

See discussions, stats, and author profiles for this publication at: <https://www.researchgate.net/publication/267633077>

Near-well effects in carbon dioxide storage in saline aquifers

Thesis · April 2013
DOI: 10.13140/2.1.1629.2809

CITATION
1

READS
114

1 author:



Ana Mijic
Imperial College London
41 PUBLICATIONS 148 CITATIONS

SEE PROFILE

Some of the authors of this publication are also working on these related projects:



CHANCE: Coupled Human And Natural Systems Environment for water management under uncertainty in the Indo-Gangetic Plain [View project](#)



Spatio-temporal assessment of annual water-balance model for Upper Ganga Basin [View project](#)

Near-well effects in carbon dioxide storage in saline aquifers

by

Ana Mijić

A thesis submitted for the degree of Doctor of Philosophy
of the Imperial College London

Department of Earth Science and Engineering
Imperial College London

June 2013

Abstract

Carbon capture and storage, that is the collection of carbon dioxide (CO_2) from power plants and its injection underground, is an important technology for reducing CO_2 emissions to the atmosphere and hence, mitigating climate change. A key aspect of CO_2 storage is the injection rate into the subsurface, which is limited by the pressure at which formation starts to fracture. Hence, it is vital to assess all of the relevant processes that may contribute to the pressure increase in the aquifer during CO_2 injection.

The central aim of this study is to analyse the ability of the near-well region of a saline formation to conduct fluids, using a set of analytical solutions that enable quick and reliable assessment of CO_2 injectivity. In this research, the near-well fluid flow was assumed to be a function of the non-Darcy flow parameter as defined by the Forchheimer equation. For the analysis of single-phase flow problems, the analytical solution for the Forchheimer flow in closed domains was derived and an alternative method for applying analytical solutions associated with a single well to multiple well systems was proposed. The CO_2 injection process was modelled as a two-phase system where the non-Darcy flow was assumed for the gas phase only, including a novel representation of the spatially varying fractional flow function. The solution for immiscible flow was further developed to model compositional displacements, which enabled analysis of the porosity reduction due to salt precipitation in a near-well region. Finally, the effects of gas compressibility were examined by integrating the analytical model with an iterative algorithm for correcting gas properties.

Results showed that in low permeability formations when CO_2 is injected at high rates non-Darcy flow conditions are more favourable for CO_2 storage than linear flow due to better displacement efficiency. This, however, came at the cost of increased well pressures. More favourable estimations of the pressure buildup were obtained when CO_2 compressibility was taken into account because reservoir pressures were reduced due to the change in the gas phase properties. The non-Darcy flow resulted in a significant reduction in solid salt saturation values, with a positive effect on CO_2 injectivity. In the examples shown, non-Darcy flow conditions may lead to significantly different pressure and saturation distributions in the near-well region, with potentially important implications for CO_2 injectivity.

Statement of own work

The contents of this report are all my own work, and any quotation from, or description of, the work of others is fully acknowledged by reference to the sources, whether published or unpublished.

The following extracts of this work have been published:

Chapter 3

- Mijic, A., Mathias, S. A., and LaForce, T. C. (2010) Nonlinear flow in multiple well systems. In *Proceedings, BHS Third International Symposium: Role of Hydrology in Managing Consequences of a Changing Global Environment, Newcastle, UK*, pp. 349–352.
- Mijic, A., Mathias, S. A., and LaForce, T. C. (2012) Multiple well systems with non-Darcy flow. *Ground Water*, doi: 10.1111/j.1745-6584.2012.00992.x.

Chapter 4

- Mijic, A., and LaForce, T. C. (2012) Spatially varying fractional flow in radial CO₂–brine displacement. *Water Resources Research*, 48(9), W09503.

Chapters 5 and 6

- Mijic, A., and LaForce, T. C. (2010) Effects of non-Darcy flow in CO₂ injection into saline aquifers. In *Proceedings, ECMOR XII: 12th European Conference on the Mathematics of Oil Recovery, Oxford, UK*.
- Mijic, A., LaForce, T. C., and Muggeridge, A. H. (2013) CO₂ injection in saline aquifers under non-Darcy conditions. *Water Resources Research*, In preparation.

Acknowledgments

Funding for this research was provided by the Grantham Institute for Climate Change, an Institute of Imperial College London. Additional support came from the John Archer Scholarship Fund and the Overseas Research Students Awards Scheme.

I am deeply grateful to my supervisors Tara LaForce and Ann Muggeridge for their guidance and patience with all the theoretical and modelling support they have offered throughout this project.

Thanks to Simon Mathias for sharing his knowledge with me. His work has always been – and still is – a huge inspiration to me. I am also grateful to Wouter Buytaert for waiting patiently for me to complete this work.

It has been a pleasure working with my colleagues, in particular, Aaron Goater, Kurt Petvipusit, Bilal Rashid and Lorena Lazaro Vallejo. I never would have made it through without my special team – thank you Susana Almeida, Sun Chun, Simon Parker and Karl Smith for being my infinite source of wisdom, comfort and fun. Karl, a special thank you for taking the time to proofread this thesis. A very special thanks to Milena, Miloš, Jelena and Janko, for always being there for me. I am grateful to my family and my husband's family, for all their support.

Finally, immense thanks to my husband Đorđe and my kids Lena, Luka and Vuk. Without their unconditional love and support none of this would have been possible.

Contents

Abstract	2
Statement of own work	3
Acknowledgments	4
List of Figures	9
List of Tables	15
Notation	17
1 Introduction	20
1.1 Context	20
1.2 Research objectives	22
1.3 Thesis outline	23
2 Literature review	25
2.1 Introduction	25
2.2 Water injection under non-Darcy conditions	26
2.2.1 Single-well systems	28
2.2.2 Multiple well systems	31
2.3 CO ₂ injection in saline aquifers	31
2.3.1 Analytical solutions for pressure buildup	33
2.3.2 Two-phase flow modelling	37
2.4 Conclusions	46
3 Non-Darcy flow in single-phase closed and/or multiple well systems	48
3.1 Introduction	48

3.2	Forchheimer flow to a well in a closed domain	48
3.2.1	Analytical solution for a single well	49
3.2.2	Multiple wells without the principle of superposition	52
3.2.3	Numerical model	53
3.3	Comparison of solutions	56
3.4	Conclusions	58
4	Immiscible non-Darcy displacement	61
4.1	Introduction	61
4.2	Spatially varying two-phase flow	62
4.2.1	Non-Darcy gas phase velocity	65
4.2.2	Non-Darcy fractional flow function	67
4.2.3	Solution for saturation by the MOC	68
4.2.4	Solving for pressure	70
4.3	Model development	74
4.3.1	Estimation of fluid properties	74
4.3.2	Relative permeability functions	80
4.3.3	Forchheimer coefficient for the mobile gas phase	81
4.4	Model results	90
4.4.1	Non-Darcy fractional flow curves	92
4.4.2	Saturation profiles	96
4.4.3	Pressure buildup	98
4.4.4	Comparison with a finite difference solution	102
4.4.5	Limitations of the proposed solution	103
4.5	Conclusions	105
5	Effects of partial miscibility	107
5.1	Introduction	107
5.2	Compositional non-Darcy two-phase displacement	108
5.2.1	Non-Darcy overall fractional flow function	110
5.2.2	Solution for composition by the MOC	112
5.2.3	Solving for pressure	114
5.2.4	Permeability reduction due to salt precipitation	115
5.3	Model development	117
5.3.1	Phase behaviour of CO ₂ -brine systems	117

5.3.2	Estimation of fluid properties for mixtures	120
5.4	Model results	121
5.4.1	Overall fractional flow function	122
5.4.2	Saturation and pressure distributions	125
5.4.3	Permeability reduction	127
5.4.4	Comparison with reservoir simulator	129
5.5	Conclusions	134
6	Effects of CO₂ compressibility	136
6.1	Introduction	136
6.2	Compressible two-phase flow	137
6.2.1	Compressibility correction	138
6.3	Model development	142
6.3.1	Density functions	142
6.4	Model results	144
6.4.1	Saturation and pressure profiles	146
6.4.2	Effects on CO ₂ injectivity	146
6.4.3	Comparison with reservoir simulator	149
6.5	Conclusions	152
7	Summary and Conclusions	154
7.1	Summary of thesis	154
7.1.1	Single-phase system pressure buildup	154
7.1.2	Two-phase system saturation distribution and salt precipitation . . .	155
7.1.3	Two-phase system pressure buildup	158
7.2	Summary of contributions to knowledge	160
7.3	Recommendations for further work	161
7.3.1	Estimation of Forchheimer coefficient	161
7.3.2	Correction of pressure estimation due to salt precipitation	161
7.3.3	Modelling the effects of rock dissolution	162
7.3.4	Multiple well analysis in two-phase displacement	162
7.3.5	Reservoir simulator with saturation-dependent Forchheimer flow . .	163
7.3.6	Extending the validity of analytical models	163
7.4	Implications and conclusions	163

References	165
A Derivation of two-dimensional finite difference approximation for single-phase liquid non-Darcy flow	178
B Derivation of the radial differential equation for single-phase flow	180
C Equal area rule in radial non-Darcy displacement	182
D Derivation of the radial differential equation for compressible two-phase displacement	186

List of Figures

1.1	Geological storage options (Metz, 2005).	21
2.1	Radial flow under steady state conditions in a groundwater storage system (modified from Dake (1983)).	29
2.2	Radial flow under semi-steady state conditions in a groundwater storage formation (modified from Dake (1983)).	30
2.3	Typical CO ₂ profile under segregated flow conditions (Nordbotten et al., 2005).	34
2.4	Flow regions during CO ₂ injection under diffuse flow conditions and resulting pressure distribution (Burton et al., 2008).	36
2.5	Fractional flow function for immiscible water-oil displacement (Buckley and Leverett, 1942) and the Welge (1952) method for the shock saturation. . . .	39
2.6	Riemann solution for Buckley and Leverett (1942) equation (LeVeque, 1992): a) triple-valued saturation profile, b) unique solution with a shock front and c) characteristics for the discontinuity present initially at the inlet and for the initial saturation.	40
2.7	Motion of a shock during diffuse flow displacement (Orr, 2007).	40
2.8	Fractional flow function for miscible gas-oil displacement (Orr, 2007).	42
2.9	Riemann solution for miscible gas-liquid displacement.	42
2.10	Pressure-mole fraction CO ₂ -water phase diagram at 25 °C. Phases labeled are: V - vapour phase, L ₁ - water-rich liquid and L ₂ - CO ₂ -rich liquid (Spycher et al., 2003).	44
3.1	Schematic diagram of a multiple well system.	52
3.2	Schematic diagram of the finite difference model.	55
3.3	Implicit numerical scheme in a matrix form (modified from Mijic (2009)). .	56
3.4	Forchheimer coefficient, b obtained from Geertsma (1974) correlation.	57

3.5	Dimensionless well pressure in a circular domain for various values of r_e/r_w and different levels of flow nonlinearity. The analytical solution is that given in equation (3.17), shown only within the time range of validity.	58
3.6	Dimensionless well pressure in a square domain for various values of L/r_w and different levels of flow nonlinearity. The analytical solution is that given in equation (3.17) with r_e obtained from equation (3.18), shown only within the time range of validity.	59
4.1	Control volume in a radial two-phase flow system.	62
4.2	Iterative procedure for the calculation of the non-Darcy gas flux.	67
4.3	Equal area rule for immiscible non-Darcy displacement.	71
4.4	Solution algorithm for the two-phase Darcy and non-Darcy immiscible displacements. Modules that implement novel approaches to the solution of the non-Darcy problem are highlighted in grey.	75
4.5	$P - V - T$ relationship calculated using the Redlich and Kwong (1949) equation of state (4.52) (solid line) and Hermite polynomial interpolation algorithm (circular markers).	76
4.6	CO ₂ properties: a) density and b) viscosity as a function of pressure and temperature. Both properties vary significantly within the chosen range of pressures.	77
4.7	Variation of brine properties: a), c) and e) with pressure for $K_s=0.15 \text{ g cm}^{-3}$ and b), d) and f) with salinity for $P=30 \text{ MPa}$. Brine density increases with salinity, while viscosity and compressibility of brine are both dependent on pressure and salt concentration.	79
4.8	Relative permeability experimental data for Berea sandstone (Krevor et al., 2012) and correlation model estimations.	82
4.9	Relative permeability experimental data for the four sandstone samples (Krevor et al., 2012) and modified Corey and van Genuchten models (equations (4.66) and (4.67), respectively) with best fit parameters given in Table 4.1.	83

4.10	Mobile liquid phase non-Darcy coefficient experimental data and empirical correlations (4.70)–(4.73) optimised to the two data sets simultaneously. Correlation is greatly influenced by the lack of experimental data in the middle of the effective permeability range. Forchheimer coefficient for the gas phase is greatly overestimated for Ottawa sands.	87
4.11	Mobile liquid phase non-Darcy coefficient experimental data and separately optimised theoretical correlations for a) Carbonate and b) Ottawa sand. . .	87
4.12	Mobile liquid phase non-Darcy coefficient experimental data for Ottawa sand fitted using the saturation dependent correlation (4.75).	89
4.13	CO ₂ -brine system relative permeability functions. Input data are shown in Table 4.5.	90
4.14	Inertial effects as a function of the gas phase saturation for $Q_m=100 \text{ kg s}^{-1}$ and $W=3.2 \cdot 10^{-7} \text{ m}^{1.5}$	92
4.15	Non-Darcy fractional flow curves as a function of the gas phase saturation and radial distance from the well for $Q_m=100 \text{ kg s}^{-1}$ and $W=3.2 \cdot 10^{-7} \text{ m}^{1.5}$. . .	93
4.16	Schematic representation of the influence of the non-Darcy effect in a radial CO ₂ -brine displacement. For $r > r_d$, the non-Darcy effect is insignificant. . .	94
4.17	Comparison of non-Darcy fractional flow curves with respect to the formation thickness and permeability. Figure 4.17a corresponds to Figure 4.15. . .	95
4.18	Saturation profiles of Darcy and non-Darcy displacements 12 hours after the beginning of the injection at the rate $Q_m=100 \text{ kg s}^{-1}$. The formation thickness is $H=50 \text{ m}$ and permeability is $k=10^{-13} \text{ m}^2$	97
4.19	Saturation profiles of non-Darcy displacements for various mass injection rates, after a fixed mass of CO ₂ has been injected for $W=3.2 \cdot 10^{-7} \text{ m}^{1.5}$, $H=50 \text{ m}$ and $k=10^{-13} \text{ m}^2$	97
4.20	Comparison of CO ₂ saturation distributions for cases a) and b) shown in Figure 4.17. Time is set to 0.5, 5 and 50 days after the beginning of the injection. The injection rate is $Q_m=100 \text{ kg s}^{-1}$ and the Forchheimer flow constant for non-Darcy flow is $W=3.2 \cdot 10^{-7} \text{ m}^{1.5}$	98
4.21	Pressure distribution along the reservoir for Darcy and non-Darcy flow 12 hours after the beginning of the injection. Open flow boundary is set at $r=5000 \text{ m}$. Remaining parameters are $Q_m=100 \text{ kg s}^{-1}$, $H=50 \text{ m}$ and $k=10^{-13} \text{ m}^2$	100

4.22	Comparison of pressure distributions for cases a) and b) shown in Figure 4.17. Time is set to 0.5, 5 and 50 days after the beginning of the injection, before the boundary impacts the pressure. The injection rate is $Q_m=100 \text{ kg s}^{-1}$ and the Forchheimer flow constant for non-Darcy flow is $W=3.2 \cdot 10^{-7} \text{ m}^{1.5}$. Open flow boundary is set at $r=5000 \text{ m}$	101
4.23	Comparison of pressure distributions for: a) open and b) closed formations. Time is set to 200, 500 and 1000 days after the beginning of the injection. The pressure effect has reached the boundary at $t=115$ and 62 days in open and closed formations, respectively. The parameters are $Q_m=100 \text{ kg s}^{-1}$, $W=3.2 \cdot 10^{-7} \text{ m}^{1.5}$, $H=50 \text{ m}$ and $k=10^{-13} \text{ m}^2$. The far-field boundary condition is set at $r=5000 \text{ m}$	102
4.24	Comparison between analytical and numerical solutions for Darcy (lower saturations) and non-Darcy (higher saturations) flow 5 days after the beginning of the injection. The injection rate is $Q_m=100 \text{ kg s}^{-1}$ and the Forchheimer flow constant is $W=3.2 \cdot 10^{-7} \text{ m}^{1.5}$	103
5.1	Approximation of the compositional model of CO_2 injection into a saline formation (Zeidouni et al., 2009).	107
5.2	Overall fractional flow function within the single-phase gas region for spatially varying Forchheimer flow. Inertial effects increase with the proximity to the well ($r_w < r_1 < r_2$).	111
5.3	Equal area rule for miscible non-Darcy displacement.	114
5.4	Solution algorithm for the two-phase Darcy and non-Darcy miscible displacements. Modules that implement novel approaches to the non-Darcy problem solution are additionally highlighted in grey. Model components added to the immiscible solution algorithm to account for the phase behaviour are highlighted with a thick black border.	118
5.5	Non-Darcy overall fractional flow curves as a function of gas phase composition and radial distance from the well for $Q_m=100 \text{ kg s}^{-1}$, $W=3.2 \cdot 10^{-7} \text{ m}^{1.5}$ and $K_s=0.15 \text{ g cm}^{-3}$	123
5.6	Spatially varying non-Darcy overall fractional flow in near-well CO_2 region as a function of gas phase composition for $Q_m=100 \text{ kg s}^{-1}$, $W=3.2 \cdot 10^{-7} \text{ m}^{1.5}$ and $K_s=0.15 \text{ g cm}^{-3}$	124

5.7	Non-Darcy overall fractional flow curves as a function of gas phase composition and radial distance from the well in the model with constant Forchheimer coefficient, b_1 . Parameters are set to $Q_m=100 \text{ kg s}^{-1}$, $W=3.2 \cdot 10^{-7} \text{ m}^{1.5}$ and $K_s=0.15 \text{ g cm}^{-3}$	125
5.8	Effects of the Forchheimer coefficient variability on: a) CO_2 saturation and b) pressure distributions five days after the beginning of injection for $Q_m=100 \text{ kg s}^{-1}$, $W=3.2 \cdot 10^{-7} \text{ m}^{1.5}$ and $K_s=0.15 \text{ g cm}^{-3}$	126
5.9	Effects of brine salinity in Darcy displacement on: a) CO_2 saturation and b) pressure distributions five days after the beginning of injection for $Q_m=100 \text{ kg s}^{-1}$. Reference salinity case is for $K_s=0.15 \text{ g cm}^{-3}$ and higher salinity for $K_s=0.30 \text{ g cm}^{-3}$	127
5.10	Effects of the Forchheimer coefficient variability on permeability reduction parameters for: a)–c) reference case with $K_s=0.15 \text{ g cm}^{-3}$ and d)–f) higher salinity case with $K_s=0.30 \text{ g cm}^{-3}$. The injection rate is $Q_m=100 \text{ kg s}^{-1}$ and the Forchheimer flow constant is $W=3.2 \cdot 10^{-7} \text{ m}^{1.5}$	128
5.11	The simulation model capillary pressure function obtained using the van Genuchten (1980) model. Input parameters are given in Table 5.4.	131
5.12	Comparison of: a) CO_2 saturation and b) pressure distributions for the reference case (i.e. $K_s=0.15 \text{ g cm}^{-3}$) during the early injection period ($t=0.5$, 5 and 50 days). The injection rate is $Q_m=100 \text{ kg s}^{-1}$ and the Forchheimer flow constant for non-Darcy flow is $W=3.2 \cdot 10^{-7} \text{ m}^{1.5}$. The Forchheimer coefficient, b_1 is assumed to be independent of the gas phase saturation for the purpose of benchmarking.	132
5.13	Comparison of: a) development of the dry-out front and b) salt saturation for the reference case (i.e. $K_s=0.15 \text{ g cm}^{-3}$) during early injection period ($t \leq 50$ days). The injection rate is $Q_m=100 \text{ kg s}^{-1}$ and the Forchheimer flow constant for non-Darcy flow is $W=3.2 \cdot 10^{-7} \text{ m}^{1.5}$. The Forchheimer coefficient, b_1 is assumed to be independent of the gas phase saturation for the purpose of benchmarking.	133
6.1	Algorithm to account for CO_2 compressibility in Darcy and non-Darcy solutions. Additional modules, compared with those developed in chapters 4 and 5, are shown with a thick black line.	143

6.2	CO ₂ density functions at $T = 40^\circ\text{C}$. Exponential and linear correlations are calculated from equations (6.28) and (6.29), respectively, with $c_P = 1.04 \cdot 10^{-8} \text{ Pa}^{-1}$ and $\rho_{10} = 691.8 \text{ kgm}^{-3}$ at $P_0=12 \text{ MPa}$	145
6.3	CO ₂ compressibility as a function of reservoir temperature and pressure calculated from: a) Redlich and Kwong (1949) approximation (equation (6.27)), b) linear density approximation (equation (6.30)) and c) exponential density approximation ($c_1 = c_P$).	145
6.4	Effects of non-Darcy flow in incompressible and compressible displacements on a)-b) CO ₂ saturation and c)-d) pressure distributions 5 days after the beginning of injection for $Q_m=100 \text{ kg s}^{-1}$. Forchheimer coefficient for non-Darcy flow is $W=3.2 \cdot 10^{-7} \text{ m}^{1.5}$	147
6.5	Relative error in a) leading front location and b) well pressure estimations associated with neglecting the non-Darcy effects in compressible displacement. Formation thickness is $H = 200 \text{ m}$ and Forchheimer coefficient for non-Darcy flow is $W=3.2 \cdot 10^{-7} \text{ m}^{1.5}$	149
6.6	CO ₂ injectivity under Darcy and non-Darcy flow conditions and variable formation permeabilities. Formation thickness is $H = 200 \text{ m}$ and Forchheimer coefficient for non-Darcy flow is $W=3.2 \cdot 10^{-7} \text{ m}^{1.5}$	150
6.7	Comparison of a) CO ₂ saturation and b) pressure distributions during early injection period ($t \leq 50 \text{ days}$). The injection rate is $Q_m=100 \text{ kg s}^{-1}$ and the Forchheimer flow constant for non-Darcy flow is $W=3.2 \cdot 10^{-7} \text{ m}^{1.5}$. The Forchheimer coefficient, b_1 is assumed to be independent of the gas phase saturation for the purpose of benchmarking.	151
C.1	Equal area rule for leading front calculation	183
C.2	Equal area rule for trailing front calculation	184

List of Tables

3.1	Dimensionless transition times and error estimates for MWS models comparison.	59
4.1	Summary of experimental data (k_{r10} , k_{r20} , S_{1c} and S_{2r}) from Krevor et al. (2012) and optimised values of the modified Corey and van Genuchten model parameters n and g (equations (4.66) and (4.67), respectively).	82
4.2	Mobile liquid saturation literature data for carbonates (Wong, 1970) and Ottawa sands (Evans and Evans, 1988).	84
4.3	Values of the Forchheimer flow constant, W in the original correlations (4.70)–(4.73) and the corresponding units for b and kk_r	86
4.4	Values of Forchheimer flow constant, W obtained by optimising the empirical correlations to the experimental data sets independently.	88
4.5	Parameters used for the analytical model simulations and values of fluid properties at the initial reservoir pressure.	91
4.6	Performance of the Picard scheme: Number of iterations as a function of the Forchheimer flow constant and radial distance from the well for $Q_m=100 \text{ kg s}^{-1}$, $H=50 \text{ m}$ and $k=10^{-13} \text{ m}^2$	96
4.7	Simulation results for Darcy and non-Darcy flow for two cases shown in Figure 4.20: a) $H=50 \text{ m}$ and $k=10^{-13} \text{ m}^2$ and b) $H=200 \text{ m}$ and $k=10^{-13} \text{ m}^2$. The injection rate is $Q=100 \text{ kg s}^{-1}$ and the initial pressure is $P_0=12 \text{ MPa}$. Subscript L denotes the value of the parameter at the leading shock front.	99
5.1	Mutual solubilities of CO_2 and water as a function of pressure at $T=40^\circ\text{C}$ and brine salinity of 15 g cm^{-3}	121
5.2	Fluid properties and phase behaviour of CO_2 -brine system with initial conditions defined in Table 4.5.	122

5.3	Simulation results for miscible Darcy ($W=0$) and non-Darcy ($W=3.2 \cdot 10^{-7} \text{ m}^{1.5}$) flow and reference and higher salinity cases five days since the beginning of injection. Subscripts L and T denote values of the parameter at the leading and trailing shock fronts, respectively. Results for immiscible displacement from Table 4.7, case b are repeated for comparison.	126
5.4	Model parameters used in the reservoir simulator. Corresponding initial and boundary conditions are given in Table 4.5.	131
6.1	Simulation results for compressible Darcy ($W=0$) and non-Darcy ($W=3.2 \cdot 10^{-7} \text{ m}^{1.5}$) flow with constant and variable Forchheimer coefficient b_1	148

Notation

q	fluid flux [L T^{-1}]	26
k	intrinsic formation permeability [L^2]	26
μ	dynamic viscosity [$\text{M L}^{-1} \text{T}^{-1}$]	26
P	pressure [$\text{M L}^{-1} \text{T}^{-2}$]	26
r	radial distance [L]	26
ρ	fluid mass density [M L^{-3}]	27
b	Forchheimer coefficient [L^{-1}]	27
ϕ	formation porosity (–)	28
Q	injection rate [$\text{L}^3 \text{T}^{-1}$ or M T^{-1}]	28
H	formation thickness [L]	28
c	compressibility [$\text{M}^{-1} \text{L T}^2$]	28
t	time [T]	28
E	exponential integral (–)	28
S	phase saturation (–)	38
A	reservoir cross-sectional area [L^2]	38
x	linear distance/coordinate of grid nodes in x direction [L]	38
f	phase fractional flow (–)	38
D	pressure domain specific storage [$\text{M}^{-1} \text{L T}^2$]	49
L	length of a square domain/MWS well spacing [L]	53
y	coordinate of grid nodes in y direction [L]	53
δ	dummy variable defining sink term (–)	53
N	number of points (–)	54
B	Forchheimer flow parameter [$\text{L}^{-1} \text{T}$]	65
β	Forchheimer factor (–)	65
η	differential parameter (–)	68
v	dimensionless wave velocity (–)	69
G	pressure integral (–)	71
α	exponential integral constant (–)	72
a	intermolecular attraction ($\text{bar cm}^6 \text{mol}^{-2} \text{K}^{0.5}$)	74
d	intermolecular repulsion ($\text{cm}^3 \text{mol}^{-1}$)	74
V	molar volume ($\text{cm}^3 \text{mol}^{-1}$)	74

T	temperature ($^{\circ}\text{C}$ or K)	74
R	universal gas constant ($\text{bar cm}^3 \text{mol}^{-1} \text{K}^{-1}$)	74
M	molar mass (g mol^{-1})	76
K	concentration [ML^{-3}]	78
n	Corey model parameter ($-$)	80
l	pore connectivity ($-$)	80
g	van Genuchten model parameter ($-$)	80
W	Forchheimer flow constant [$\text{L}^{-3/2}$]	86
w	mass fraction ($-$)	109
C	overall phase composition ($-$)	109
F	overall phase fractional flow ($-$)	109
s	volume fraction ($-$)	109
γ	activity coefficient ($-$)	117
m	molality ($-$)	117
Φ	fugacity coefficient ($-$)	117
Θ	equilibrium constant ($-$)	119
λ	mole fraction ($-$)	119
ν	stoichiometric number of ions contained in the dissolved salt ($-$)	119
Γ	two-phase solubility factor ($-$)	119
p	van Genuchten capillary model parameter ($-$)	130
ξ	self-similar transformation function [$\text{L T}^{-0.5}$]	137
U	scaled fluid flux [$\text{L T}^{-0.5}$]	137
Z	compressible flow parameter ($-$)	140
I	injectivity [L T]	148

Subscripts

0	initial (time, density) / end-point (permeability)	28
e	extent of the reservoir unit	29
h	water	38
r	rock (compressibility) / relative (permeability) / residual (saturation)	49
w	well	49
c	critical (time, saturation) / CO_2	51
1	gas phase	62

2	liquid phase	62
D	dimensionless	68
L	leading shock	70
p	two-phase	71
b	brine	72
s	salt	78
exp	experimental	88
mod	model	88
T	trailing shock	113
atm	atmospheric	120
C	capillary	130
P	reference pressure	139
max	maximum	144

Superscripts

n	time step	54
0	Darcy fraction of gas flux	65
i	iteration level	66

Chapter 1

Introduction

1.1 Context

Carbon dioxide capture and storage (CCS) is an important potential technology for reducing atmospheric emissions of carbon dioxide (CO_2) from human activities, and hence mitigating climate change (Metz, 2005). It can be applied to large point sources of CO_2 such as power plants or large industrial processes. The CCS process involves three steps: firstly, the collection or capture of CO_2 at the source; secondly, the captured CO_2 transportation to a chosen storage site, which can be located at any distance from the CO_2 source site; finally, CO_2 injection into an underground geological storage formation.

The focus of this research is underground geological CO_2 storage. As shown in Figure 1.1, geological storage options include depleted oil and gas fields, unminable coal beds and deep saline formations. These suitable storage formations can be located in both onshore and offshore aquifers. Whereas the use of oil and gas fields is favourable due to the availability of site characterisation data, it is estimated that saline aquifers can potentially store approximately 1,000 gigatonnes (Gt) of CO_2 , which is by far the largest storage capacity compared to the other options (Metz, 2005). Depleted oil and gas reservoirs and unminable coal beds are estimated to have a storage capacity of about 700 Gt and less than 200 Gt, respectively.

The injection of CO_2 in a saline formation is a complex problem. There are four main reasons for this:

1. Injection of CO_2 raises pressure near the well, and the degree of pressure buildup will depend on the injection rate, permeability and porosity of the formation and the presence or absence of permeability barriers within or around it (Metz, 2005). How-

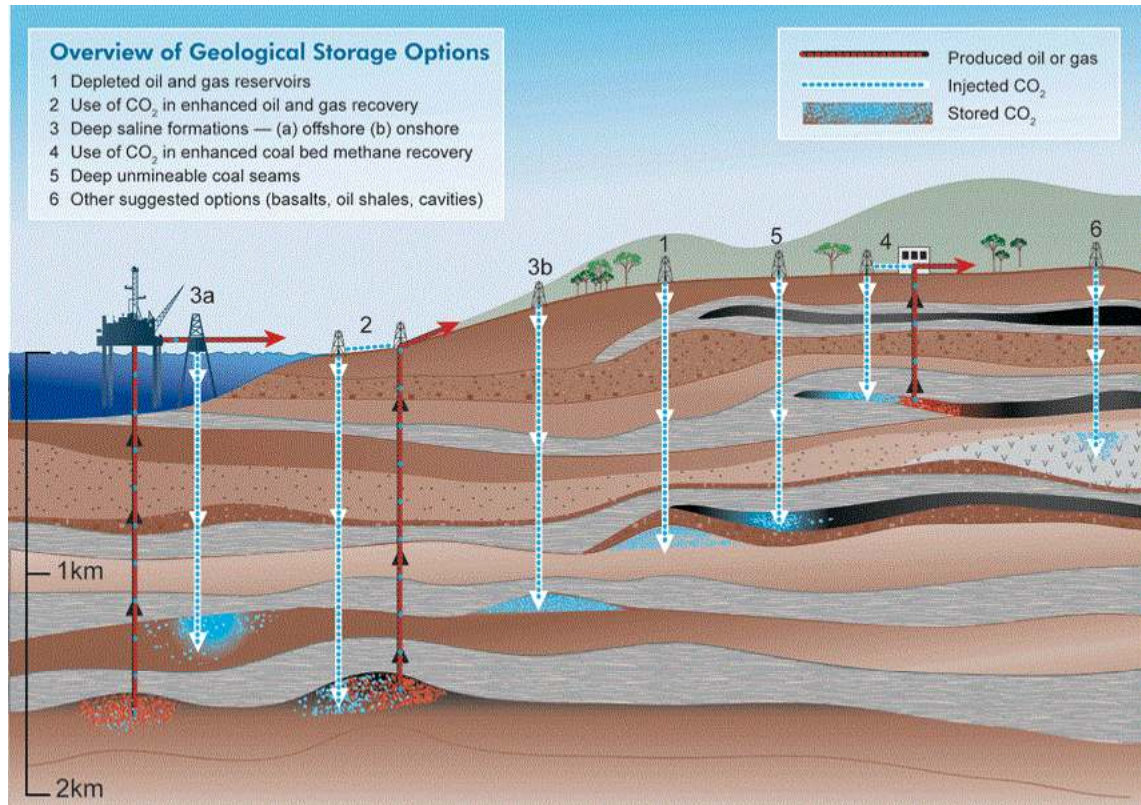


Figure 1.1: Geological storage options (Metz, 2005).

ever, to introduce CO₂ into the storage formation, the downhole injection pressure has to be higher than the reservoir fluid pressure, but lower than the pressure that may induce fractures in the formation (Mathias et al., 2009b). Therefore, prior to the start of the injection process, it is necessary to determine the rate at which CO₂ can be injected without exceeding the fracture pressure of the top seal. The problem becomes even more complicated if it is necessary to increase the number of injection wells in order to achieve the required injection rate. Since each injection well costs millions of dollars and has an environmental impact on the surface (Metz, 2005), the problem of optimising multiple well systems has to be addressed.

2. In saline aquifers, the effective permeability and porosity of the near-well region are likely to decrease with time. This is because the injected CO₂ can induce the resident saline water's evaporation, resulting in salt deposition. This deposition may have a negative impact on the gas injectivity (Prévost et al., 2004).
3. CO₂ is a compressible gas, whose properties vary significantly with the change of the reservoir pressure (Spycher et al., 2003). The increase of the gas density and viscosity, however, should be beneficial for CO₂ storage because of the decreased gas

mobility and pressure reduction within the formation.

4. Solutions to subsurface problems usually assume a first-order (linear) relationship between the fluid flux and the pressure gradient, as described by Darcy's law (Darcy, 1856). At high injection rates, however, inertial effects may become significant and the assumption of flow linearity becomes invalid. This may influence pressure and saturation distributions in two-phase displacement (Wu, 2001).

The competition between salt precipitation, compressibility and non-Darcy effects, together with the influence of the formation boundary on the pressure buildup, should therefore determine whether it gets easier or harder to inject CO₂ with time. To accurately estimate the suitability of the aquifer for CO₂ injection, it is necessary to quantify the level of influence of these effects on saturation and pressure distributions within the storage formation.

1.2 Research objectives

The objectives of this thesis are:

1. To examine the possibility of multiple well analysis in single-phase non-Darcy systems and the potential for implementation in two-phase problems.
2. Considering potentially significant inertial effects (Wu, 2001), to extend the existing analytical model of the two-phase flow (Buckley and Leverett, 1942) to represent the non-Darcy behaviour of the gas phase in immiscible radial displacement.
3. To analyse combined effects of non-Darcy flow, miscibility and compressibility by extending the solution to include interphase mass transfer and change in gas phase properties as a function of pressure.

To achieve these objectives, solutions to the system of equations describing fluid behaviour and pressure distribution will extend the relevant physics for radial flow of single and multiple phases to include the inertial effects in the near-well area using the Forchheimer equation (Forchheimer, 1901). Developed models should also provide useful validation of more complex numerical solutions.

It should be noted that if CO₂ is injected into carbonate aquifers, it will dissolve the aquifer rock in the near-well region and increase the formation permeability and porosity (Noh et al., 2007). This is beneficial for CO₂ injectivity, but could cause well failure if a

substantial fraction of the limestone and cement are dissolved at the well. Moreover, in fractured systems it has been observed experimentally that the dissolution/precipitation reaction of limestone and CO_2 tends to enhance the preferential flow paths (Singurindy and Berkowitz, 2005), which could cause channeling of CO_2 and lead to poor storage efficiency in the long run. However, the present research, whilst attempting to understand and quantify effects of salt precipitation in the near-well region, does not attempt to account for rock dissolution effects.

1.3 Thesis outline

This thesis consists of seven chapters. This chapter introduces the problem and outlines the research objectives.

In Chapter 2, a literature review gives a brief background of the key concepts associated with pressure buildup modelling in both single and two-phase systems and fractional flow theory in immiscible and compositional displacements. It then presents research which has been carried out to look at these physical processes under non-Darcy flow conditions. Chapter 2 concludes by proposing a number of research questions to be addressed by this thesis.

One of the ways to address the research questions is to begin the analysis of non-Darcy effects by modelling single-phase liquid flow. Therefore, in Chapter 3 the development and results of the analytical solutions for the pressure buildup in closed single-well are given, enabling analysis of multiple well systems under non-Darcy flow conditions.

In Chapter 4, Forchheimer flow in immiscible two-phase flow is investigated by assuming non-Darcy flow of the gas phase. The spatially varying fractional flow function is obtained by implementing an iterative procedure for the determination of the gas phase velocity. The solution for saturation, obtained using a modified method of characteristics, and pressure calculations are applied for the analysis of CO_2 injection in saline aquifers. Finally, the model is verified by comparison to the corresponding numerical solution, and its limitations are discussed.

In Chapter 5, the analytical solution presented in Chapter 4 is extended to model compositional behaviour of a gas-liquid system. The aim is to obtain a model that is a better representation of the full physics of the CO_2 injection problem. A solution for miscible non-Darcy flow is obtained and its performance tested by comparison with the ECLIPSE 300 reservoir simulator. The results of the analytical solution are used to analyse

the influence of the Forchheimer flow on salt precipitation distribution in the near-well region.

Chapter 6 is dedicated to the application of the compressibility correction in the miscible non-Darcy model. An iteration algorithm is implemented to obtain the best reservoir pressure for the calculation of CO₂ properties. The reservoir simulator is again used for comparison of results, and non-Darcy effects on CO₂ injectivity are discussed.

Finally, in Chapter 7, the findings of this study, the contributions to the knowledge that have been made, suggestions for future work and conclusions are presented.

Chapter 2

Literature review

2.1 Introduction

An important task in groundwater hydraulics and reservoir simulation is the prediction of fluid pressure distribution resulting from pumping and/or injecting fluids. Pressure estimation can be obtained either from numerical models or analytical solutions. Easy to implement and computationally efficient, analytical solutions are often considered a practical approach to flow analysis. In addition, they are useful for validation of complex numerical codes. However, they are only correct under simplifying assumptions needed for their derivation.

Distribution of the reservoir pressure over space and time is determined by the flow regime, aquifer properties, fluid properties and the type of the aquifer boundary. Fluid flow in the subsurface is usually modelled by Darcy's equation. However, in single-phase liquid systems, non-Darcy flow has been observed in both granular media and fractured reservoirs. If gas or supercritical CO₂ is injected in a liquid or brine-saturated aquifer, the system of equations describing these flows becomes increasingly nonlinear. In addition, low-viscosity gases can have a flow velocity that is more than an order of magnitude greater than a liquid phase flux for the same pressure change. In such circumstances, equations describing the flow of a gas phase through a porous formation often should include a non-Darcy component.

The key factor that influences porosity change during CO₂ injection in saline aquifers is salt precipitation due to residual brine vaporisation into the flowing gas phase. This process can significantly reduce the formation effective permeability and porosity in the near-well region. Injected CO₂, being a highly compressible gas, has properties that significantly

vary with a change of pressure. Both these effects can significantly alter the pressure distribution in an aquifer used for CO₂ storage. The first will tend to increase pressure, possibly reducing injectivity, but it may be mitigated by compressibility effects. Thus it is necessary to predict their relative impact on pressure distribution within the storage formation.

For both single and two-phase problems, most relevant solutions have been designed for single-well systems situated in infinite aquifers. However, if the overall aquifer pressure needs to be maintained below some limiting value, it may be necessary to consider multiple well systems. Moreover, some reservoir formations contain low-permeability regions. For analysis of both scenarios it may be necessary to change the outer boundary condition, which alters the response of the system once the pressure perturbation has reached the reservoir boundary.

In this chapter, a summary of current approaches to analytical pressure buildup modelling in single and two-phase systems is provided, with particular attention to previous work carried out to understand the processes that are significant in the near-well region. The review identifies important gaps in understanding of the most relevant processes that control water and CO₂ injectivity in liquid formations, which form the key research questions for this study.

2.2 Water injection under non-Darcy conditions

Groundwater systems can be artificially recharged by re-injection of water back into the aquifer for later recovery and use. Water may be injected into either confined or unconfined formations. This process is known as the Aquifer Storage and Recovery (Martin and Dillion, 2002). The usual modelling approach is to assume linear flow, that is the first-order relationship between the fluid flux and the pressure gradient known as Darcy's law (Darcy, 1856):

$$q = -\frac{k}{\mu} \frac{dP}{dr} \quad (2.1)$$

where q is fluid flux, k is intrinsic formation permeability, μ is dynamic viscosity, P is fluid pressure and r is radial distance from the well. These flow problems are well described by linear sets of equations (Theis, 1935; Mathias and Butler, 2006). However, with increasing flow velocity, inertial forces become significant and the linear relationship between pressure

rise and the flow rate becomes invalid. This flow condition is often described using the Forchheimer equation (Forchheimer, 1901):

$$\frac{\mu q}{k} + \rho b q |q| = -\frac{dP}{dr} \quad (2.2)$$

where ρ is fluid mass density and b is known as the Forchheimer coefficient. Compared to Darcy equation, the additional term on the left-hand-side of equation (2.2) represents the kinetic energy of the fluid flow at high velocities. This study addresses the problem of water injection under non-Darcy flow. However, the same approach is appropriate for either injection or production well systems.

Theoretical aspects of the Forchheimer equation were presented in studies of Irmay (1958), Ruth and Ma (1992), Whitaker (1996), Giorgi (1997) and Chen et al. (2001). Hasanizadeh and Gray (1987) derived the generalised form of the Forchheimer equation based on the fundamental laws of continuum mechanics, concluding that the non-Darcy flow occurs due to significant viscous effects at high flow velocities. Non-Darcy flow has been observed in both coarse granular media (Thiruvengadam and Kumar, 1997; Venkataraman and Rama Mohan Rao, 1998, 2000; Legrand, 2002; Chen et al., 2003; Reddy and Rao, 2006; Sidiropoulou et al., 2007) and fractured formations (Kohl et al., 1997; Lee and Lee, 1999; Qian et al., 2005, 2007). Chen et al. (2003) analysed non-Darcy flow in horizontal wells and verified numerical results with data monitored on a physical laboratory model. More recently, Mathias and Todman (2010) demonstrated a formal link between the Forchheimer coefficient and the so-called well-loss coefficient, associated with the analysis of a step drawdown test.

The non-Darcy regime can be identified either with the critical value of Reynolds number or Forchheimer number (Zimmerman et al., 2004; Zeng and Grigg, 2006). Due to the clear meaning of variables, the Forchheimer number defined as (Zeng and Grigg, 2006):

$$F_0 = \frac{kb\rho q}{\mu} \quad (2.3)$$

was recommend to define the onset of non-Darcy flow. The critical value of $F_0 = 0.11$ corresponds to 10% non-Darcy effect. Value of the Forchheimer coefficient, b can be found from many empirical correlations, summarised in the comprehensive review of Li and Engler (2001). The authors suggested a procedure for choosing the right correlation based on the formation lithology and the estimation of aquifer properties. Based on comparison between

non-Darcy coefficients obtained from laboratory and field-scale measurements, Mathias and Todman (2010) proposed the Geertsma (1974) correlation:

$$b = 0.005\phi^{-5.5}k^{-0.5} \quad (2.4)$$

where ϕ is a formation porosity, as the most adequate for the modelling of single-phase liquid systems. Inertial effects are most significant in the near-well area, where high-velocity non-Darcy conditions occur (Mathias et al., 2008; Mathias and Todman, 2010).

2.2.1 Single-well systems

For a short time after some pressure disturbance has been created in the reservoir, or in the case of an infinite aquifer, the effects of the boundary are not felt and the system is mathematically infinite (Dake, 1983). Both pressure and its derivative with respect to time are functions of a radial distance and time.

Under Darcy flow conditions, the transient solution for pressure is given by Theis (1935):

$$P - P_0 = \frac{Q\mu}{4\pi Hk} E\left(\frac{\mu cr^2}{4kt}\right) \quad (2.5)$$

where P_0 is the initial fluid pressure, Q is the volumetric injection rate, H is the formation thickness, c is compressibility, t is time since the beginning of injection and E denotes the exponential integral function. Equation (2.5) corresponds to the link-source solution, which assumes that the well radius is negligible compared to the size of the aquifer, and therefore can be treated as a line (Dake, 1983).

Although an exact solution describing transient Forchheimer flow does not currently exist, some authors have developed approximate solutions (Şen, 1988; Kelkar, 2000; Wu, 2002a). A comprehensive set of analytical and semi-analytical solutions for the problem of transient Forchheimer flow to a single-well within an aquifer of infinite extent was presented in Mathias et al. (2008). After the pressure disturbance has reached the boundary, the pressure distribution in the reservoir will depend on the boundary type.

Open aquifers

In aquifers that have a completely open outer boundary, the fluid injection at the well is assumed to be balanced by fluid exit across the boundary (Dake, 1983). Pressure at the

boundary therefore remains constant for all times and the reservoir is said to be under steady state flow conditions (Figure 2.1).

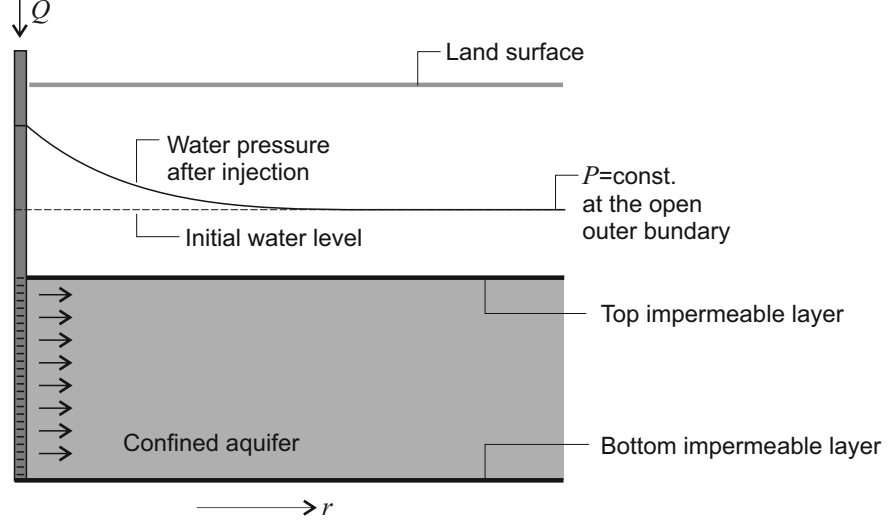


Figure 2.1: Radial flow under steady state conditions in a groundwater storage system (modified from Dake (1983)).

For flow governed by Darcy's law, a steady state solution for pressure was given by Thiem (1906):

$$P - P_0 = \frac{Q\mu}{2\pi Hk} \ln\left(\frac{r_e}{r}\right) \quad (2.6)$$

where r_e is the radial extent of the formation unit. Non-Darcy flow in single-well open systems has been extensively studied in the past. The analytical solution to steady state radial Forchheimer flow was obtained by Bear (1979):

$$P - P_0 = \frac{Q\mu}{2\pi Hk} \ln\left(\frac{r_e}{r}\right) + b\rho \frac{Q|Q|}{4\pi^2 H^2} \left(\frac{1}{r} - \frac{1}{r_e}\right) \quad (2.7)$$

Numerous other studies addressed the numerical simulation of non-Darcy flow using the Forchheimer equation. Some of them implemented the finite element approximation (Ewing et al., 1999; Kolditz, 2001), while others applied the finite difference approach (Holditch and Morse, 1976; Choi et al., 1997; Wu, 2002b; Belhaj et al., 2003).

Note that most solutions for non-Darcy flow specifically relate to confined aquifers. To account for non-Darcy flow behaviour during a constant-head well test in an unconfined

aquifer, Chen and Chang (2003) developed a curve matching method with the skin effect, which accounts for the change in the pressure drop compared to the one predicted with Darcy law. Moutsopoulos (2007) implemented the Forchheimer equation to solve one-dimensional unsteady flow in an unconfined semi-infinite aquifer. More recently, Eck et al. (2012) developed an analytical solution for the Forchheimer seepage through an inclined porous layer under constant areal recharge.

Closed aquifers

When an aquifer is limited by a low-permeability region that prevents the flow across the boundary, the pressure derivative with respect to time is constant (Dake, 1983). Additional pressure buildup in the reservoir, under so-called semi-steady state flow conditions, is shown in Figure 2.2.

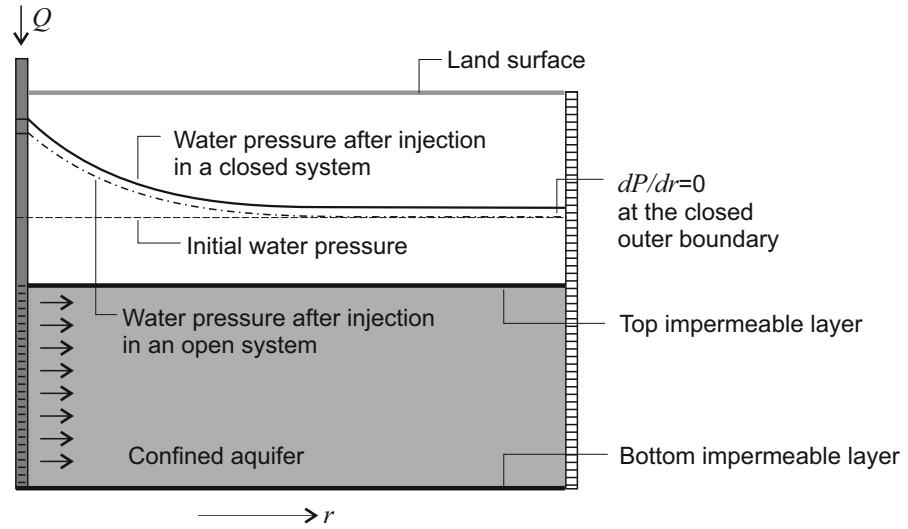


Figure 2.2: Radial flow under semi-steady state conditions in a groundwater storage formation (modified from Dake (1983)).

The solution for Darcy flow in closed systems is very similar to solution given by Thiem (1906), having an additional term to account for the influence of the no-flow boundary (Dake, 1983):

$$P - P_0 = \frac{Q\mu}{2\pi Hk} \ln \left(\frac{r_e}{r} - \frac{1}{2} \right) \quad (2.8)$$

Non-Darcy effects, which can occur in both water injection and abstraction, can be included as an additional skin factor (Dake, 1983). The total skin factor for a well combines the effects of the mechanical skin, completion pseudoskin and geometrical pseudoskin. Yildiz (2006) summarised the available methods and software to predict the total skin factor in fully penetrated vertical wells. However, there has not yet been an attempt to analytically model non-Darcy flow in closed domains using the Forchheimer equation.

2.2.2 Multiple well systems

If the pressure buildup in a reservoir or aquifer needs to be maintained below some limiting value, it may be necessary to consider multiple well systems (MWS). A methodology for estimating the limiting pressure at which the formation starts to fracture can be found in Mathias et al. (2009b). For linear problems (Stephenson and Radmore, 1990), solutions for MWS can be obtained by implementing the principle of superposition (Schwartz and Zhang, 2002). However, when one is interested in non-Darcy flow, linearity no longer applies (Mathias et al., 2008). For such situations, an alternative method for MWS is required.

Compared to the vast of literature on the modelling of single-well systems, there is limited work on modelling MWS. Nordbotten et al. (2004) analysed potential leakage of injected waste fluids through abandoned wells. Results of the study showed that a system of multiple passive wells in the vicinity of an injection well behaves nonlinearly due to interaction between leaky wells. Consequently, the overall leakage rate per well in the system was reduced. Pech and Novotny (2005) and Novotny and Pech (2005) derived relations for a composite drawdown in MWS and wells near hydrological boundaries, respectively. In both studies, the principle of superposition was implemented in an analytical solution derived to include well skin losses. However, the accuracy of these results was not demonstrated by comparison with numerical simulation or experimental data. Mijic (2009) presented the analysis of MWS under steady state non-Darcy flow conditions. The analytical solution obtained can be used where there is no influence of the flow boundary on the pressure buildup at the well.

2.3 CO₂ injection in saline aquifers

In CO₂ storage projects, the issue of pressure buildup is particularly important (Rutqvist et al., 2008; Mathias et al., 2009b). In order to inject CO₂ into a storage formation,

the downhole pressure has to be higher than the reservoir fluid pressure. However, the increment in pressure could lead to deformation of the reservoir or the seal rock. This could induce fractures in the formation and lead to CO₂ leakage. Therefore, the critical pressure that develops at the injection well can significantly limit the aquifer storage capacity and is one of the most important criteria for screening and selection of potential CO₂ storage sites (Metz, 2005).

The behaviour of the injected gas can be modelled numerically, using either field scale simulators (Pruess, 1987; Schlumberger, 2002) or problem-specific models (Mathias et al., 2009a). Many studies analysed the pressure buildup during field-scale CO₂ injection. Rutqvist et al. (2007) used coupled fluid flow and geomechanical fault activation models to analyse the maximum sustainable injection pressure during CO₂ injection. The results showed that the main advantage of numerical modelling compared to simplified analytical estimations is in more accurate representation of structural geometry and its effects on spatial distribution of the fluid pressure. Taking into account the formation heterogeneity in a form of a multilayered groundwater system, Birkholzer et al. (2009) showed that the significant pressure increase can occur at more than 100 km away from the injection well. The pressure increase in vertical direction, however, showed to be important only in formations with highly permeable ($> 10^{-18} \text{ m}^2$) sealing units. Another interesting aspect related to pressure increase is the effect of the boundary condition used in simulations (Cavanagh and Wildgust, 2011). Analysis of formations with low permeability shales at a regional scale have shown that a boundary permeability of about 10^{-18} m^2 is likely to enable adequate pressure dissipation and allow for CO₂ to be injected at sufficient rates. Heinemann et al. (2012) analysed the CO₂ storage capacity of the offshore UK North Sea Bunter sandstone formation. The results indicated that neglecting fluid pressure increase during CO₂ injection can result in over-estimation of the gas storage capacity. It is worth mentioning that even the state-of-the-art numerical simulators cannot always predict accurately the field-scale behaviour of the injected gas. Examples from three demonstration projects (Sleipner, In Salah and Snøhvit) showed that in highly heterogeneous reservoirs, the actual CO₂ plume development is strongly controlled by geological factors, and therefore the monitoring data are necessary for reservoir characterisation and accurate pressure estimations (Eiken et al., 2011).

Conversely, CO₂ injection problems are often analysed using analytical solutions to multiphase flow. Although a simplified approach limits their application for the analysis of specific field storage problems, analytical solutions improve the understanding of how

specific aspects of the physics affect the injection process. Furthermore, they can be used as a benchmark to verify numerical solutions that take into account the full physics of the analysed problem and/or they can be used as a part of a numerical scheme to speed up the calculations (Juanes and Lie, 2007). Finally, analytical solutions are efficient tool for fast screening and ranking of aquifers suitability for CO₂ injection.

Estimations of reservoir pressure and lateral plume extent will vary significantly depending on the underlying assumption of the model applied. The basic modelling approach is to assume phase immiscibility, that is complete insolubility between CO₂ and brine. These models are a good approximation of water-oil displacement (Buckley and Leverett, 1942; Dake, 1983). However, modelling of gas-liquid systems requires modification of the approach to account for the partitioning of water and CO₂ between phases. This can be achieved by implementing solutions to miscible two-phase flow (Orr, 2007). Finally, at reservoir conditions CO₂ compressibility can potentially influence pressures and position of the gas front (Vilarrasa et al., 2010). The remainder of the chapter reviews the existing modelling approaches to CO₂-brine displacement and the mathematical theory behind the models.

2.3.1 Analytical solutions for pressure buildup

Existing analytical models for the pressure buildup and CO₂ plume size estimation in brine aquifers were developed assuming confined and homogeneous formations under isothermal conditions. Two main approaches have been developed previously, which are discussed in more detail below.

Segregated flow approach

In displacement theory, if gravity forces are assumed to be more dominant than viscous forces, the displacement occurs under the so-called segregated flow condition (Dake, 1983). The phases are assumed to be separated by a sharp interface, and at any point on the interface, the pressures in two phases are assumed to be equal. Therefore, there is no capillary transition zone. Gravity forces determine the distribution of the fluids within the reservoir, so that the vertical variations in saturations are significant. The displacement is governed by vertical equilibrium, that is the flow is predominantly horizontal and results from the Darcy or viscous forces. The mixture of fluid phases is represented as a single fluid, which has a characteristic mobility that governs the total flux of the mixture. Finally, the phases are assumed to flow with effective permeability that equals to the product of

absolute permeability and the end point relative permeability of the phase. Consequently, the thickness averaged relative permeability in the segregated flow approach is a linear function of phase saturation.

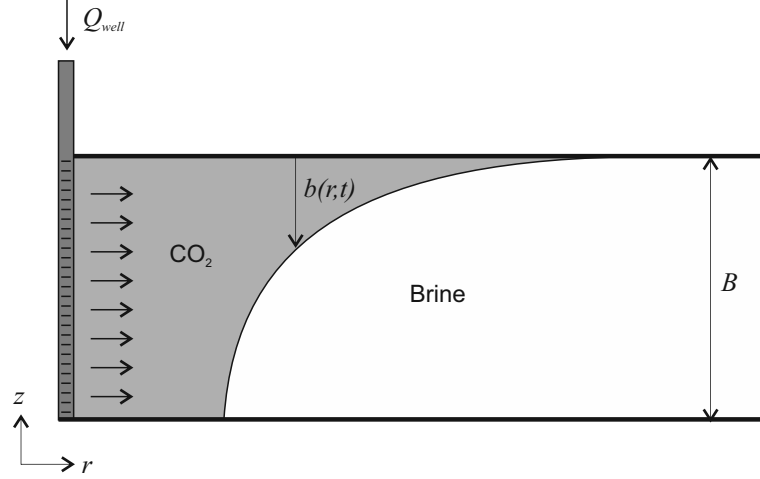


Figure 2.3: Typical CO₂ profile under segregated flow conditions (Nordbotten et al., 2005).

The segregated flow approach has been used in oil industry since the 1950's (Dietz, 1953). Nordbotten et al. (2005) were the first to apply this approach to the CO₂ sequestration problem. The analytical solution for the plume evolution during CO₂ injection in an infinite formation was obtained by minimising the pressure buildup at the well while imposing the volume constraint. The model assumes negligible capillary pressure, fluid immiscibility and incompressibility, constant phase saturations within gas and liquid zones, and vertically integrated properties applied to the composite fluid. The resulting CO₂ profile is shown in Figure 2.3. The similarity solution of Nordbotten et al. (2005) was extended by Nordbotten and Celia (2006) to include slight miscibility between the two fluids. Dentz and Tartakovsky (2009) developed an approximate analytical solution for the interface dynamics during CO₂ injection that explicitly incorporates effects of buoyancy.

The segregated flow approach was further developed by Mathias et al. (2009a), who derived a new analytical solution that describes the full temporal and spatial pressure distribution during CO₂ injection. Furthermore, the late time transient approximation of the solution was extended to account for non-Darcy effects using the Forchheimer equation. Building on the solution for infinite formations, Mathias et al. (2011b) presented an explicit approximate solution for estimating pressure buildup due to the injection of CO₂ in a closed

brine aquifer of finite radial extent under Darcy flow conditions. In Mathias et al. (2011a), the pressure buildup equations of Mathias et al. (2011b) were extended to account for CO₂ partial miscibility. Gray et al. (2011) derived the vertical equilibrium model to describe the mitigation of CO₂ injected into an aquifer of variable thickness.

Several authors have analysed the effects of CO₂ compressibility on the sharp-interface solutions. Nordbotten and Celia (2006) suggested the iterative procedure to obtain the fluid properties that correspond to the pressures obtained at the end of the simulation, though the results of such procedure have not been shown. Vilarrasa et al. (2010) obtained expressions for the vertically averaged pressure for the both Nordbotten et al. (2005) and Dentz and Tartakovsky (2009) solutions. These expressions were used to obtain the average gas phase density. The compressibility correction was implemented through the iterative procedure that minimises the error between the mean density used to obtain input fluid properties and the mean density obtained from reservoir pressures at the end of the simulation. They have found that the error in the interface position caused by neglecting CO₂ compressibility is significant when gravity forces dominate. Mathias et al. (2011a) and Mathias et al. (2011b) re-evaluated their approximate solutions to account for CO₂ compressibility by recalculating fluid properties based on the well pressure that occurs when the pressure disturbance reaches the outer reservoir boundary.

Results for both immiscible and miscible models showed good agreement with commercial model simulations, which include results from ECLIPSE (Nordbotten et al., 2005), CODE BRIGHT (Vilarrasa et al., 2010) and TOUGH2 (Mathias et al., 2011b). However, segregated flow models have been shown to be inaccurate when estimating the abrupt interphase position for high CO₂ injection rates, and for analysis of near-well effects (Lu et al., 2009), when flow is no longer gravity dominated.

Diffuse flow approach

Under non-gravity dominated or so-called diffuse flow conditions, fluid saturations at any point in the displacement path are assumed to be uniformly distributed with respect to the formation thickness (Dake, 1983). This means that viscous forces dominate the displacement process and that the vertical variation in saturations can be neglected. This assumption permits the displacement to be mathematically represented as a one-dimensional problem. The diffuse flow conditions are valid when displacement occurs at very high injection rates and the effects of the capillary and gravity forces are negligible.

When applied to the CO₂ injection problem, the diffuse flow approach assumes that

three flow regions will form: 1) pure CO₂ region near the well, 2) intermediate two-phase zone and 3) far-field single-phase brine region. Pressure gradients within each region are obtained as a function of phase mobilities and the injection rate at any instant in time. Phase zone boundaries are determined by applying the fractional flow theory. The diffuse flow model allows for phase miscibility. However, both CO₂ and brine are assumed to be incompressible. The problem formulation is presented in Figure 2.4.

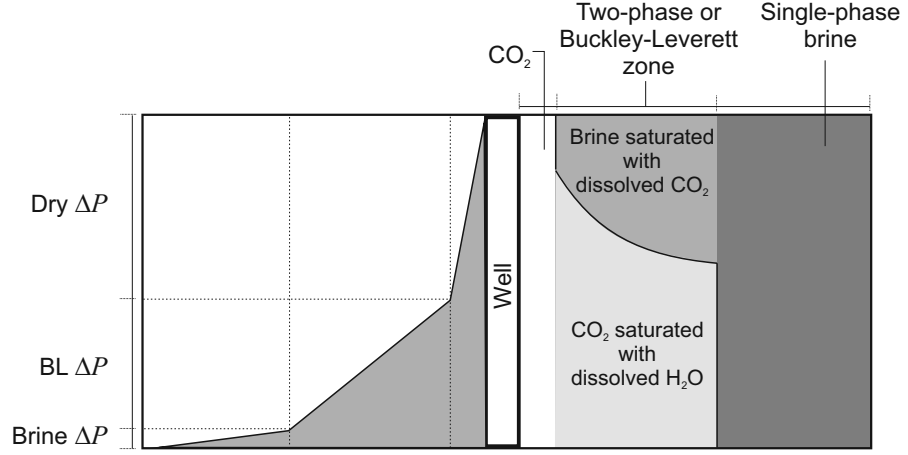


Figure 2.4: Flow regions during CO₂ injection under diffuse flow conditions and resulting pressure distribution (Burton et al., 2008).

Burton et al. (2008) implemented the fractional flow approach to examine the problem of time-dependent CO₂ injectivity. They assumed a constant pressure drop between the injection well and the far-field boundary under steady state flow conditions. The linear pressure distribution within the two-phase zone was a result of the simplified approach to calculation of the pressure buildup, which assumes phase mobilities obtained from the average zone saturation. The development of fronts that distinguish flow regions was determined by implementing the miscible fractional flow model for radial flow (Noh et al., 2007). Burton et al. (2008) concluded that CO₂ injectivity is influenced by the drying-out process that occurs near the well. In addition, it strongly depends on the mobility of the flow in the two-phase region. Hence, the characterisation of relative permeability functions is one of the key factors for the practical implementation of CO₂ storage projects.

The approach to pressure buildup modelling presented in Burton et al. (2008) was implemented by Ehlig-Economides and Economides (2010) to examine the feasibility of CO₂

storage in closed underground formations. The influence of the far-field no-flow boundary was modelled by changing the last term in the expression for pressure buildup given by Burton et al. (2008). The findings given by Ehlig-Economides and Economides (2010) suggest that CO₂ sequestration is not a practical means of providing any significant reduction in CO₂ emissions. Such an extreme conclusion was strongly argued against by Cavanagh et al. (2010) and Chadwick et al. (2010). Both studies showed that questionable numerical values, conceptual analogies and boundary condition assumptions led to the misleading calculations regarding the pressure response during CO₂ injection.

The analysis of the compressibility effects in viscous dominated flow have not yet been presented.

It is worth mentioning that there are a few other approaches in the literature that deal with the pressure buildup problem in a more simplified manner. Saripalli and McGrail (2002) suggested a semi-analytical model for immiscible displacement, which defines the radius of the two-phase zone around the injector based on the average CO₂ saturation. The pressure distribution is modelled as a steady state problem considering the pressure increase only within the two-phase region. Zhou et al. (2008) developed a method for the assessment of CO₂ storage capacity in semi-closed and closed formations. They assumed that the storage capacity is a function of the pore and brine compressibilities only. The study presented an equation that can estimate the domain-average pressure buildup in closed formations based on the pore volume needed to store the injected CO₂.

In the diffuse flow approach, the solution for pressure buildup during CO₂ injection is strongly dependent on the saturation change within the reservoir. Phase saturations determine relative permeability functions and hence the flow mobility within the two-phase region. The mathematical theory behind the two-phase modelling is discussed in more detail below.

2.3.2 Two-phase flow modelling

There are two basic concepts in two-phase displacement modelling. When two fluids cannot mix and hence separate into two phases with an interface between them, the process is referred to as an immiscible displacement (Dake, 1983). Typical example of an immiscible process is the oil recovery resulting from displacement by water. However, when a gas is injected into a porous formation, components in the gas can dissolve in the resident liquid phase, and components in the liquid can transfer to the vapour, forming a local chemical equilibrium. Such miscible displacements are modelled taking into account the resulting

compositional changes that occur in such processes (Orr, 2007). Both concepts are based on the assumption of phase incompressibility.

Immiscible displacement

The fundamental principle in the analytical modelling of the two-phase displacement in porous media is the Buckley and Leverett (1942) formulation. The solution was derived for immiscible water-oil systems and describes the processes that affect the two-phase displacement. By introducing the concept of fractional flow, the Buckley and Leverett (1942) equation states that the rate of advance, that is the characteristic velocity of a front that has a fixed saturation, is proportional to the change in fractional flow caused by a small change in saturation of the displacing phase:

$$\frac{\partial S_h}{\partial t} + \frac{Q}{A\phi} \frac{\partial f_h}{\partial x} = 0 \quad (2.9)$$

where S is the phase saturation, A is the cross-sectional area of the formation unit, x is linear distance from the injection well and f is the fractional flow function defined as:

$$f_h = \frac{q_h}{q} \quad (2.10)$$

Subscript h denotes the water phase. Equation (2.9) is valid in one-dimensional (1D) homogenous reservoirs, under the assumptions of horizontal and incompressible flow and negligible capillary pressure. Typical fractional flow curve, and the corresponding characteristic velocity, df_h/dS_h , are shown in Figure 2.5.

The Buckley and Leverett (1942) equation is a form of a scalar hyperbolic conservation law with a non-convex flux function (LeVeque, 1992). If the initial state can be defined with piecewise constant data that have a single discontinuity, its combination with the conservation law leads to a Riemann problem (LeFloch, 2002). For the injection of pure water in an oil reservoir with connate water saturation, the solution for the Buckley-Leverett problem shown in Figure 2.6a can be constructed by following the characteristics for each saturation. This is known as the method of characteristics (MOC). The MOC reduces a partial differential equation to a family of ordinary differential equations, which can be integrated for a defined set of input data (LeVeque, 1992).

The saturation profile obtained, however, is a physically impossible solution for two reasons: 1) characteristics associated with the initial discontinuity intersect those from

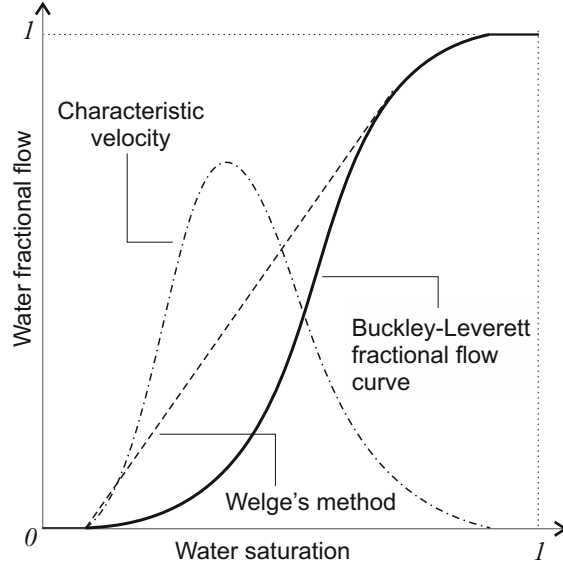


Figure 2.5: Fractional flow function for immiscible water-oil displacement (Buckley and Leverett, 1942) and the Welge (1952) method for the shock saturation.

the initial saturation (Figure 2.6c) and 2) there are two saturations that have the same characteristic velocity, which indicates that two different phase saturations can exist at the same location within the reservoir. To find a unique solution, it is necessary that a saturation discontinuity or a shock front forms.

The shock location can be determined by the so-called equal area rule (LeVeque, 1992; Whitham, 2011), where the integral of the discontinuous weak solution (solid line in Figure 2.6b) must be the same as the area under the multivalued profile (dashed line in Figure 2.6b). Welge (1952) integrated the Buckley-Leverett saturation profile over the distance from the injection point to the front and concluded that the shock to the fractional flow curve from the initial state must have a point of tangency that defines the shock front saturation. Therefore, the shock front saturation can be obtained easily once the fractional flow function is known (Figure 2.5).

The characteristics for the problem defined above are shown in Figure 2.6c. The velocity of the shock can be found by satisfying the conservation of volume across the shock, that is, the Rankine-Hugoniot or jump condition (LeVeque, 1992). Figure 2.7 shows that the change in the amount of a phase present in the control volume is proportional to the net inflow of that phase. Moreover, the unique solution for the non-convex function must satisfy the Oleinik entropy condition. The entropy condition states that wave velocities on the upstream side of the shock must be greater or equal to the shock velocity, while

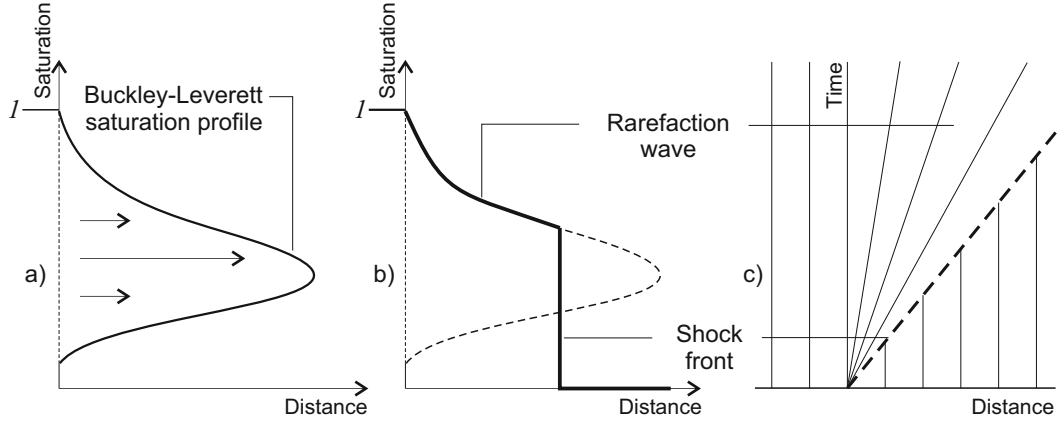


Figure 2.6: Riemann solution for Buckley and Leverett (1942) equation (LeVeque, 1992): a) triple-valued saturation profile, b) unique solution with a shock front and c) characteristics for the discontinuity present initially at the inlet and for the initial saturation.

the shock has to move faster than the saturations downstream of it (Orr, 2007). Both the Rankine-Hugoniot and Oleinik entropy conditions are implemented through the equal area rule. Amongst others, implementation of the MOC for the analysis of immiscible oil and gas recovery processes is given by Bedrikovetsky (1993).

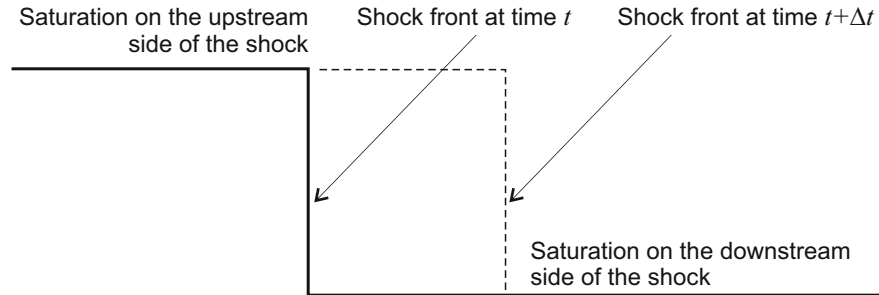


Figure 2.7: Motion of a shock during diffuse flow displacement (Orr, 2007).

The Buckley and Leverett (1942) solution assumes that the flow in the porous formation is governed by Darcy's law. However, the flow conditions in a two-phase system can also transfer from linear to non-Darcy. Non-Darcy flow conditions in water-oil systems have been examined by several authors. Numerical solutions were given by Wu (2002b) and Ahmadi et al. (2010). Wu (2001) presents the analytical solution for the water saturation profile in non-Darcy two-phase flow, assuming that both phases flow under non-Darcy conditions in a 1D system. The model shows that the Forchheimer displacement is con-

trolled not only by relative permeability curves, but also by the level of inertial losses and the flow injection rate. More recently, solutions for radial and 1D flow systems based on non-Darcy flow models of Forchheimer (1901) and Barree and Conway (2004) were given by Wu et al. (2010). Barree and Conway (2004) proposed a physically-based model for non-Darcy flow assuming the variable formation permeability and variable Forchheimer coefficient. Wu et al. (2011) developed the general analytical and numerical solution with the Barree and Conway (2004) model. The solutions presented contribute significantly to the understanding of the two-phase flow under non-Darcy conditions. However, they assume that the same fractional flow function applies to the whole displacement and hence non-Darcy parameters dominate the displacement process even when the shock front has moved further away from the injection well. This models a 1D coreflood, but it is incorrect for spatially varying radial non-Darcy displacement.

The problem of fractional flow function dependence on parameters other than saturation can be found in the analysis of the water-drive displacement of non-Newtonian oils (Bedrikovetsky, 1993). In that work, it is assumed that the water phase is a Newtonian fluid which displaces non-Newtonian oil with an arbitrary nonlinear flow behaviour. The Buckley and Leverett (1942) solution can be applied, but in this case the fractional flow curve is a function of the displacement velocity. The application of this approach to improved oil recovery analysis can be found in Rossen et al. (2011). They extended the fractional flow theory to non-Newtonian fluids where fluid viscosity changes with a radial position and implemented it to the modelling of foam and polymer displacement processes.

Miscible displacement

Injection of CO₂ in saline formations induces several processes, such as multiphase fluid flow, chemical reactions and precipitation of solid salt. If chemical reactions include equilibrium partitioning of a water and CO₂ components between the liquid and gas phases, then a generalisation of the problem of two-phase displacement solved by Buckley and Leverett (1942) is needed. Assuming that the pressure at which the phase equilibrium is evaluated is taken to be constant and that effects of adsorption and temperature variation are not included in the flow problem considered, the solution for the two-component gas-oil displacement using the MOC can be found in Orr (2007). A typical gas phase fractional flow curve as a function the overall fraction of the gas component is shown in Figure 2.8. Within the two-component region, the fractional flow function has the shape typical for

the two-phase displacement. In single-phase regions, the fractional flow is a linear function of composition, which means that the total flow velocity is equal to the Darcy velocity of the phase. Hence, the characteristic velocity is constant and equal to 1.

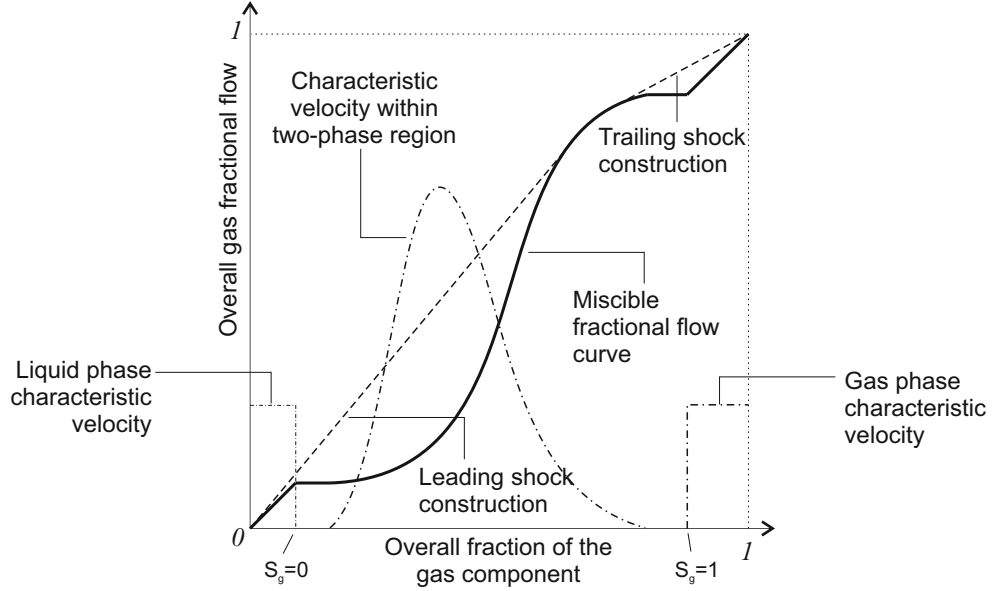


Figure 2.8: Fractional flow function for miscible gas-oil displacement (Orr, 2007).

The Riemann solution for the miscible displacement consists of two shock fronts and a rarefaction wave (Figure 2.9). Characteristics of the initial composition determine the leading shock front, while the trailing shock determines the near-well zone where the composition is equal to the injection composition.

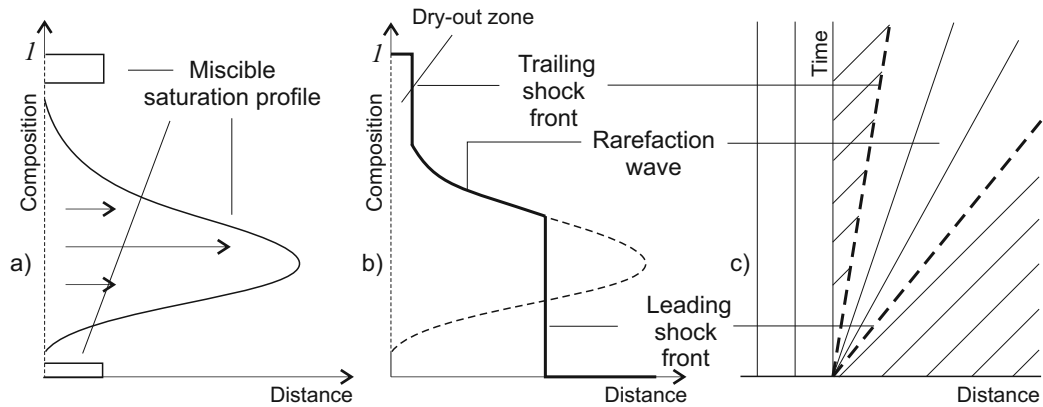


Figure 2.9: Riemann solution for miscible gas-liquid displacement.

Miscibility of gas with water leads to CO₂ partially dissolving in brine, and water partially vaporising in the gas phase. A physical formulation of the CO₂-brine system can be found in Prévost et al. (2004), Fuller et al. (2006) and Zeidouni et al. (2009). The problem that is considered is one-dimensional CO₂ injection in an infinitely large saline aquifer through a well located in the centre of the formation. The system is fully represented by a three-phase (gas, liquid and solid), three-component (CO₂, water and salt) displacement. Although such analysis are implemented in the numerical (Giorgis et al., 2007; Pruess and Spycher, 2007) and thermodynamic (Fuller et al., 2006) models for salt precipitation, all analytical solutions presented so far consider the approximation of the system by a two-phase (gas and liquid), two-component (CO₂ and brine) problem. In such a case three regions will form (see Figure 2.4): 1) gas phase zone between the injection well and the trailing shock, the so-called dry-out zone, 2) two-phase zone between the trailing and the leading shock and 3) liquid phase zone ahead of the leading shock (Noh et al., 2007; Zeidouni et al., 2009; Mathias et al., 2011a). To solve the problem of fluid dynamics in two-phase flow, it is necessary to determine the fluid properties and phase change effects in the water-salt-CO₂ system.

Thermodynamics of water-salt-CO₂ systems

Models for solving viscous-dominated flows are based on the assumption of local chemical equilibrium, which means that the phases that form are determined by the pressure, temperature and overall composition of the fluid (Orr, 2007). It is therefore necessary to obtain pressure-temperature-composition correlation (that is, equation of state) for water-salt-CO₂ mixtures in the pressure and temperature range of geological CO₂ storage.

Based on the published experimental data, Spycher et al. (2003) presented a non-iterative procedure to calculate the composition of CO₂ and liquid phases at equilibrium, using the Redlich and Kwong (1949) equation of state. CO₂-water phase diagram at the fixed temperature, including locations of the literature data used in the study, is shown in Figure 2.10. The narrowness of the three-phase region indicted its unimportance for geological sequestration. Furthermore, the model suggests that water solubility in the gas phase is only a fraction of percent. To account for effects of chloride salts in liquid phase, Spycher and Pruess (2005) included the activity coefficient for liquid CO₂ in the original formulation of Spycher et al. (2003). Equations implemented in Spycher et al. (2003) and Spycher and Pruess (2005) models are discussed in more detail in Section 5.3.1.

From compositional analysis it can be seen that the implementation of fluid properties in water-salt-CO₂ system usually includes only two phases: a liquid phase and a gas (CO₂-rich) phase, the latter one having a liquid-like density (supercritical CO₂) for pressures and temperatures above the critical point ($T_c = 31.04^\circ\text{C}$ and $P_c = 7.382\text{ MPa}$ (Vargaftik, 1975)). Liquid phase contains salt component, which may dissolve in brine or precipitate as a solid component. In a miscible displacement, liquid phase may contain dissolved CO₂, and the brine may vaporise into the gas phase. Correlations that can be used for the calculation of fluid properties and consequences of implementing simplifying assumptions regarding the thermodynamic behaviour are discussed in more detail in Sections 4.3.1 and 5.3.2.

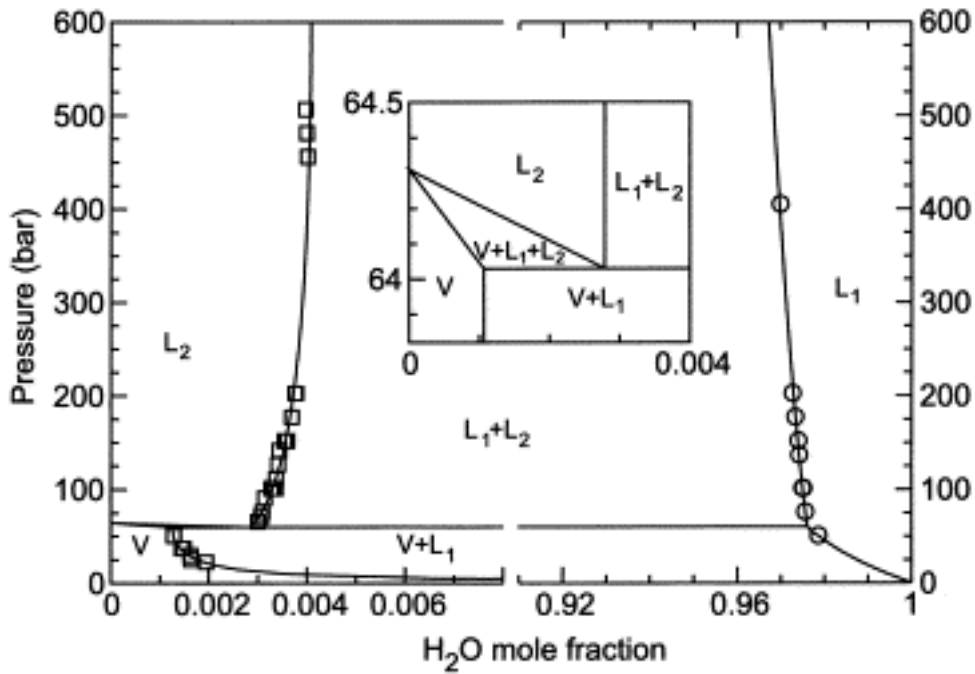


Figure 2.10: Pressure-mole fraction CO₂-water phase diagram at 25 °C. Phases labeled are: V - vapour phase, L₁ - water-rich liquid and L₂ - CO₂-rich liquid (Spycher et al., 2003).

Salt precipitation during CO₂ injection

Although the amount of brine that may vaporise in the flowing gas phase is in order of few percentiles (Figure 2.10), continuous injection of dry CO₂ into a saline formation may

lead to complete vaporisation of the resident brine and formation of the dry-out zone in the vicinity of the injection well. A vaporisation of formation brine may lead to even the irreducible water saturation to reduce to zero, which may increase the relative permeability of the liquid phase (Hurter et al., 2007). Two scenarios are possible – in low salinity brine environments, this process will result in injectivity enhancement, but in formations with high saline brines, this may cause precipitation of the dissolved salt and serious injectivity reduction (Giorgis et al., 2007; Pruess and Spycher, 2007; Pruess and Müller, 2009; Zeidouni et al., 2009).

Numerical simulations showed that the precipitation of solid salt occurs in the grid block with the highest rate of water vaporisation into flowing gas phase (that is, in the first grid block where the liquid phase is present), and that there is no precipitation in the two-phase region (Pruess and Spycher, 2007; Hurter et al., 2007; Pruess and Müller, 2009). The results showed that salt saturation in the dry-out region is constant and independent of injection rate. Finally, it was suggested that a brief preflush with fresh water to displace precipitated salt away from the injection well may be beneficial for CO₂ injectivity.

Based on the results from numerical models, analytical solutions for salt precipitation were developed. Existing analytical models (Burton et al., 2008; Pruess and Müller, 2009; Pruess, 2009; Zeidouni et al., 2009; Mathias et al., 2011a) are all based on the assumption that salt precipitation will occur due to the vaporisation of brine across the trailing shock into the flowing gas phase. The reason is because in the approximation of the problem by a two-phase two-component system, all the saturations with velocities lower than the trailing shock velocity will not appear in the solution. Hence, CO₂ will dry out the region in the vicinity of the injection well once the brine saturation approaches the one downstream of the trailing shock (Zeidouni et al., 2009). In the models, there is no mass transfer between the saturated liquid phase in the two-phase zone and saturated gas phase ahead of the trailing shock. Therefore, there is no salinity change in the CO₂-brine region. All the solid salt will precipitate within the dry-out zone and its saturation can be determined as a function of the liquid phase saturation downstream of the shock.

Having defined the value of solid phase saturation, it is possible to determine the reduction in the formation permeability due to salt precipitation and analyse its influence on CO₂ injectivity. The authors, however, applied different approaches to determine the gas and hence the liquid phase shock saturations. Pruess (2009) implemented the Buckley and Leverett (1942) fractional flow theory for immiscible displacement. As phase immiscibility implies the existence of the leading shock only, he suggested an iterative procedure for

obtaining the gas saturation at the dry-out front. Burton et al. (2008) applied the Buckley and Leverett (1942) formulation modified by Noh et al. (2007), which accounts for partial CO₂-brine solubility. Finally, Zeidouni et al. (2009) and Mathias et al. (2011a) accounted for CO₂ and water partitioning in both phases and the volume change upon mixing by extending the model for gas-liquid displacement problem given by Orr (2007).

2.4 Conclusions

In this chapter, following introductory sections on the basic concepts of the flow in single and two-phase subsurface systems, the summary of work that has been carried out to analytically model the behaviour of water and CO₂ once they are injected into an underground formation has been presented. This shows that the estimation of the critical pressure buildup at the well is of great importance for the analysis of single-phase systems (Mathias et al., 2008), as well as for the estimation of the CO₂ storage capacity (Metz, 2005).

Analytical models for the pressure buildup in single-phase systems are well known. However, this is true only for when water is assumed to flow under Darcy flow conditions, when equations given by Thiem (1906) and Theis (1935) can be implemented. Modelling of flow under non-Darcy flow conditions, which include viscous effects that occur at high flow velocities, requires the modification of the governing equations. Existing analytical models for the non-Darcy flow using the Forchheimer (1901) equation include the steady-state solution given by Bear (1979) and late transient approximations (Şen, 1988; Kelkar, 2000; Wu, 2002a; Mathias et al., 2008). These solutions, however, cannot model Forchheimer flow in closed domains, nor the pressure buildup under non-Darcy conditions in a system of multiple wells.

Solutions for two-phase flow, which can analytically model CO₂ injection into saline aquifers, can be obtained by applying the segregated flow approach. Although these models include effects such as miscibility (Nordbotten and Celia, 2006; Mathias et al., 2011a), buoyancy (Dentz and Tartakovsky, 2009), compressibility (Vilarrasa et al., 2010), no-flow boundary (Mathias et al., 2011b) and non-Darcy large time approximation (Mathias et al., 2009a), their application is limited by the assumption of the gravity-dominated flow. These solutions are thus most useful in the analysis of the long term movement of thin CO₂ plumes (Nordbotten and Celia, 2006; Gasda et al., 2009; Gray et al., 2011).

Analytical solutions based on fractional flow theory and the Buckley and Leverett (1942) model can be used for analysis of near-well effects, such as salt precipitation (Zei-

douni et al., 2009) and non-Darcy immiscible flow (Wu et al., 2011). The latter model, however, assumes one-dimensional, linear displacement, and that non-Darcy flow of both water and oil phases dominates the displacement process regardless of the position within the reservoir. The two-phase flow solutions that are based on the diffuse flow approach cannot model compressible flow.

The literature review presented in this chapter shows that many important aspects regarding water injection and CO₂ storage problems are addressed in the work undertaken so far. However, the application of analytical models presented is limited by assumptions made for their derivation (segregated flow solutions), flow geometry (one-dimensional core-flood solutions) and by covering only one of the aspects that can have a significant impact on a pressure buildup and flow movement in the subsurface. Therefore, the key research questions that arise from this literature review are:

- What is the influence of a no-flow boundary on the well pressure under non-Darcy conditions, and can a single-well solution be implemented in the multiple well system analyses?
- If non-Darcy flow varies with the distance from the well, how can this be modelled analytically and what are the implications on saturation and pressure distributions during CO₂ injection?
- How can analytical solutions for CO₂ plume extent and pressure buildup estimations be formulated and combined to model miscible, compressible, non-Darcy flow in closed and open formations?
- How important are the different near-well effects, and what controls CO₂ injectivity?

Chapter 3

Non-Darcy flow in single-phase closed and/or multiple well systems

3.1 Introduction

In the previous chapter a review of research on non-Darcy flow in single-phase systems showed that numerous researchers have developed both analytical and numerical solutions to explore this issue. However, the Forchheimer (1901) equation has not yet been applied in the analytical modelling of bounded domains and/or multiple well systems (MWS).

The work that is presented in this chapter seeks to further develop existing analytical solutions to account for the influence of the no-flow boundary in confined domains under non-Darcy flow conditions. Starting from the mass balance equation for slightly compressible flow, the analytical solution for Forchheimer flow and finite aquifer formations is derived. Furthermore, a hypothesis for the implementation of the obtained solution in the analysis of MWS is proposed. The model is verified with numerical simulations of the original problem. The numerical model is an extension of the steady state finite difference solution presented in Mijic (2009). A two-dimensional scheme is modified to simulate transient flow and account for the effects of the closed boundary. Finally, the applicability of the approach to unconfined aquifers is discussed.

3.2 Forchheimer flow to a well in a closed domain

Non-Darcy flow conditions can be described using the Forchheimer (1901) equation:

$$\frac{\mu q}{k} + \rho b |q| q = -\frac{dP}{dr} \quad (3.1)$$

where μ is dynamic viscosity, q is fluid flux, k is intrinsic permeability, ρ is fluid mass density, P is fluid pressure, r is radial distance from the injection well and b the Forchheimer coefficient. For low fluid fluxes, value of b approaches zero and equation (3.1) reduces to Darcy's law.

The governing mass conservation equation for radial single-phase, slightly compressible flow in a homogenous, isotropic and confined aquifer with the injection well centrally located can be written as (Dake, 1983):

$$\frac{\partial \phi \rho}{\partial t} + \frac{1}{r} \frac{\partial}{\partial r}(r \rho q) = 0 \quad (3.2)$$

where ϕ is formation porosity and t is time since the beginning of injection. If $c_r = \phi^{-1}(d\phi/dP)$ and $c = \rho^{-1}(d\rho/dP)$ are the compressibility of the rock and fluid, respectively (Wheater et al., 2010), then equation (3.2) becomes:

$$D \frac{\partial P}{\partial t} + \frac{1}{r} \frac{\partial}{\partial r}(r q) = 0 \quad (3.3)$$

where $D = \phi(c_r + c)$ is the pressure domain specific storage coefficient. If equation (3.3) would be expressed in terms of the hydraulic head ($h = P/(\rho g)$), then the pressure domain specific storage coefficient would revert to the more standard definition of the specific storage, that is $\phi \rho g(c_r + c)$. Details of the derivation of equation (3.3) are presented in Appendix B. The relevant initial and boundary conditions are:

$$\begin{aligned} P &= P_0 & r &\geq r_w & t &= 0 \\ q &= \frac{Q}{2\pi H r_w} & r &= r_w & t &> 0 \\ q &= 0 & r &= r_e & t &> 0 \end{aligned} \quad (3.4)$$

where P_0 is the initial fluid pressure, Q is the volumetric injection rate, H is the formation thickness, r_w is the well radius, and r_e is the radial extent of the reservoir unit.

3.2.1 Analytical solution for a single well

After pressure perturbation has reached the boundary, the change in pressure with time is relatively uniform (Dake, 1983), so that:

$$\frac{\partial P}{\partial t} = \frac{Q}{AHD} \quad (3.5)$$

where $A = \pi(r_e^2 - r_w^2)$ is the plan area of the reservoir unit. Substituting equation (3.5) into equation (3.3) leads to:

$$\frac{Q}{AH} + \frac{1}{r} \frac{\partial}{\partial r}(rq) = 0 \quad (3.6)$$

Substituting in equation (3.1), integrating with respect to r and applying the no-flow boundary at $r = r_e$ gives:

$$\frac{dP}{dr} = \frac{Q\mu}{2kAH} \left[r - \frac{r_e^2}{r} - \frac{Qk\rho b}{2\mu AH} \left(r - \frac{r_e^2}{r} \right)^2 \right] \quad (3.7)$$

Integrating equation (3.7) and setting $P = P_w$ at $r = r_w$ leads to:

$$P - P_w = \frac{Q\mu}{2kAH} \left\{ \frac{r^2 - r_w^2}{2} - r_e^2 \ln \left(\frac{r}{r_w} \right) + \frac{Qk\rho b}{2\mu AH} \left[2r_e^2(r - r_w) + \frac{r_e^4}{r} - \frac{r_e^4}{r_w} - \frac{r^3 - r_w^3}{3} \right] \right\} \quad (3.8)$$

Equation (3.8) can be expressed in terms of the average reservoir pressure, which can be obtained from (Dake, 1983):

$$\bar{P} = \frac{2\pi}{A} \int_{r_w}^{r_e} rP dr \quad (3.9)$$

Substituting equation (3.8) into (3.9), evaluating the integral and rearranging for P_w then gives:

$$P_w = \bar{P} - \frac{\pi Q\mu}{kA^2H} \left[\frac{r_e^4}{8} - \frac{r_w^4}{8} - \frac{r_e^4}{2} \ln \left(\frac{r_e}{r_w} \right) + \frac{(r_e^2 - r_w^2)^2}{4} + \frac{Qk\rho b}{2\mu AH} \left(\frac{24r_e^5}{15} - \frac{r_e^6}{2r_w} + \frac{r_e^2 r_w^3}{2} - \frac{3r_e^4 r_w}{2} - \frac{r_w^5}{10} \right) \right] \quad (3.10)$$

Once a semi-steady state is reached, the average pressure can be approximated from the material balance for the closed domain given by equation (3.5) (Dake, 1983):

$$\bar{P} = \frac{Qt}{AHD} + P_0 \quad (3.11)$$

Recalling that $A = \pi(r_e^2 - r_w^2)$ and assuming $r_e \gg r_w$ leads to:

$$P_w - P_0 = \frac{Qt}{\pi r_e^2 HD} + \frac{Q\mu}{2\pi kH} \left[\ln \left(\frac{r_e}{r_w} \right) - \frac{3}{4} \right] + \frac{Q^2 \rho b}{(2\pi H)^2 r_w} \left(1 - \frac{16r_w}{5r_e} \right) \quad (3.12)$$

Equation (3.12) is the solution for non-Darcy pressure buildup at the well once the semi-steady state conditions become valid.

The critical time at which the semi-steady state assumption becomes valid, t_c can be found by equating equation (3.12) with equation (3.15) and assuming that $4kt_c/\mu Dr_e^2 \ll 1$, which is valid for typical values of formation properties (permeability of order $k \approx 10^{-13} \text{ m}^2$, porosity of $\phi \approx 0.1$ and rock compressibility of order $c_r \approx 10^{-9} \text{ Pa}^{-1}$):

$$t_c = \frac{\mu Dr_e^2}{4k} \exp\left(0.5772 - \frac{3}{2}\right) \exp\left(\frac{4kt_c}{\mu Dr_e^2}\right) \approx 0.2423 \frac{\mu Dr_e^2}{k} \quad (3.13)$$

A late time analytical approximation for the Forchheimer flow, when r_e can be assumed infinite, was derived by Mathias et al. (2008):

$$P - P_0 = \frac{Q\mu}{4\pi Hk} \left[\ln\left(\frac{4kt}{\mu Dr^2}\right) - 0.5772 \right] + \frac{Q^2 \rho b}{(2\pi H)^2 r} \quad (3.14)$$

The above expression for the reservoir pressure, P (in Pa) consists of Jacob's late-time approximation for transient Darcy flow (Dake, 1983) and the additional term that represents the contribution of the Forchheimer flow to the pressure buildup. A similar structure of the solution for non-Darcy flow, formulated as a superposition of the Darcy flow solution and a non-Darcy term, was also found by Wu (2002a). In this study, the late time solution for the Forchheimer flow from a well in closed domains, before the pressure perturbation has reached the boundary, is approximated such that:

$$P_w - P_0 \approx \frac{Q\mu}{4\pi Hk} \left[\ln\left(\frac{4kt}{\mu Dr_w^2}\right) - 0.5772 \right] + \frac{Q^2 \rho b}{(2\pi H)^2 r_w} \left(1 - \frac{16r_w}{5r_e} \right) \quad (3.15)$$

The second term on the right-hand side of equation (3.15) is assumed to be the contribution of the non-Darcy flow to the well pressure increase in closed formations.

Under Darcy flow conditions, the late transient transition time, t_0 , can be found as a function of the well radius (Dake, 1983). During this time, the influence of the formation boundary begins to be felt at the well. Mathias and Todman (2010) showed that when flow is governed by the Forchheimer equation, the critical time for the initiation of the late transient approximation is a function of the Forchheimer coefficient, b , and can be found from:

$$t_0 \approx \frac{\mu Dr_w^2}{k} \left[\frac{1}{(7 \cdot 10^3)} \left(\frac{2\pi H r_w \mu}{Qk\rho b} \right)^2 + \frac{1}{(3 \cdot 10^7)} \left(\frac{2\pi H r_w \mu}{Qk\rho b} \right)^{1/2} \right]^{-1} \quad (3.16)$$

It follows that:

$$P_w - P_0 = \begin{cases} \frac{Q\mu}{4\pi Hk} \left[\ln \left(\frac{4kt}{\mu D r_w^2} \right) - 0.5772 \right] + \frac{Q^2 \rho b}{(2\pi H)^2 r_w} \left(1 - \frac{16r_w}{5r_e} \right), & t_0 < t < t_c \\ \frac{Qt}{\pi r_e^2 H D} + \frac{Q\mu}{2\pi k H} \left[\ln \left(\frac{r_e}{r_w} \right) - \frac{3}{4} \right] + \frac{Q^2 \rho b}{(2\pi H)^2 r_w} \left(1 - \frac{16r_w}{5r_e} \right), & t \geq t_c \end{cases} \quad (3.17)$$

3.2.2 Multiple wells without the principle of superposition

The nonlinearity in q (see equation (3.1)) implies that the principle of superposition is not valid under non-Darcy flow conditions. To solve this problem, an alternative approach to pressure buildup estimation has to be applied.

When analysing an equally spaced multiple well system, well interference has the most significant influence on the pressure buildup at the innermost well in the system (Zakrisson et al., 2008). Moreover, the aquifer hydraulic properties have to be uniform, which implies formation homogeneity. For such a system, the solution for the centrally located (critical) well could provide a limiting value of the pressure buildup, which determines the number and location of wells for the given injection rate. Figure 3.1 shows a possible layout in an array of equally spaced wells. Due to the interaction between the wells, the central well can be equivalently represented as a single well in a closed square domain of length equal to the well spacing interval L .

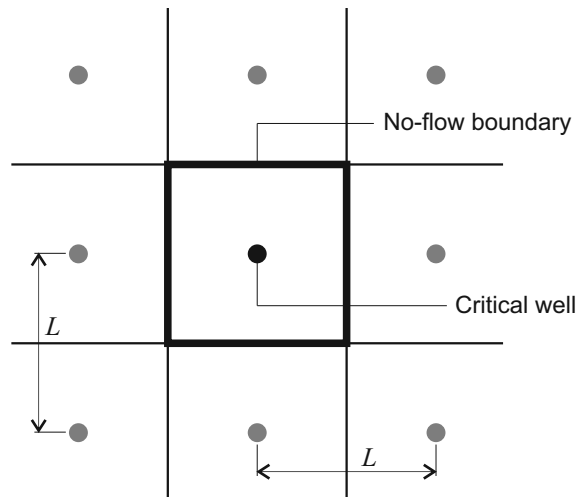


Figure 3.1: Schematic diagram of a multiple well system.

To account for different geometrical configurations, Dake (1983) presented the general form of inflow equation by introducing so-called Dietz shape factors (Dietz, 1965). This solution is valid only for times when the well is producing under semi-steady state conditions. In this study, it is hypothesised that the centrally located well is adequately represented by a single well situated in a closed circular region of equivalent plan area. Equation (3.17) can therefore be used to model this situation if it is assumed that the equivalent radius of the confined aquifer is related to the well spacing, L through:

$$r_e = \frac{L}{\pi^2} \quad (3.18)$$

Mathias et al. (2011b) invoked the same assumption for analysing the pressure buildup during CO₂ injection.

3.2.3 Numerical model

To assess the accuracy of the above solution, the response of equation (3.17) was compared to a finite difference solution in a square domain. Due to the loss of axial symmetry the problem becomes two-dimensional (2D). Hence, the number of grid-points required in the numerical solution is the square of those used in the numerical simulations previously presented by Mathias et al. (2008).

The continuity equation written for 2D flow takes the form (Wang and Anderson, 1995):

$$\frac{\partial q_x}{\partial x} + \frac{\partial q_y}{\partial y} = \delta_{i,j} \frac{Q}{\Delta x \Delta y H} - D \frac{\partial P}{\partial t} \quad (3.19)$$

where x and y are distances along orthogonal axis in the horizontal plane and δ is a dummy variable that is equal to 1 for a sink or a source term and 0 otherwise. In the scheme, the injection well with a flow rate Q is assumed to be centrally located at the origin node ($i = j = 1$), within the infinitesimal volume $\Delta x \Delta y H$ (first term on the right-hand-side of equation (3.19)). The corresponding dummy variable equals to $\delta_{1,1} = 1$. The Forchheimer equation that is used to substitute for q_x and q_y in equation (3.19) is written as:

$$q_x = -\frac{1}{\frac{\mu}{k} + \rho b |\vec{q}|} \frac{\partial P}{\partial x} \quad q_y = -\frac{1}{\frac{\mu}{k} + \rho b |\vec{q}|} \frac{\partial P}{\partial y} \quad (3.20)$$

where $|\vec{q}|$ is a magnitude of a flux vector in radial direction defined as:

$$|\vec{q}| = \sqrt{q_x^2 + q_y^2} \quad (3.21)$$

Mathias et al. (2008) were able to take advantage of the advanced adaptive time-grid solvers for one-dimensional solutions available in MATLAB. The need to solve a 2D problem, however, means that an alternative and more robust algorithm is required. In this study, the above equations are discretised using forward finite difference approximation. To ensure adequate resolution is obtained close to the well, the orthogonal spatial axes were discretised into N logarithmically spaced nodes. The finer grid resolution in the near-well region is necessary to capture significant pressure gradients that are expected under non-Darcy flow conditions. For the simulation of domains of infinite extent, Mathias et al. (2008) found it necessary to discretise the radial dimension into 2000 points. To accurately represent the finite domains studied here, grid refinement studies showed that 500 points were sufficient (therefore the total number of nodes that was used in each model was 250,000). The time scale was logarithmically discretised as well, to allow for the rapid pressure changes that occur during early times.

The no-flow boundaries were implemented using image nodes. The numerical scheme is able to represent both circular and square domains with a closed far-field boundary. In the circular model, image nodes are set at the radial distance from the well equal to r_e . The far-field boundary condition for a square reservoir unit is set at the constant length of $L/2$ in both x and y directions. A schematic diagram of the numerical grid is presented in Figure 3.2. The image node representation includes extending the finite difference domain by one additional set of nodes with the pressures equal to ones at the other side of the domain boundary (Wang and Anderson, 1995), which translates into no-flow condition $\partial P/\partial x = \partial P/\partial y = 0$ at $x = y = L/2$ for square domains or $\partial P/\partial r = 0$ at $r = r_e$ for circular domains.

The resulting set of ordinary differential equations is solved using the first-order implicit time-stepping method (Wang and Anderson, 1995). Part of this procedure requires that equations (3.20) are linearised. This is achieved by calculating values $|\vec{q}|$ using fluxes from the previous time step, n . For each time step, estimates of $|\vec{q}|$ are improved using Picard iteration until a convergence criterion is satisfied (Stephenson and Radmore, 1990). More details about the linearisation method used are given by Mijic (2009).

Substituting equation (3.20) into equation (3.19) and discretising it in space and time leads to an implicit finite difference approximation for transient 2D Forchheimer flow:

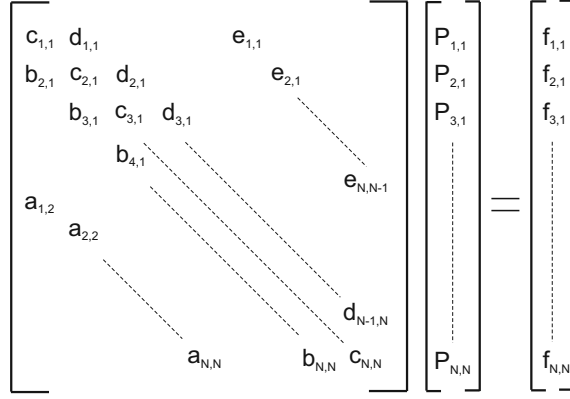


Figure 3.3: Implicit numerical scheme in a matrix form (modified from Mijic (2009)).

3.3 Comparison of solutions

In this study, the level of flow nonlinearity was determined by the dimensionless Forchheimer coefficient group $Qk\rho b/2\pi H\mu r_w$. The pressure behaviour was investigated when the group had values of 0, 1.59 and 3.18, which are representative of typical single-phase liquid systems (Mathias and Todman, 2010). The corresponding values of the Forchheimer coefficient, b , can be obtained from one of the many approximations available in the literature. Mathias and Todman (2010) presented a comparison between laboratory and field-scale Forchheimer coefficients and concluded that in single-phase liquid systems, the approximation of Geertsma (1974):

$$b = 0.005 \phi^{-5.5} k^{-0.5} \quad (3.24)$$

where k is intrinsic permeability (in m^2) and ϕ is porosity, gives an accurate estimation of b (in m^{-1}). This type of correlation is used mostly for formations where flow direction is parallel to the dominant direction of pore channels (Li and Engler, 2001). Figure 3.4 shows values of the Forchheimer coefficient calculated using the relation (3.24).

The numerical scheme was controlled by the maximum number of iterations and the error tolerance. In all the simulations presented, an error tolerance of 0.001 was used with the maximum number of iterations set to 1000.

As a first verification, the numerical model was modified to have a circular no-flow boundary by applying image nodes to all nodes at $x^2 + y^2 = r_e^2$. Figure 3.5 shows dimensionless pressure against dimensionless time at $r = r_w$, for a range of r_e/r_w ratios. Results for circular domains are obtained from equation (3.17) and compared to finite difference

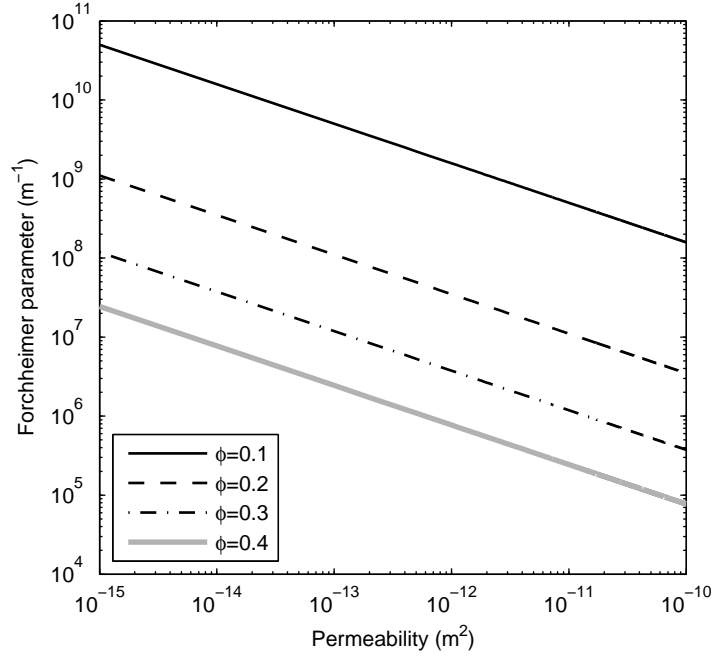


Figure 3.4: Forchheimer coefficient, b obtained from Geertsma (1974) correlation.

simulations. When $b = 0$, it is clear that there is an excellent correspondence between the two models, thereby verifying the numerical solution for Darcy flow in a closed circular unit. There is also an excellent agreement between both solutions for Forchheimer flow, providing times are greater than the minimum of t_0 and t_c .

The proposed model was then tested by simulating the original problem of a closed square domain. For the same scenarios as shown in Figure 3.5, analytical results were obtained using the effective r_e calculated from equation (3.18). In square domains, the increased rate of pressure buildup, which occurs when the pressure perturbation reaches the boundary (i.e. when $t = t_c$), will occur slightly later than in a corresponding circular unit (Figure 3.6 and Table 3.1). Again the agreement between two solutions is excellent, confirming the original hypothesis that square domains are well approximated by circular domains of an equivalent area.

The goodness of fit between analytical and numerical solutions was quantified by calculating the normalised root mean square error (NRMSE) of obtained pressure estimations:

$$NRMSE_p = \frac{1}{P_{n,max} - P_{n,min}} \sqrt{\frac{\sum_{i=1}^n (P_{a,i} - P_{n,i})^2}{n}} \quad (3.25)$$

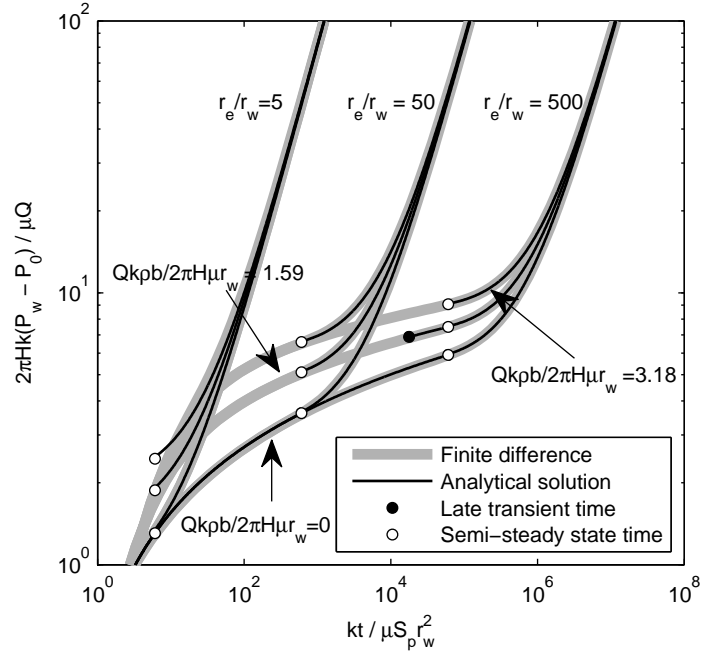


Figure 3.5: Dimensionless well pressure in a circular domain for various values of r_e/r_w and different levels of flow nonlinearity. The analytical solution is that given in equation (3.17), shown only within the time range of validity.

where P_n and P_a are pressures obtained from numerical and analytical models, respectively, and $P_{n,max}$ and $P_{n,min}$ define the range of numerical model values. The results presented in Table 3.1 confirm the excellent agreement between the solutions for both single and multiple well models and all considered levels of flow nonlinearity, having the maximum $NRMSE_p$ equal to 0.18%. Note that in both Figures 3.5 and 3.6, most analytical model results are presented for times $t \geq t_c$. The reason is because when $t_0 \geq t_c$, which is the case for the parameter combinations highlighted in Table 3.1, the closed boundary affects the well pressure before the late transient solution becomes valid. The combined effect of the boundary condition and the Forchheimer flow therefore limits the application of equation (3.17) to the semi-steady state model that is valid when $t \geq t_c$.

3.4 Conclusions

The application of the Forchheimer (1901) equation for the modelling of a single-phase liquid flow so far has been limited to infinite aquifers and single-well systems. In this chapter, the analytical solution for Forchheimer flow to a well in a homogeneous and

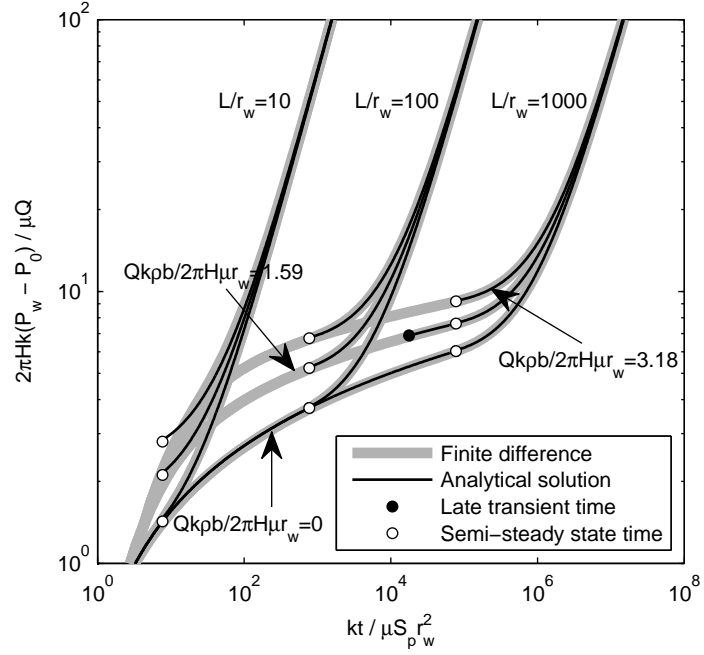


Figure 3.6: Dimensionless well pressure in a square domain for various values of L/r_w and different levels of flow nonlinearity. The analytical solution is that given in equation (3.17) with r_e obtained from equation (3.18), shown only within the time range of validity.

Table 3.1: Dimensionless transition times and error estimates for MWS models comparison.

		Circular domain			Square domain		
		r_e/r_w			L/r_w		
$Qkpb/2\pi H\mu r_w$		(—)			(—)		
	(—)	5	50	500	10	100	1000
$kt_0/\mu D r_w^2$	1.59	1.7723*	1.7723	1.7723	1.7723	1.7723	1.7723
($\cdot 10^4$)	3.18	7.0831	7.0831	7.0831	7.0831	7.0831	7.0831
$kt_c/\mu D r_w^2$	1.59	0.0006	0.0606	6.0575	0.0008	0.0771	7.7126
($\cdot 10^4$)	3.18	0.0006	0.0606	6.0575	0.0008	0.0771	7.7126
$NRMSE_p$	1.59	9.1	9.8	18.2	0.03	0.002	18.9
($\cdot 10^{-2}$ %)	3.18	10.8	10.8	13.5	0.02	0.002	4.2

*highlighted values correspond to the combination of parameters when $t_0 \geq t_c$

confined aquifer was derived (equation (3.17)) and it was shown that the application of the analytical solution is constrained by the time at which the solution becomes valid.

For linear problems, multiple well systems can be analysed using the principle of superposition. Unfortunately, such an approach is not appropriate when a system is under non-Darcy flow conditions. In this chapter, it was hypothesised that a multiple well system can be analysed by finding the pressure buildup at the critical well. That well was treated as a single well in a closed circular formation, with an area equivalent to the zone of influence of the central well in a system of equally spaced multiple wells (Figure 3.1 and equation (3.18)). Comparison with numerical simulations of the full problem, shown in Figure 3.6, verified the accuracy of the approximate solution for all analysed levels of the flow nonlinearity.

The application of the proposed solution is limited to confined aquifers. The problem concerning an unconfined aquifer could potentially be modelled using the confined flow equations if: a) changes in a water table due to injecting are small relative to the fully saturated thickness of the aquifer (10 % or less (Reilly et al., 1984) or b) they are embedded with a delayed yield term (Yeh and Chang, 2012). However, modelling of closed well systems completed in unconfined aquifers requires further research. Moreover, the method was derived for the equally spaced wells. Potentially, this could be corrected by implementing analysis similar to ones for derivation of Dietz shape factors (Dietz, 1953). Finally, the method is limited to homogeneous formations. More accurate estimations of non-Darcy effects in heterogeneous aquifers, taking into account spatial variations of permeability and porosity, could be implemented within the 2D finite difference solution.

The work presented in this chapter sets up a framework for the implementation of the Forchheimer equation in transient analytical and numerical models for single and multiple well systems in closed, confined aquifers. While the numerical model requires significant computational effort, both in terms of grid and iterative convergence, the analytical solution can be applied easily for the determination of the well pressure buildup and multiple well systems analysis. Furthermore, it sets the basis for the analysis of well systems in the presence of hydrological boundaries and points to the possibility of obtaining approximate solutions for alternative non-Darcy problems concerning closed domains and multiple well systems in the same way.

Chapter 4

Immiscible non-Darcy displacement

4.1 Introduction

The fractional flow method was derived for water-oil systems and therefore has been widely applied for analysing oil-recovery processes (Pope, 1980; Orr, 2007). However, if it is applied to gas-liquid systems, such as CO₂ injection in saline aquifers, the problem of non-Darcy effects arises. Low-viscosity gases often have a flow velocity that satisfies the criteria for the initiation of the non-Darcy flow (Dake, 1983). In radial flow, the non-Darcy component is most significant in the region of large pressure gradients close to the well (Mathias et al., 2009a). An analysis of the effects of non-Darcy flow on CO₂ storage will therefore contribute to a better understanding of the processes that can limit CO₂ injectivity.

In radial flow, as the saturation front advances into the reservoir, the influence of the inertial effects lessens and the problem reverts to simulation under Darcy flow conditions. In this case, the fractional flow function should vary with position from the well. In existing solutions, non-Darcy flow conditions are assumed for both flowing phases. However, in a gas-liquid displacement, the injection phase non-Darcy flow is the dominant behaviour, and it can be assumed that the liquid phase flows under Darcy conditions. In this chapter, the non-Darcy flow of the gas phase is modelled by replacing the Darcy's model with a two-phase extension of the Forchheimer equation (Liu et al., 1995; Evans and Evans, 1988). The fractional flow curve is a function of both saturation and the radial distance from the well. The saturation profile is obtained by implementing the generalised method of characteristic (MOC) solution, where the characteristic equation is solved by numerical integration (Lighthill and Whitham, 1955; Greenberg, 1978). In contrast to the Buckley

and Leverett (1942) approach, the characteristic equation is solved with values of fluxes fixed along the curves. The location of the shock front is determined by the equal area rule. The proposed solution is applied to the modelling of CO₂ injection in saline aquifers, with a comparison to the corresponding numerical solution. Furthermore, limitations of the proposed approach with the respect to the full physics of the problem are discussed.

4.2 Spatially varying two-phase flow

In a confined radial two-phase flow system, when effects of hydrodynamic dispersion are neglected, the conservation of mass of the gas phase over the control volume shown in Figure 4.1 has to satisfy the following:

$$\underbrace{[(r + \Delta r)^2 - r^2] \pi H \phi \Delta(S_1 \rho_1)}_{\text{Change in storage}} = \underbrace{2r\pi H \Delta t \rho_1 q_1}_{\text{Mass in}} - \underbrace{2(r + \Delta r)\pi H \Delta t [\rho_1 q_1 + \Delta(\rho_1 q_1)]}_{\text{Mass out}} \quad (4.1)$$

where S is the phase saturation, r is radial distance from the well, H is aquifer thickness, ϕ is formation porosity, ρ is fluid density, q is fluid flux and t is time since the beginning of injection. Subscripts define the phases considered. The subscript 1 denotes injected gas and subscript 2 will be used for the resident liquid. Equation (4.1) assumes that there is no segregation due to gravity, that is a flux is constant along the entire saturated thickness of the aquifer.

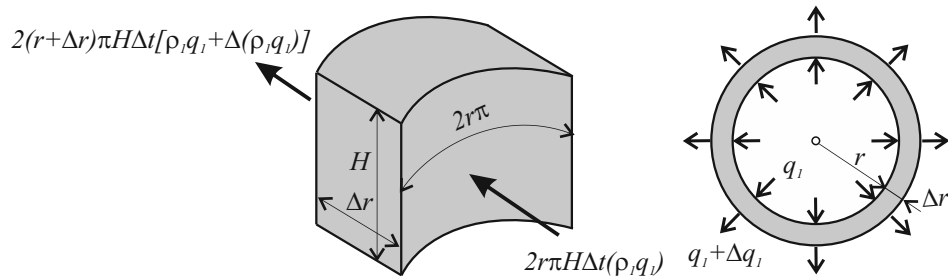


Figure 4.1: Control volume in a radial two-phase flow system.

Rearranging equation (4.1) and assuming infinitesimal Δr and Δt gives:

$$\phi \frac{\partial(S_1 \rho_1)}{\partial t} = -\frac{\rho_1 q_1}{r} - \frac{\partial(\rho_1 q_1)}{\partial r} \quad (4.2)$$

If the gas is assumed to be incompressible ($\rho_1=\text{const.}$), the conservation equation for the gas phase becomes:

$$\frac{\partial S_1}{\partial t} + \frac{1}{\phi} \left[\frac{q_1}{r} + \frac{\partial q_1}{\partial r} \right] = 0 \quad (4.3)$$

The same conservation equation can be written for the liquid phase:

$$\frac{\partial S_2}{\partial t} + \frac{1}{\phi} \left[\frac{q_2}{r} + \frac{\partial q_2}{\partial r} \right] = 0 \quad (4.4)$$

Adding equations (4.3) and (4.4) gives:

$$\frac{\partial(S_1 + S_2)}{\partial t} + \frac{1}{\phi} \left[\frac{1}{r}(q_1 + q_2) + \frac{\partial(q_1 + q_2)}{\partial r} \right] = 0 \quad (4.5)$$

The sum of phase saturations has to be 1 and is therefore constant. Consequently, the time derivative in equation (4.5) is equal to zero. In addition, the total fluid flux can be defined as a sum of phase velocities, $q = q_1 + q_2$. Therefore, the change of the total flow velocity in radial direction is:

$$\frac{\partial q}{\partial r} = -\frac{q}{r} \quad (4.6)$$

Using the concept of the fractional flow, where $f_1 = q_1/q$, equation (4.3) can be written as:

$$\frac{\partial S_1}{\partial t} + \frac{1}{\phi} \left[\frac{f_1 q}{r} + \frac{\partial}{\partial r}(f_1 q) \right] = 0 \quad (4.7)$$

Substituting equation (4.6) into equation (4.7) and applying the product rule for the derivative of a product of functions $f_1 = f_1(r)$ and $q = q(r)$ gives:

$$\frac{\partial S_1}{\partial t} + \frac{q}{\phi} \frac{\partial f_1}{\partial r} = 0 \quad (4.8)$$

The total fluid flux in equation (4.8) can be expressed as a function of volumetric injection flow rate as $q = Q/A$, where the cross-sectional area is $A = 2r\pi H$. Finally, the radial conservation equation for the gas phase in a two-phase incompressible system is obtained

as:

$$\frac{\partial S_1}{\partial t} + \frac{Q}{\pi H \phi} \frac{\partial f_1}{\partial(r^2)} = 0 \quad (4.9)$$

Equation (4.9) is analogous to the Buckley and Leverett (1942) formulation for linear flow:

$$\frac{\partial S_1}{\partial t} + \frac{Q}{A \phi} \frac{\partial f_1}{\partial x} = 0 \quad (4.10)$$

with two differences: 1) equation (4.9) is developed for a radial flow geometry, whereas equation (4.10) assumes a linear one-dimensional reservoir, and 2) in equation (4.10), the fractional flow is uniform, that is the fluid flux does not change along the flow direction; in equation (4.9) fractional flow can vary with the radial distance from the well. The latter difference permits the application of equation (4.9) in analysis of the two-phase flow under spatially varying conditions.

To solve equation (4.9), it is necessary to define the functional dependance of the gas fractional flow, that is the relation $f_1 = f_1(S_1, r)$. In this study, it is assumed that the gas phase flows under non-Darcy conditions and the two-phase extension of the Forchheimer equation (Liu et al., 1995; Evans and Evans, 1988) is valid:

$$-\frac{dP}{dr} = \frac{\mu_1}{k k_{r1}} q_1 + b_1 \rho_1 q_1 |q_1| \quad (4.11)$$

where k_r is the relative permeability. The liquid phase flows under Darcy conditions and the two-phase extension of the Darcy's law can be applied (Dake, 1983):

$$q_2 = -\frac{k k_{r2}}{\mu_2} \frac{dP}{dr} \quad (4.12)$$

The linear behaviour of the liquid phase enables direct calculation of the flux q_2 and its implementation into the fractional flow function. However, the governing partial differential equation for the gas phase is nonlinear with respect to q_1 . To obtain the value of the gas phase flux, some form of linearisation of equation (4.11) with respect to the non-Darcy term is needed.

4.2.1 Non-Darcy gas phase velocity

In this study, equation (4.11) is linearised by rearranging it such that:

$$q_1 = -\frac{kk_{r1}}{\mu_1} \frac{dP}{dr} \left(1 + \frac{b_1 \rho_1 kk_{r1}}{\mu_1} |q_1| \right)^{-1} \quad (4.13)$$

The following terms are defined:

$$B_1 = \frac{b_1 \rho_1 kk_{r1}}{\mu_1} \quad (4.14)$$

and

$$q_1^0 = -\frac{kk_{r1}}{\mu_1} \frac{dP}{dr} \quad (4.15)$$

Equation (4.14) defines a Forchheimer flow parameter, B_1 . As the gas is assumed to be incompressible and the phase density does not depend on the pressure, the parameter B_1 is a function of gas saturation only ($B_1 = B_1(S_1)$). This assumption may have a significant impact on pressure changes in the near-well region, which will be discussed in more detail in Chapter 6. Values of B_1 are determined by the level of non-Darcy effects defined by the Forchheimer coefficient for the gas phase, b_1 . Correlations used in this study to estimate values of b_1 are discussed in more detail below. Equation (4.15) defines the Darcy fraction of the gas flux, q_1^0 . Finally, equation (4.13) transforms into:

$$q_1 = \frac{q_1^0}{1 + B_1 |q_1|} \quad (4.16)$$

which leads to the specification of the Forchheimer factor, β defined as:

$$\beta = 1 + B_1 |q_1| \quad (4.17)$$

Forchheimer factor is treated as a coefficient and it is assumed to be a scalar function of the magnitude of the gas phase velocity at any point. Since the value of the gas flux exists on both sides of equation (4.16), the solution for q_1 must be obtained iteratively.

Iterative algorithm for non-Darcy gas flux

In this study, the following algorithm for the calculation of the non-Darcy gas flux is suggested (Figure 4.2):

1. Initial pressure gradients in the two-phase region, $(dP/dr)^i$ are obtained from the mass conservation equation (Wu, 2001):

$$Q = (q_1 + q_2)2r\pi H \quad (4.18)$$

assuming Darcy flow conditions for both flowing phases (i.e. $B_1 = 0$). The rearrangement of equation (4.18) and substitution of expressions for flow fluxes (4.12) and (4.16) leads to:

$$\left(\frac{dP}{dr}\right)^i = -\frac{Q}{2r\pi Hk} \left(\frac{k_{r1}}{\mu_1} + \frac{k_{r2}}{\mu_2}\right)^{-1} \quad (4.19)$$

2. Values of $(dP/dr)^i$ are substituted into equation (4.15), to obtain the Darcy fraction of the gas phase velocity:

$$q_1^0 = -\frac{kk_{r1}}{\mu_1} \left(\frac{dP}{dr}\right)^i \quad (4.20)$$

3. Equation (4.16) is rearranged into the form of a quadratic equation $B_1 q_1^2 + q_1 - q_1^0 = 0$, whose positive solution is the gas flux under non-Darcy flow conditions:

$$q_1 = \frac{-1 + \sqrt{1 + 4B_1 q_1^0}}{2B_1} \quad (4.21)$$

4. Using the gas flux q_1 from the previous step, the value of factor β is obtained from equation (4.17).
5. The pressure gradients in the next iteration, $(dP/dr)^{i+1}$ are calculated under the assumption of non-Darcy flow conditions that correspond to the level of inertial effects defined with the value of β , such that:

$$\left(\frac{dP}{dr}\right)^{i+1} = -\frac{Q}{2r\pi Hk} \left(\frac{1}{\beta} \frac{k_{r1}}{\mu_1} + \frac{k_{r2}}{\mu_2}\right)^{-1} \quad (4.22)$$

6. Values of $(dP/dr)^{i+1}$ and $(dP/dr)^i$ are compared. If the difference is larger than the defined tolerance error, the procedure is repeated with pressure gradients updated from the previous iteration, until the convergence criterion is satisfied.

The procedure is referred to as the Picard iterative method (Stephenson and Radmore, 1990). Among many other applications, the method was successfully implemented by Mijic (2009) for the linearisation of the governing continuity equation in a numerical solution for two-dimensional non-Darcy single-phase flow.

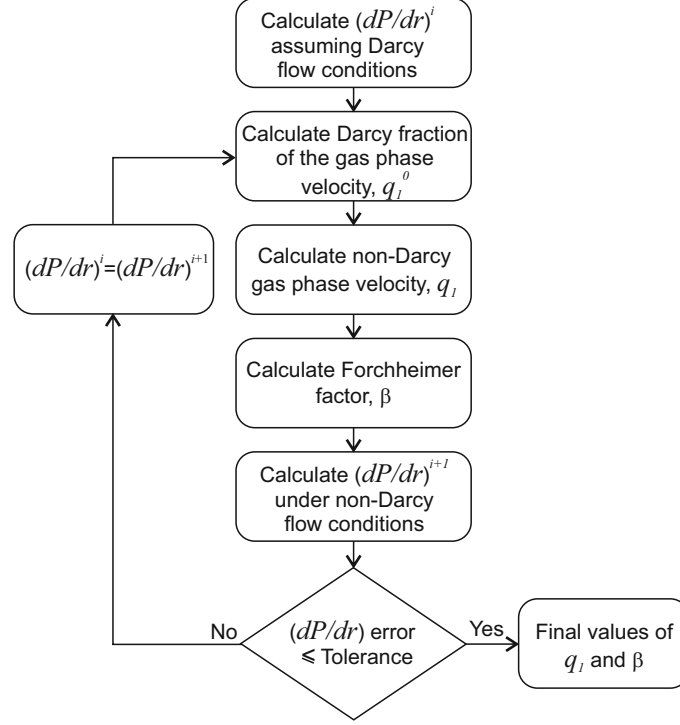


Figure 4.2: Iterative procedure for the calculation of the non-Darcy gas flux.

4.2.2 Non-Darcy fractional flow function

In equation (4.9), the fractional flow function is defined as:

$$f_1 = \frac{q_1}{q} = \frac{q_1}{q_1 + q_2} \quad (4.23)$$

After the gas phase velocity has been obtained, and hence the value of the factor β , the fractional flow function can be determined under non-Darcy flow conditions. Substitution of equations (4.12), (4.16) and (4.17) into equation (4.23) leads to:

$$f_1 = \left(1 + \frac{k_{r2}\mu_1}{k_{r1}\mu_2} \beta \right)^{-1} \quad (4.24)$$

Equation (4.24) is the final expression for the spatially varying fractional flow function. The advantage of this approach is that when inertial effects are insignificant, the value of B_1 tends to zero and hence the factor β converges to 1. Consequently, the problem simplifies to Darcy flow conditions and equation (4.24) reverts to the well-known Buckley and Leverett (1942) fractional flow approximation.

4.2.3 Solution for saturation by the MOC

In order to reduce the number of variables, the following dimensionless transformations in space and time, respectively, can be applied (Rossen et al., 2011):

$$r_D = \frac{r^2}{r_e^2} \quad (4.25)$$

$$t_D = \frac{Qt}{\pi r_e^2 H \phi} \quad (4.26)$$

Substitution of equations (4.25) and (4.26) simplifies the governing differential equation (4.9) to:

$$\frac{\partial S_1}{\partial t_D} + \frac{\partial f_1}{\partial r_D} = 0 \quad (4.27)$$

Introduction of the fractional flow dependency on both saturation and radial distance from the well leads to the nonclassical form of a hyperbolic problem. If f_1 depends on both S_1 and r_D then the governing differential equation (4.27) becomes (Rossen et al., 2011):

$$\frac{\partial S_1}{\partial t_D} + \left(\frac{\partial f_1}{\partial S_1} \right)_{r_D} \frac{\partial S_1}{\partial r_D} = - \left(\frac{\partial f_1}{\partial r_D} \right)_{S_1} \quad (4.28)$$

Because S_1 is a function of r_D and t_D , the expression for the total derivative of S_1 can be written as (Orr, 2007):

$$\frac{dS_1}{d\eta} = \frac{\partial S_1}{\partial t_D} \frac{dt_D}{d\eta} + \frac{\partial S_1}{\partial r_D} \frac{dr_D}{d\eta} \quad (4.29)$$

where η is a differential parameter. Term by term comparison of equation (4.28) with equation (4.29) gives:

$$\frac{dS_1}{d\eta} = - \left(\frac{\partial f_1}{\partial r_D} \right)_{S_1} \quad (4.30)$$

$$\frac{dt_D}{d\eta} = 1 \quad (4.31)$$

$$\frac{dr_D}{d\eta} = \left(\frac{\partial f_1}{\partial S_1} \right)_{r_D} \quad (4.32)$$

Equations (4.30)–(4.32) are known as the characteristic equations and $t_D(\eta)$ and $r_D(\eta)$ are characteristic curves along which the derivative of S_1 is $dS_1/d\eta$.

Under Darcy flow conditions, when $f_1 = f_1(S_1)$, the derivative of S_1 with respect to η is zero, and hence characteristic curves are straight lines along which S_1 is constant (Orr, 2007). Moreover, the velocity at which the saturation propagates along a characteristic is constant for a given value of S_1 . Equation (4.30) indicates that under non-Darcy flow conditions, S_1 varies along a characteristic. Parameter η can be eliminated from equations (4.31) and (4.32), which gives:

$$v = \frac{dr_D}{dt_D} = \left(\frac{\partial f_1}{\partial S_1} \right)_{r_D} \quad (4.33)$$

Equation (4.33) shows that the saturation wave in non-Darcy displacement has a nonuniform wave velocity, v that changes along the flow direction. Hence, the characteristic curves are no longer straight.

Combining equations (4.27) and (4.33) gives:

$$\frac{\partial f_1}{\partial t_D} + v \frac{\partial f_1}{\partial r_D} = 0 \quad (4.34)$$

This means that f_1 is constant on waves travelling past the point with velocity v (Lighthill and Whitham, 1955). Mathematically, equation (4.34) has a new system of characteristics, given by equation (4.33), along which the fractional flow f_1 is constant. The wave velocity is therefore the slope of the flow-saturation curve for a fixed r_D . If v is expressed as a function of f_1 and r_D , and the initial condition is defined as:

$$r_D(f_1, 0) = r_{wD} \quad (4.35)$$

then the path of the wave carrying a given fractional flow f_1 can be obtained as:

$$r_D = \int_0^{t_D} v(f_1, r_D) dt_D + r_{wD} = \int_0^{t_D} \left(\frac{\partial f_1}{\partial S_1} \right)_{r_D} dt_D + r_{wD} \quad (4.36)$$

The resulting solution is a multivalued saturation profile at a fixed time. In order to remove the multivalued parts, the discontinuity or the leading shock has to be inserted. The general approach to determining the discontinuity in the saturation profile is by implementing the equal area rule, which ensures that the total mass of the shock solution matches that of the triple-valued solution, as required by the physical conservation law. For linear flow problems, the equal area rule simplifies to the application of the Welge (1952) method, where the leading shock is a tangent to the fractional flow curve. The shock front advances with a constant speed, which is determined by the Rankine-Hugoniot condition.

Under non-Darcy flow conditions, however, this approach is not applicable. In non-Darcy two-phase flow systems, the characteristic wave velocity varies with distance from the well. Consequently, both the shock front saturation and speed will change in the radial direction. However, the location of the leading shock, r_{LD} at a fixed time can be obtained by integrating the saturation profile using the equal area rule. Equating areas A_1 and A_2 , shown in Figure 4.3, gives:

$$r_{LD} = \frac{1}{S_{1L}} \int_{S_{1c}}^{S_{1L}} r_D dS_1 \quad (4.37)$$

where S_{1L} is a leading shock front saturation under non-Darcy flow conditions and S_{1c} is a critical gas saturation, below which the gas phase becomes immobile. Details of the implementation of the equal area rule for determining the shock front position in non-Darcy displacement are given in Appendix C. LeVeque (1992) proved that the Rankine-Hugoniot condition holds even when the discontinuity propagates with a variable speed, as is the case in the two-phase non-Darcy flow. The instantaneous shock velocity at time t can be calculated with values of saturations at both sides of the shock evaluated at the same time.

4.2.4 Solving for pressure

Once the saturation profile is known, the solution for pressure can be obtained from the expression for pressure gradients under non-Darcy flow conditions given in equation (4.22), which after implementing the dimensionless transformation (4.25) becomes:

$$\frac{dP}{dr_D} = -\frac{Q}{4r_D\pi Hk} \left(\frac{1}{\beta} \frac{k_{r1}}{\mu_1} + \frac{k_{r2}}{\mu_2} \right)^{-1} \quad (4.38)$$

Given the knowledge of the shock front location, r_{LD} and assuming that the end point

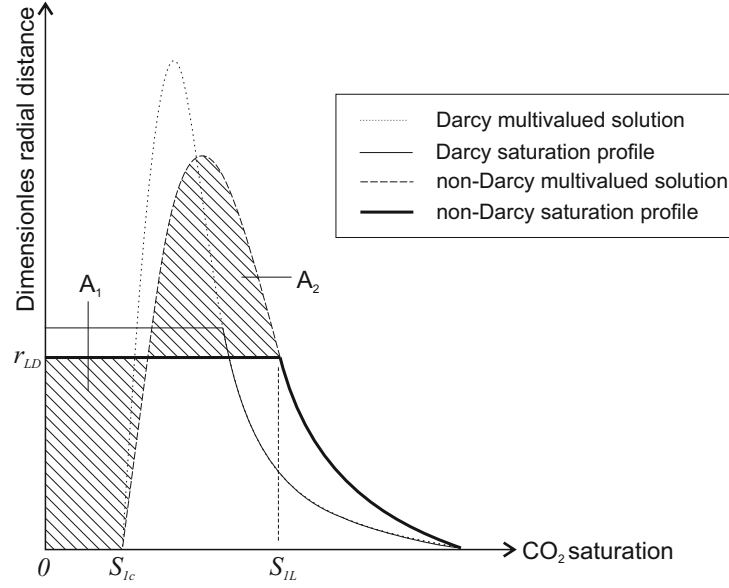


Figure 4.3: Equal area rule for immiscible non-Darcy displacement.

relative permeability of the liquid phase is equal to 1, equation (4.38) can be modified into:

$$\frac{dP}{dr_D} = -\frac{Q}{4\pi Hk} \begin{cases} \frac{1}{r_D} \left(\frac{1}{\beta} \frac{k_{r1}}{\mu_1} + \frac{k_{r2}}{\mu_2} \right)^{-1}, & r_{wD} \leq r_D \leq r_{LD} \\ \frac{\mu_2}{r_D}, & r_D > r_{LD} \end{cases} \quad (4.39)$$

and integrated with respect to r_D , which gives:

$$P - P_0 = \frac{Q}{4\pi Hk} \begin{cases} \mu_1 G_p(r_D) + \mu_2 G_b(r_D), & r_{wD} \leq r_D \leq r_{LD} \\ \mu_2 G_b(r_D), & r_D > r_{LD} \end{cases} \quad (4.40)$$

where P_0 is the initial reservoir pressure and G_p and G_b are pressure integrals for two-phase and brine regions, respectively.

The pressure integral for the two-phase region:

$$G_p(r_D) = -\frac{1}{\mu_1} \int_{r_D}^{r_D^L} \frac{1}{r_D} \left(\frac{1}{\beta} \frac{k_{r1}}{\mu_1} + \frac{k_{r2}}{\mu_2} \right)^{-1} dr_D \quad (4.41)$$

can be solved explicitly if relative permeability functions are linear (Mathias et al., 2009a). In this study, it is assumed that the relative permeability varies nonlinearly with saturation and the integral in equation (4.41) is evaluated by the numerical integration. Note that values of pressure for the non-Darcy flow are influenced by the value of β .

Solution for the brine domain depends on the boundary condition and time since the

beginning of injection. Before the pressure perturbation has reached the boundary (i.e. when $t_D < t_{cD}$, where t_{cD} is the critical time that shall be defined below), the transient solution for the single-phase liquid flow under Darcy conditions is given by Theis (1935):

$$P - P_0 = \frac{Q\mu}{4\pi Hk} E\left(\frac{\mu cr^2}{4kt}\right) \quad (4.42)$$

where E denotes the exponential integral function. When $t_D \geq t_{cD}$, the pressure is determined by the influence of the boundary. The pressure integral for the brine region, $G_b(r_D)$ therefore has to be determined based on the outer boundary condition.

Pressure integral for open aquifers

In open aquifers, the constant pressure far-field boundary condition is implemented through the Thiem (1906) equation:

$$P - P_0 = \frac{Q\mu}{2\pi Hk} \ln\left(\frac{r_e}{r}\right) \quad (4.43)$$

By applying dimensionless transformations (4.25) and (4.26), equations (4.42) and (4.43) can be simplified and substituted into system (4.40). The pressure integral for open formations becomes:

$$G_b(r_D) = \begin{cases} E(\alpha r_D), & t_D < t_{cD} \\ \ln\left(\frac{1}{r_D}\right), & t_D \geq t_{cD} \end{cases} \quad (4.44)$$

where

$$\alpha = \frac{Q\mu_2 c_2}{4\pi Hk t_D} \quad (4.45)$$

The transition time, t_{cD} can be obtained by equating solutions before and after the pressure is influenced by the boundary conditions, which gives:

$$t_{cD} = \frac{Q\mu_2 c_2}{4\pi Hk} \exp(0.5772) \quad (4.46)$$

where c_2 is brine compressibility.

Pressure integral for closed aquifers

The solution for pressure at the well in closed formations can be obtained from equation (3.12), assuming that brine flows under Darcy conditions (i.e. $b = 0$). To incorporate this expression within the two-phase solution it is necessary to set r_w as the outside edge of the two-phase region defined by the leading shock front position, r_L (Mathias et al., 2011b):

$$P_L - P_0 = \frac{Qt}{\pi r_e^2 H \phi c_2} + \frac{Q\mu_2}{2\pi k H} \left[\ln \left(\frac{r_e}{r_L} \right) - \frac{3}{4} \right] \quad (4.47)$$

The pressure distribution in the brine region can be obtained from equation (3.8), which after setting $P_w = P_L$ and neglecting non-Darcy flow becomes:

$$P - P_L = \frac{Q\mu_2}{2\pi k H r_e^2} \left[\frac{r^2 - r_L^2}{2} - r_e^2 \ln \left(\frac{r}{r_L} \right) \right] \quad (4.48)$$

Combining equations (4.47) and (4.48) gives the final expression for the pressure distribution within brine region in two-phase displacement:

$$P - P_0 = \frac{Qt}{\pi r_e^2 H \phi c_2} + \frac{Q\mu_2}{2\pi k H} \left[\ln \left(\frac{r_e}{r} \right) - \frac{3}{4} + \frac{r^2 - r_L^2}{2r_e^2} \right] \quad (4.49)$$

This modification was unnecessary when deriving the pressure integral for open aquifers because the solution is not influenced by the formation boundary.

After dimensionless transformations using equations (4.25) and (4.26), the expression for the pressure integral in closed formations takes the form:

$$G_b(r_D) = \begin{cases} E(\alpha r_D), & t_D < t_{cD} \\ \frac{1}{\alpha} + \ln \left(\frac{1}{r_D} \right) - \frac{3}{2} + \frac{r_D - r_{LD}}{2}, & t_D \geq t_{cD} \end{cases} \quad (4.50)$$

where the critical time is defined as:

$$t_{cD} = \frac{Q\mu_2 c_2}{4\pi H k} \exp(0.5772 - \frac{3}{2}) \approx 0.2423 \frac{Q\mu_2 c_2}{\pi H k} \quad (4.51)$$

Note that the expression for t_{cD} in closed formations coincides with the solution given in equation (3.13).

4.3 Model development

The proposed algorithm for modelling of two-phase non-Darcy flow, together with the corresponding modules for the solution under Darcy flow conditions, is shown in Figure 4.4. The new model described here has been implemented for the analysis of CO₂ injection in saline aquifers. The model application requires estimates of CO₂ and brine properties, relative permeabilities and the Forchheimer flow coefficient for the gas phase. These are discussed in more detail below.

4.3.1 Estimation of fluid properties

Estimates of density and viscosity for both CO₂ (subscript 1) and brine (subscript 2) can be obtained using empirical correlations with temperature, pressure and salinity. The CO₂ density was obtained from the approximation given by Spycher et al. (2003), using the Redlich and Kwong (1949) equation formulated as:

$$P = \left(\frac{RT}{V - d_c} \right) - \left(\frac{a_c}{T^{0.5}V(V + d_c)} \right) \quad (4.52)$$

where a_c and d_c are parameters accounting for intermolecular attraction and repulsion, respectively, V is the molar volume of gas at a given pressure P (in bar) and temperature T (in Kelvins). The universal gas constant is equal to $R = 88.1447 \text{ bar cm}^3 \text{ mol}^{-1} \text{ K}^{-1}$. The value of intermolecular attraction in equation (4.52) can be obtained from:

$$a_c = 7.54 \cdot 10^7 - 4.13 \cdot 10^4 T \quad (4.53)$$

where T is temperature in Kelvins. Intermolecular repulsion is a constant and equal to $d_c = 27.8 \text{ cm}^3 \text{ mol}^{-1}$.

To compute the molar volume of the compressed gas phase Spycher et al. (2003) suggested rearrangement of equation (4.52) in a general cubic equation in terms of V and then solving it using the method of Nickalls (1993). In the present study, however, the molar volume for a given pressure was found in three steps:

1. Pressures for the chosen temperature and possible range of molar volumes (in this study, V is assumed to be between $30 - 10^3 \text{ cm}^3 \text{ mol}^{-1}$) were calculated using equation (4.52).

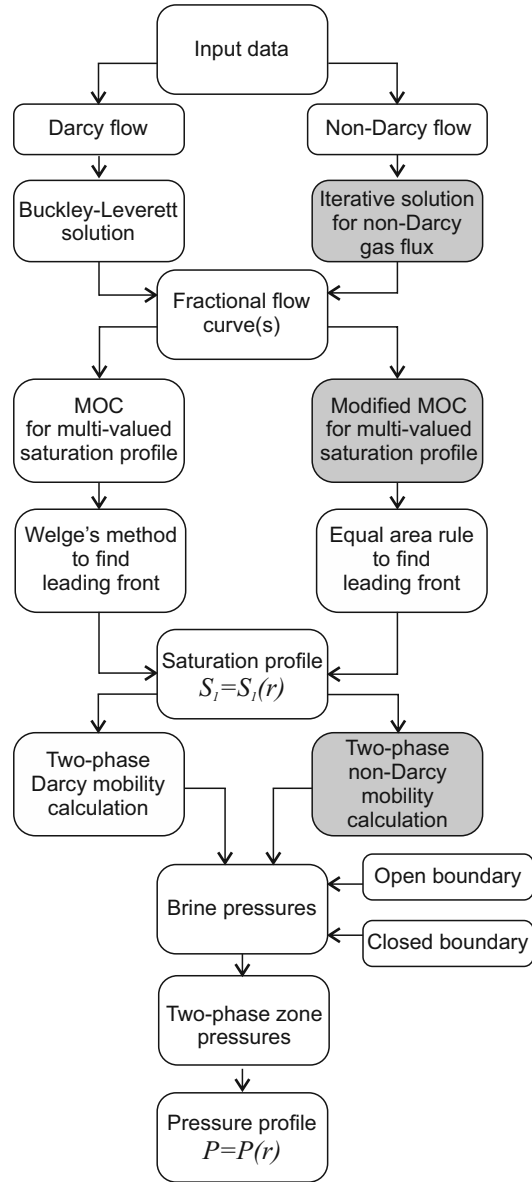


Figure 4.4: Solution algorithm for the two-phase Darcy and non-Darcy immiscible displacements. Modules that implement novel approaches to the solution of the non-Darcy problem are highlighted in grey.

2. A curve was fitted to the pressure data within the range corresponding to the molar volumes used in the pervious step ($P \approx 0.5 - 1000$ MPa). In this study, a MATLAB piecewise cubic Hermite polynomial was used for interpolation within vectors P and V (solid line in Figure 4.5).
3. The molar volume corresponding to a particular pressure and temperature was found from the obtained $P - V - T$ function. Circular markers in Figure 4.5 show that fitted values within a range of pressures considered in this study ($P = 10 - 60$ MPa) are in excellent agreement with the values obtained directly from the Redlich and Kwong (1949) correlation.

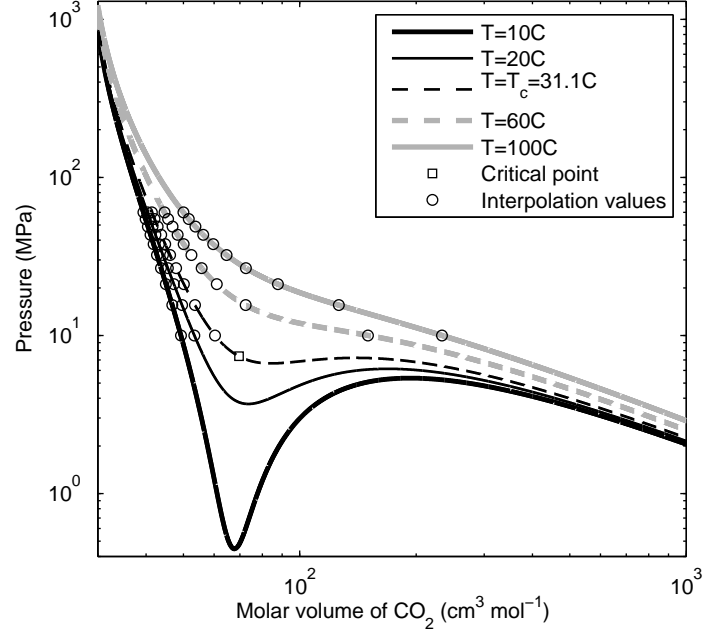


Figure 4.5: $P - V - T$ relationship calculated using the Redlich and Kwong (1949) equation of state (4.52) (solid line) and Hermite polynomial interpolation algorithm (circular markers).

Once the molar volume was calculated, CO_2 density, ρ_1 (in kg m^{-3}) was obtained from:

$$\rho_1 = \frac{1000M_c}{V} \quad (4.54)$$

where $M_c=44.01 \text{ g mol}^{-1}$ is the molar mass of CO_2 .

The CO₂ viscosity was calculated using the Mathias et al. (2009b) approximation of the Fenghour et al. (1998) relationship:

$$\mu_1 = 16.485 + (0.009487\rho_1)^2 - (0.0025939\rho_1)^4 + (0.0019815\rho_1)^6 \quad (4.55)$$

where μ is in $\mu\text{Pa s}$ and ρ is in kg m^{-3} . Mathias et al. (2009b) showed that equation (4.55) gives a good approximation over the temperature range $10^\circ\text{C} \leq T \leq 100^\circ\text{C}$. Both CO₂ density and viscosity vary significantly within the range of pressures chosen for the investigation (Figure 4.6), especially as the conditions are approaching critical point of CO₂, challenging the assumption of the fluid incompressibility made earlier in section 4.2. The correction of the analytical solution to account for the CO₂ compressibility will be discussed in more detail in Chapter 6.

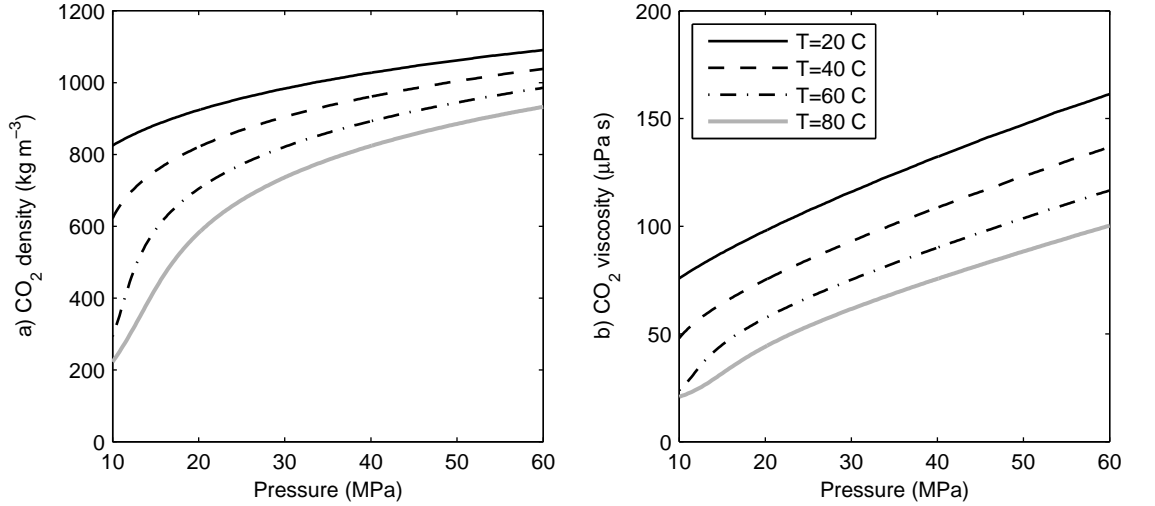


Figure 4.6: CO₂ properties: a) density and b) viscosity as a function of pressure and temperature. Both properties vary significantly within the chosen range of pressures.

In this study, brine density was obtained from the correlation given by Batzle and Wang (1992). This algorithm has been shown to be the most accurate for analysis of CO₂ injection problems in sedimentary basins for pressures up to 100 MPa, temperatures below 350°C and brine salinity less than 0.32 g cm^{-3} (Adams and Bachu, 2002). The Batzle and Wang (1992) correlation for brine density, ρ_2 (in g cm^{-3}) as a function of water density, ρ (in g cm^{-3}) is:

$$\rho_2 = \rho + K_s \{0.668 + 0.44K_s + 10^{-6}[300P - 2400PK_s + T(80 + 3T - 3300K_s - 13P + 47PK_s)]\} \quad (4.56)$$

where:

$$\rho = 1 + 10^{-6}(-80T - 3.3T^2 + 0.00175T^3 + 489P - 2TP + 0.016T^2P - 1.3 \cdot 10^{-5}T^3P - 0.333P^2 - 0.002TP^2) \quad (4.57)$$

and T is temperature (in °C), P is pressure (in MPa) and K_s is salt concentration (in kg dm⁻³).

The Kestin et al. (1981) relationship, as approximated by Batzle and Wang (1992) for temperatures below 250 °C, was used for calculation of brine viscosity (in mPa s):

$$\mu_2 = 0.1 + 0.333K_s + (1.65 + 91.3K_s^3) \exp \{-[0.42(K_s^{0.8} - 0.17)^2 + 0.045]T^{0.8}\} \quad (4.58)$$

Brine compressibility, c_2 was obtained by differentiating equations (4.56) and (4.57) with respect to P , giving (Mathias et al., 2009b):

$$\frac{d\rho_2}{dP} = \frac{d\rho}{dP} + K_s 10^{-6}[300 - 2400K_s + T(-13 + 47K_s)] \quad (4.59)$$

$$\frac{d\rho}{dP} = 10^{-6}(489 - 2T + 0.016T^2 - 1.3 \cdot 10^{-5}T^3 - 0.666P - 0.004TP) \quad (4.60)$$

and then substituting the result into the expression given by Bear (1979):

$$c_2 = \frac{1}{\rho_2} \frac{d\rho_2}{dP} \quad (4.61)$$

Figure 4.7 summarises the variation of brine properties with temperature, pressure and salinity, for conditions representative of the sedimentary basins. The conditions investigated here cover temperatures between 10 and 100 °C, pressures up to 60 MPa and brine salinity up to 0.3 g cm⁻³ (Bachu and Adams, 2003). Brine density is almost independent of pressure and temperature, but increases with salinity. The viscosity and compressibility of brine are strongly dependent on both temperature and salinity.

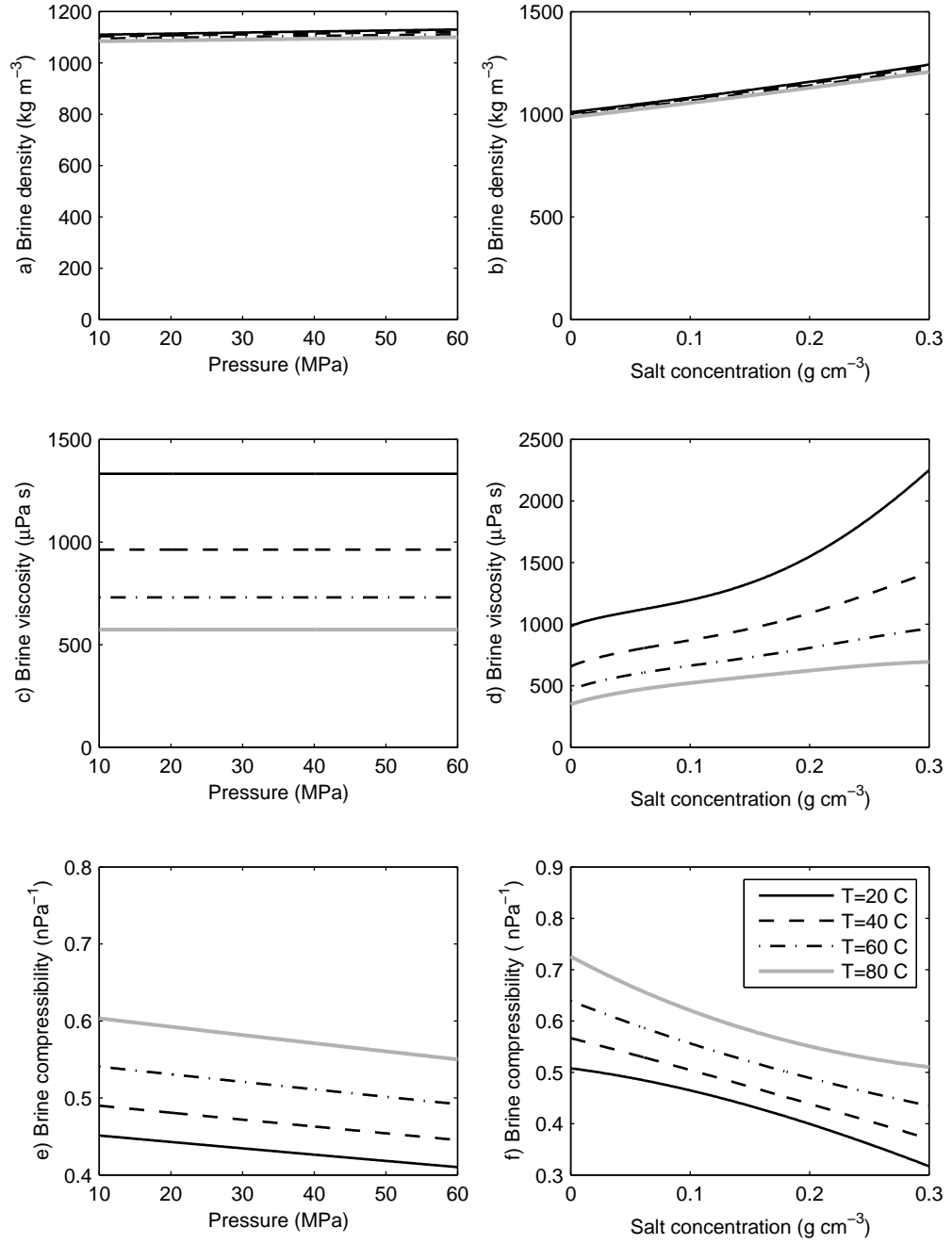


Figure 4.7: Variation of brine properties: a), c) and e) with pressure for $K_s=0.15 \text{ g cm}^{-3}$ and b), d) and f) with salinity for $P=30 \text{ MPa}$. Brine density increases with salinity, while viscosity and compressibility of brine are both dependent on pressure and salt concentration.

4.3.2 Relative permeability functions

Assuming that the gas phase relative permeability is a nonlinear function of saturation, its value can be obtained from the model presented by Corey (1954):

$$k_{r1} = (1 - \hat{S})^n [1 - (\hat{S})^n] \quad (4.62)$$

where

$$\hat{S} = \frac{S_2 - S_{2r}}{1 - S_{2r} - S_{1c}} \quad (4.63)$$

In the original work of Corey (1954), the parameter n was chosen to be 2 and subscripts r and c represent the residual saturation of the liquid phase and the critical saturation of the gas phase, respectively.

The relative permeability of the liquid phase can be found using the parametric model for predicting the hydraulic conductivity of two-phase flow given by Luckner et al. (1989). The model is an extension of the approach suggested by van Genuchten (1980) for the estimation of the hydraulic conductivity of single-phase flow systems. If the scaled variable is defined as:

$$\bar{S} = \frac{S_2 - S_{2r}}{1 - S_{2r}} \quad (4.64)$$

then the relative permeability of the liquid phase is:

$$k_{r2} = (\bar{S})^l \left\{ \left[1 - (1 - \bar{S})^{1/g} \right]^g \right\}^2 \quad (4.65)$$

where l is a pore connectivity for the liquid phase and g is the van Genuchten model parameter. While the value of l is fixed ($l = 0.5$), the value of the van Genuchten parameter can vary within the range $0 \leq g \leq 1$.

In addition to Corey (1954) and van Genuchten (1980) relations, two-phase relative permeability can be calculated as a function of the end-point relative permeability. In such a case, models (4.62) and (4.65) are rearranged to take the form of power-laws:

$$k_{r1} = k_{r10} \left(\frac{S_1 - S_{1c}}{1 - S_{2r} - S_{1c}} \right)^n \quad (4.66)$$

$$k_{r2} = k_{r20} \left(\frac{1 - S_1 - S_{2r}}{1 - S_{2r} - S_{1c}} \right)^g \quad (4.67)$$

where k_{r10} and k_{r20} are the end-point relative permeabilities of the gas and liquid phase, respectively. Finally, CO₂-brine system relative permeability can be estimated using the Brooks-Corey model (Krevor et al., 2012):

$$k_{r1} = k_{r10}(1 - \bar{S})^2[1 - (\bar{S})^n] \quad (4.68)$$

$$k_{r2} = k_{r20}(\bar{S})^g \quad (4.69)$$

To test the applicability of the aforementioned correlations to CO₂-brine systems, model results were compared with experimental data. Bennion and Bachu (2005) presented detailed water-CO₂ relative permeability data set for a variety of potential sequestration formations in Western Canada. They suggested that a low end-point saturation and relative permeability are intrinsic to the CO₂-brine system and controlled by interfacial tension. In their experiments, however, Krevor et al. (2012) showed that the maximum observed saturations are controlled by the maximum capillary pressure possible in a given experimental setup. Hence, low end-point CO₂ saturation and permeability should not be taken as end-point values of the $S_1 - k_r$ function, unless capillary pressures achieved during the experiment are representative of the aquifer and storage scheme being analysed.

The predictions of the various models for Berea sandstone are compared with the experimental data in Figure 4.8. Allowing for the variation of both n and g parameter values and taking into account the influence of the end-point relative permeability of both phases, power-law models show excellent agreement with the experimental data. A summary of experimental data, together with optimised values of parameters in equations (4.66) and (4.67) are given in Table 4.1 and shown in Figure 4.9.

4.3.3 Forchheimer coefficient for the mobile gas phase

In the literature, there are very limited data available for quantifying the effect of the mobile liquid saturation on the non-Darcy factor in gas-liquid systems. Results of experiments carried out so far, however, show that the gas phase non-Darcy coefficient increases significantly with increasing liquid saturation.

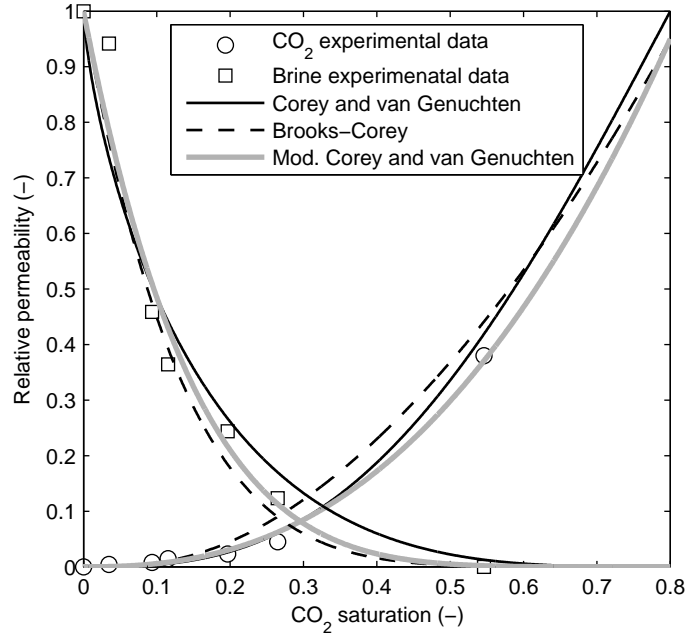


Figure 4.8: Relative permeability experimental data for Berea sandstone (Krevor et al., 2012) and correlation model estimations.

Table 4.1: Summary of experimental data (k_{r10} , k_{r20} , S_{1c} and S_{2r}) from Krevor et al. (2012) and optimised values of the modified Corey and van Genuchten model parameters n and g (equations (4.66) and (4.67), respectively).

Fomation	Type	k_{r10}	k_{r20}	S_{1c}	S_{2r}	n	g
		(-)	(-)	(-)	(-)	(-)	(-)
Berea	Sandstone	0.95	1.00	0.00	0.20	2.5	5.4
Paaratte	Sandstone	0.95	1.00	0.00	0.05	2.5	8.5
Mt. Simon	Sandstone	0.95	1.00	0.00	0.22	1.8	8.7
Tuscaloosa	Sandstone	0.95	1.00	0.00	0.05	2.6	16.9

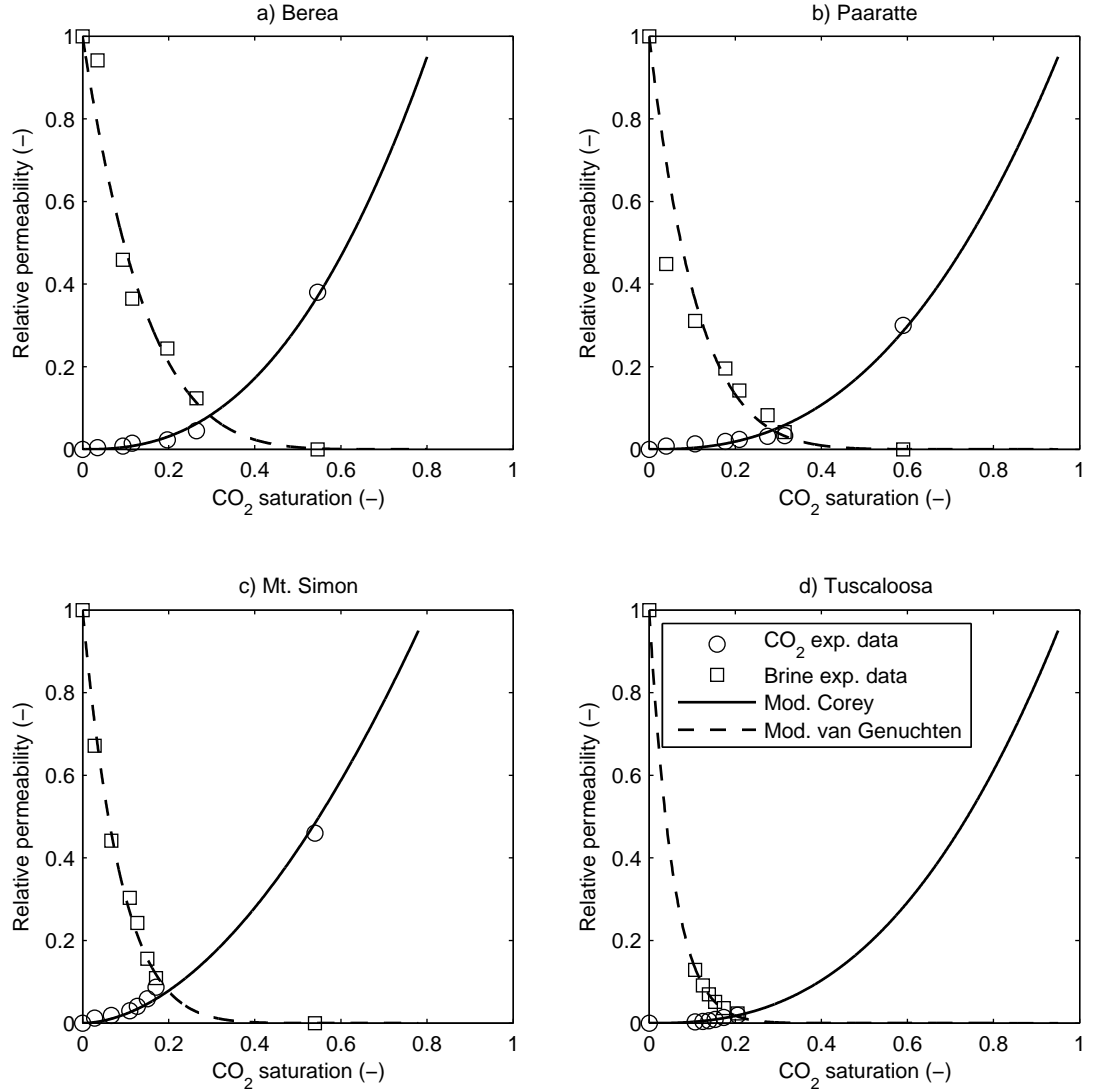


Figure 4.9: Relative permeability experimental data for the four sandstone samples (Krevor et al., 2012) and modified Corey and van Genuchten models (equations (4.66) and (4.67), respectively) with best fit parameters given in Table 4.1.

The first set of experimental data that can be used for the estimation of the Forchheimer coefficient for the mobile gas phase, b_1 was given by Wong (1970). In that study, results of Gewers and Nichol (1969), who measured the gas non-Darcy factor in low-permeability carbonates with up to 30% immobile liquid saturation, were extended to include the effects of a mobile liquid saturation in nitrogen-water systems. The experiments showed that an increase in liquid saturation from 40 to 70% could result in eight-fold increase in the non-Darcy factor. Evans and Evans (1988) obtained similar results in their nitrogen-brine experiments using Ottawa sand pack samples. For a small mobile liquid saturation, the non-Darcy flow coefficient was increased by up to three times over that for an immobile liquid saturation. The experimental data are summarised in Table 4.2.

Table 4.2: Mobile liquid saturation literature data for carbonates (Wong, 1970) and Ottawa sands (Evans and Evans, 1988).

Formation type	Sample	Effective permeability (10^{-12} m^2)	Experimental b_1 (10^7 m^{-1})	Porosity ($-$)
Carbonate	16A	0.00126	98425	0.11
	16A	0.00224	39370	0.11
	16A	0.00322	24606	0.11
	24E	0.00370	36089	0.13
	24E	0.00530	22966	0.13
	24E	0.00790	11155	0.13
	24F	0.00790	21982	0.10
	24F	0.01060	10171	0.10
	24F	0.01330	5906	0.10
Ottawa sand	20/40	29	0.01123	0.36
	20/40	31	0.01201	0.36
	20/40	32	0.01186	0.36
	20/40	33	0.01121	0.36
	20/40	33	0.01109	0.36
	20/40	36	0.01088	0.36
	20/40	36	0.01134	0.36
	20/40	44	0.00991	0.36

Table 4.2: (continued)

Formation type	Sample	Effective permeability (10^{-12} m^2)	Experimental b_1 (10^7 m^{-1})	Porosity ($-$)
	20/40	53	0.01229	0.36
	20/40	57	0.00972	0.36
	20/40	88	0.00600	0.36
	20/40	120	0.00189	0.36
	10/20	142	0.00399	0.36
	10/20	143	0.00395	0.36
	10/20	154	0.00397	0.36
	10/20	159	0.00419	0.36
	10/20	169	0.00419	0.36
	10/20	181	0.00369	0.36
	10/20	196	0.00398	0.36
	10/20	197	0.00401	0.36
	10/20	245	0.00388	0.36
	10/20	283	0.00285	0.36
	10/20	350	0.00042	0.36
	10/20	353	0.00448	0.36

The Forchheimer coefficient for the gas phase in multiphase systems can be estimated using various empirical correlations. They are extensions of relations proposed for the estimation of the non-Darcy coefficient in single-phase systems. The absolute permeability is replaced by the effective permeability, kk_r , while the porosity is substituted by the fraction of pore space occupied by gas, that is $\phi(1 - S_{2r})$ (Li and Engler, 2001). In this study, the following correlations were tested against the experimental data listed in Table 4.2:

- The correlation of Janicek and Katz (1955):

$$b_1 = \frac{W}{(kk_{r1})^{1.25}[\phi(1 - S_{2r})]^{0.75}} \quad (4.70)$$

- The correlation of Geertsma (1974):

$$b_1 = \frac{W}{(kk_r)^{0.5}[\phi(1 - S_{2r})]^{5.5}} \quad (4.71)$$

- The correlation of Kutasov (1993):

$$b_1 = \frac{W}{(kk_r)^{0.5}[\phi(1 - S_{2r})]^{1.5}} \quad (4.72)$$

- The correlation of Frederick and Graves (1994):

$$b_1 = \frac{W}{(kk_r)^{1.55}[\phi(1 - S_{2r})]} \quad (4.73)$$

where W is the Forchheimer flow constant. The constant is an optimisation parameter whose value is adjusted to obtain the best match with experimental data. Table 4.3 shows the values of W adjusted by the aforementioned authors, along with the corresponding units for b_1 and kk_r .

Table 4.3: Values of the Forchheimer flow constant, W in the original correlations (4.70)–(4.73) and the corresponding units for b and kk_r .

Correlation	W	b_1 in	kk_r in
Janicek and Katz (1955)	$1.82 \cdot 10^8$	1/cm*	mD
Geertsma (1974)	0.005	1/ft	mD
Kutasov (1993)	1432.6	1/cm	D
Frederick and Graves (1994)	$2.11 \cdot 10^{10}$	1/ft	mD

*centimetres (cm); milidarcy (mD); feet (ft); darcy (D)

In this study, the value of W in correlations (4.70)–(4.73) was optimised to obtain the best fit with the experimental data from Table 4.2. The value of residual water saturation used in calculations was $S_{2r} = 0$. Values of kk_r were in m^2 , giving the Forchheimer coefficient in m^{-1} . A first attempt was to optimise correlations to the Wong (1970) and Evans and Evans (1988) data sets simultaneously. Figure 4.10 shows that none of the equations could accurately represent all of the experimental data with a single value of W . The reason could be that non-Darcy coefficient correlations are sensitive to variations of in sample porosity (Li and Engler, 2001). While low-porosity carbonate data are well

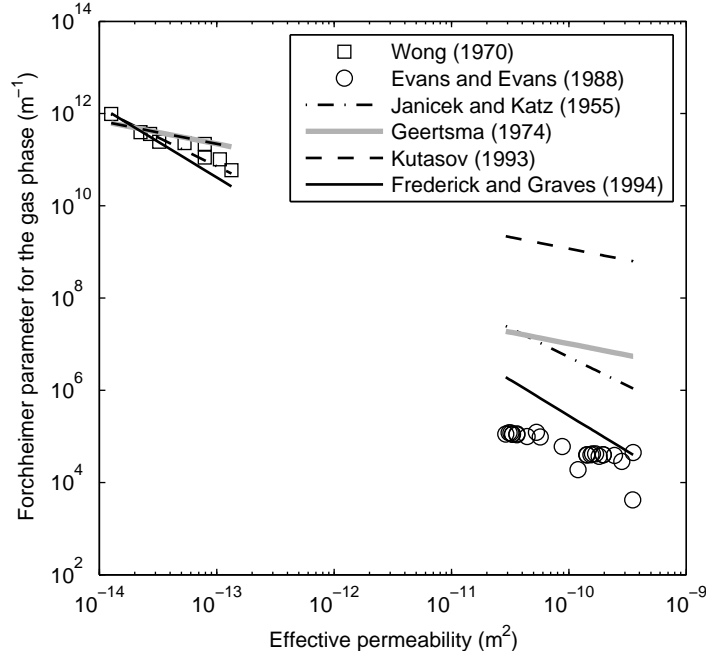


Figure 4.10: Mobile liquid phase non-Darcy coefficient experimental data and empirical correlations (4.70)–(4.73) optimised to the two data sets simultaneously. Correlation is greatly influenced by the lack of experimental data in the middle of the effective permeability range. Forchheimer coefficient for the gas phase is greatly overestimated for Ottawa sands.

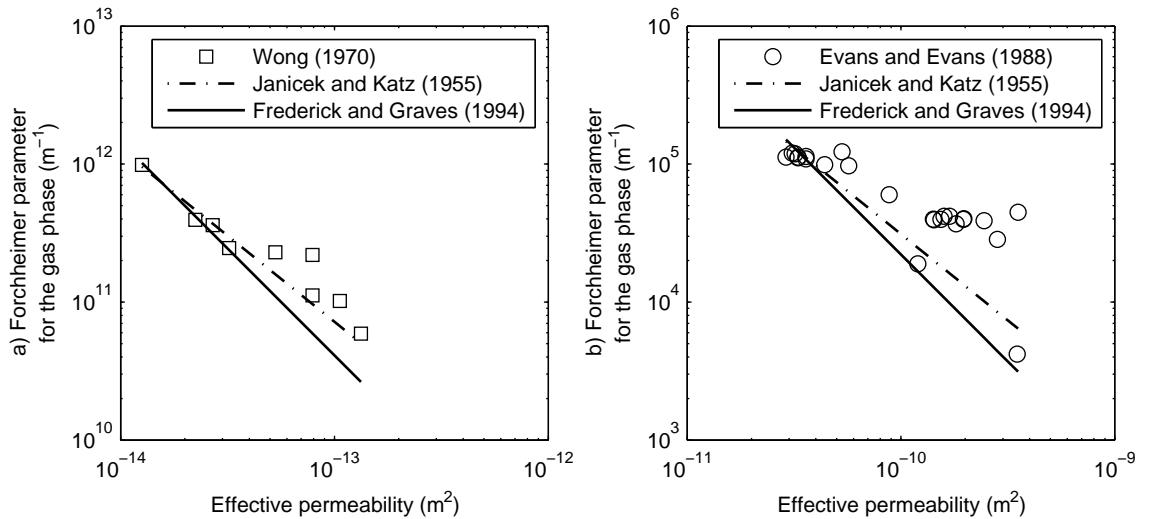


Figure 4.11: Mobile liquid phase non-Darcy coefficient experimental data and separately optimised theoretical correlations for a) Carbonate and b) Ottawa sand.

approximated, b_1 is greatly overestimated for Ottawa sands. The Frederick and Graves (1994) correlation gives the best approximation, with a value of $W = 3.2 \cdot 10^{-11} \text{ m}^{2.1}$.

To see the possible range of values of W , the Janicek and Katz (1955) and Frederick and Graves (1994) models were fitted to carbonate and Ottawa sand experimental data sets independently (Figure 4.11). Based on the results shown in Figure 4.10, these two models were selected as the most applicable for the mobile liquid systems modelling. Fitted values of W are shown in Table 4.4, together with the normalised root mean square errors (NRMSE) for each model obtained as:

$$NRMSE_b = \frac{1}{b_{1e,max} - b_{1e,min}} \sqrt{\frac{\sum_{i=1}^n (b_{1m,i} - b_{1e,i})^2}{n}} \quad (4.74)$$

where b_{1e} are the non-Darcy experimental data from Table 4.2 and b_{1m} are the values calculated from the correlations. Overall, the Janicek and Katz (1955) equation gives a better match to the experimental data, as seen by the lower values of $NRMSE_b$ for both carbonate and Ottawa sand samples. However, the Forchheimer flow constants are two orders of magnitude different. This could indicate the range of inertial effects in the non-Darcy flow of gas, that may occur in two-phase systems with a mobile liquid phase.

Table 4.4: Values of Forchheimer flow constant, W obtained by optimising the empirical correlations to the experimental data sets independently.

Formation type	Janicek and Katz (1955)		Frederick and Graves (1994)	
	W ($\text{m}^{1.5}$)	$NRMSE_b$ (%)	W ($\text{m}^{2.1}$)	$NRMSE_b$ (%)
Carbonate	$7.7 \cdot 10^{-7}$	6.3	$3.2 \cdot 10^{-11}$	8.2
Ottawa sand	$4.6 \cdot 10^{-9}$	20.2	$2.5 \cdot 10^{-12}$	24.5

The above correlations assume that all the available pore space is occupied by gas, except for the volume taken by the residual liquid saturation. However, in the two-phase region, the pore space is potentially occupied by mobile liquid, which could alter the value of the Forchheimer flow coefficient. To account for the effect of the variable gas saturation,

Wu (2001) modified the Janicek and Katz (1955) formulation to:

$$b_1 = \frac{W}{(kk_{r1})^{1.25}[\phi(S_1 - S_{1c})]^{0.75}} \quad (4.75)$$

Assuming that the saturation dependance of the gas phase relative permeability is described by the Corey (1954) model, the values of b_1 obtained from equation (4.75) were fitted to the experimental data of Evans and Evans (1988) (Figure 4.12). Data from the Wong (1970) study could not be used due to the lack of intrinsic permeability data. The best model fit was obtained with $W=3.2 \cdot 10^{-9} \text{ m}^{1.5}$, which was the value of the Forchheimer flow constant used in the simulations carried out by Wu (2001).

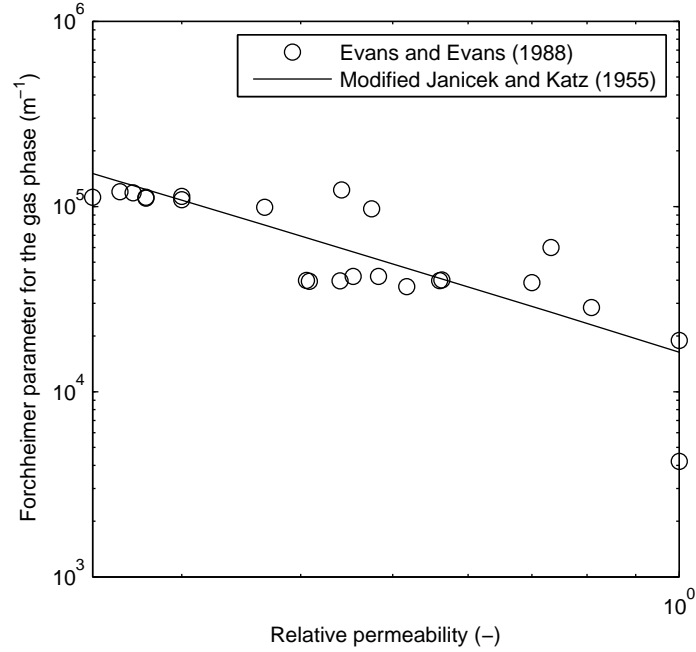


Figure 4.12: Mobile liquid phase non-Darcy coefficient experimental data for Ottawa sand fitted using the saturation dependent correlation (4.75).

In the present study, the Forchheimer coefficient for the gas phase was obtained from equation (4.75), with the values of the Forchheimer flow constant in the range of $3.2 \cdot 10^{-9} \leq W \leq 3.2 \cdot 10^{-7} \text{ m}^{1.5}$. The value for the upper limit of W was chosen based on the value obtained by fitting to the data of (Wong, 1970).

4.4 Model results

The example presented here shows the performance of the non-Darcy analytical solution using the initial and boundary conditions and formation characteristics detailed in Table 4.5. Gas and liquid phase relative permeability functions are shown in Figure 4.13. They were calculated using equations (4.66) and (4.67), respectively, with the model parameters given in Table 4.5. Injection rates were selected based on the range that is of practical interest for commercial CO₂ sequestration projects (Oldenburg et al., 2004; Zhou et al., 2008). Fluid properties were estimated at the initial reservoir pressure as described in section 4.3.1. It should be noted that the assumption of constant reservoir properties calculated at the initial pressure is not physically realistic, as both density and viscosity of CO₂ and brine will change with the pressure change in the aquifer, which will be addressed in Chapter 6.

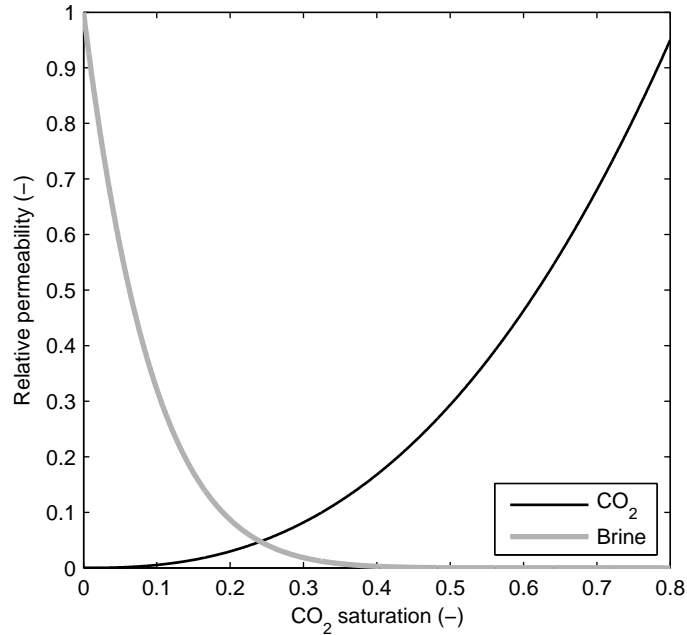


Figure 4.13: CO₂-brine system relative permeability functions. Input data are shown in Table 4.5.

Equation (4.75) was used to determine the dependence of the Forchheimer coefficient for the gas phase, b_1 on the phase saturation. By analysing equation (4.75), it can be concluded that as the gas phase becomes less mobile, that is as its saturation approaches

Table 4.5: Parameters used for the analytical model simulations and values of fluid properties at the initial reservoir pressure.

Parameter	Value
Well radius, r_w (m)	0.2
Radial extent of the reservoir, r_e (m)	5000
Porosity, ϕ (—)	0.2
Initial pressure, P_0 (MPa)	12
Temperature, T (°C)	45
Salt concentration, K_s (g cm ⁻³)	0.15
Critical CO ₂ saturation, S_{1c} (—)	0
Residual brine saturation, S_{2r} (—)	0.2
End-point relative permeability for CO ₂ , k_{r10} (—)	0.95
End-point relative permeability for brine, k_{r20} (—)	1.0
Corey model parameter, n (—)	2.5
van Genuchten model parameter, g (—)	8.5
Injection rate, Q_m (kg s ⁻¹)	30 or 100 or 120
Forchheimer flow constant, W (m ^{1.5})	$3.2 \cdot 10^{-9}$ or $3.2 \cdot 10^{-8}$ or $3.2 \cdot 10^{-7}$
Formation thickness, H (m)	50 or 200
Permeability, k (m ²)	10^{-13} or 10^{-12}
Gas phase density, ρ_1 (kg m ⁻³)	640
Gas phase viscosity, μ_1 (Pa s)	$4.99 \cdot 10^{-5}$
Liquid phase viscosity, μ_2 (Pa s)	$8.91 \cdot 10^{-4}$
Liquid phase compressibility, c_2 (Pa ⁻¹)	$5 \cdot 10^{-10}$

the critical value, the influence of the non-Darcy effect becomes more significant. However, if the influence of the gas phase flow velocity is included through equation (4.17), the overall inertial effects can be analysed through the behaviour of the factor β . Figure 4.14 shows that the non-Darcy effect is most significant in a very narrow area around the well. At radial distances larger than about 1 meter, β becomes nearly constant and approaches its limiting value of 1 in Darcy flow conditions. The significant increase of b_1 values for low gas saturations does not necessarily imply a large pressure increase at the injection well in equation (4.11). However, the pressure buildup in the near-well region will be greater than under Darcy flow conditions.

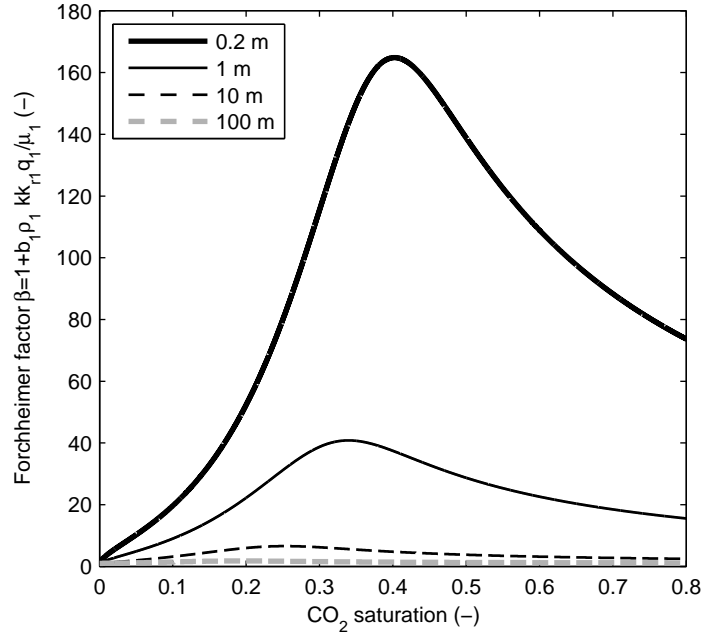


Figure 4.14: Inertial effects as a function of the gas phase saturation for $Q_m=100 \text{ kg s}^{-1}$ and $W=3.2 \cdot 10^{-7} \text{ m}^{1.5}$.

4.4.1 Non-Darcy fractional flow curves

Once the influence of inertial effects is defined as described in section 4.2.1, it is possible to determine the non-Darcy fractional flow curve for any radial distance from the well. In all the simulation results presented, the error tolerance was set to 10^{-5} and the number of iterations was limited to 100. The volumetric injection rate, Q was obtained based on

the mass injection rate Q_m :

$$Q = \frac{Q_m}{\rho_1} \quad (4.76)$$

Fractional flow curves for several distances from the well for a set injection rate and non-Darcy flow constant are shown in Figure 4.15. The non-Darcy effect is most significant near the well, where, for a given saturation value, the inertial effects significantly slow down the gas phase flow. As the gas front advances into the reservoir, the non-Darcy flow fraction becomes less significant and the flow conditions approach those of Darcy law (solid grey line in Figure 4.15). The extent of the non-Darcy effect depends upon the reservoir characteristics, the injection rate and the assumed level of inertial effects that is defined by the constant W . Once gas is flowing under linear conditions, the Darcy fractional flow curve applies for all the distances $r \geq r_d$ (Figure 4.16).

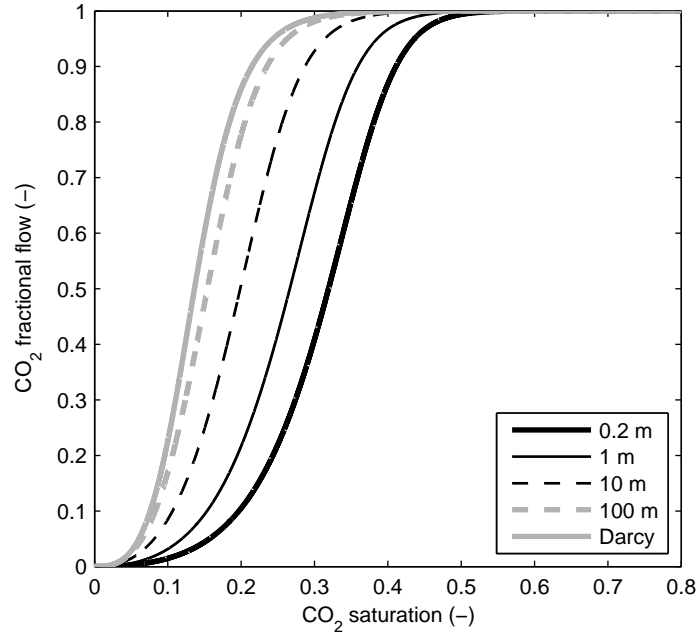


Figure 4.15: Non-Darcy fractional flow curves as a function of the gas phase saturation and radial distance from the well for $Q_m=100 \text{ kg s}^{-1}$ and $W=3.2 \cdot 10^{-7} \text{ m}^{1.5}$.

While the Buckley and Leverett (1942) solution suggests that the phase fractional flow is independent of the formation characteristics, under non-Darcy conditions that is not the case. Figure 4.17 shows the sensitivity of the non-Darcy fractional flow function to

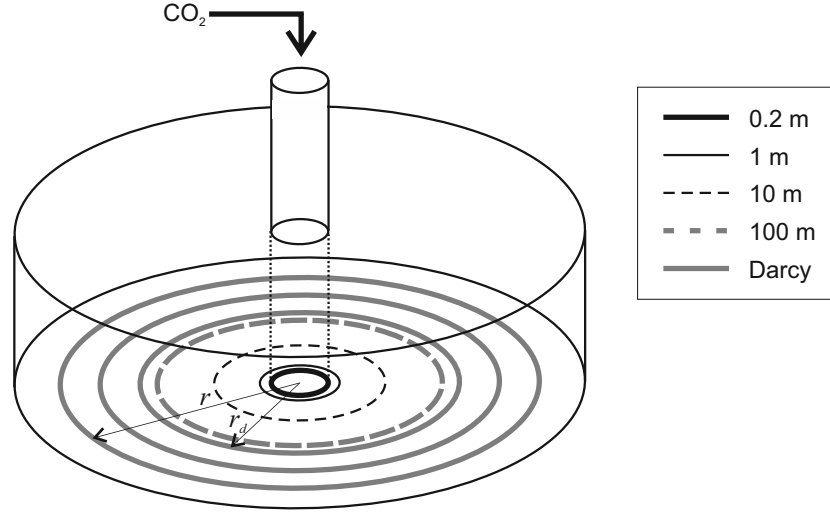


Figure 4.16: Schematic representation of the influence of the non-Darcy effect in a radial CO₂-brine displacement. For $r > r_d$, the non-Darcy effect is insignificant.

the variations of the formation thickness and permeability. The non-Darcy effect is most significant in low-permeable formations where the pore space available for two-phase flow is limited (Figure 4.17a). Inertial effects significantly reduce gas phase velocity in the near-well region. Moreover, in these circumstances non-Darcy effects are felt more than 100m from the well. Selecting aquifers with increased permeability and/or larger formation thickness leads to the reduction of non-Darcy effects and a narrowing of the region of non-Darcy flow. In high-permeability, thick formations, the non-Darcy effects are limited to distances of only tens of metres from the well (Figure 4.17d).

The impact of the convergence of the Picard iterative scheme for determining the non-Darcy gas phase velocity was tested by examining the number of iterations required to meet the error tolerance criterion. Two parameters were varied: 1) Forchheimer flow constant, W and 2) radial distance from the well, r . Results in Table 4.6 show that a good initial assumption for the pressure distribution enables the iterative procedure to be computationally very efficient. For all analysed cases, the scheme converged in less than 30 iterations. However, the method is sensitive to variations of W and r . As the divergence from the linear flow conditions increases, that is at the locations closer to the well and with higher non-Darcy flow constant, more iterations are needed in order to obtain the correct solution.

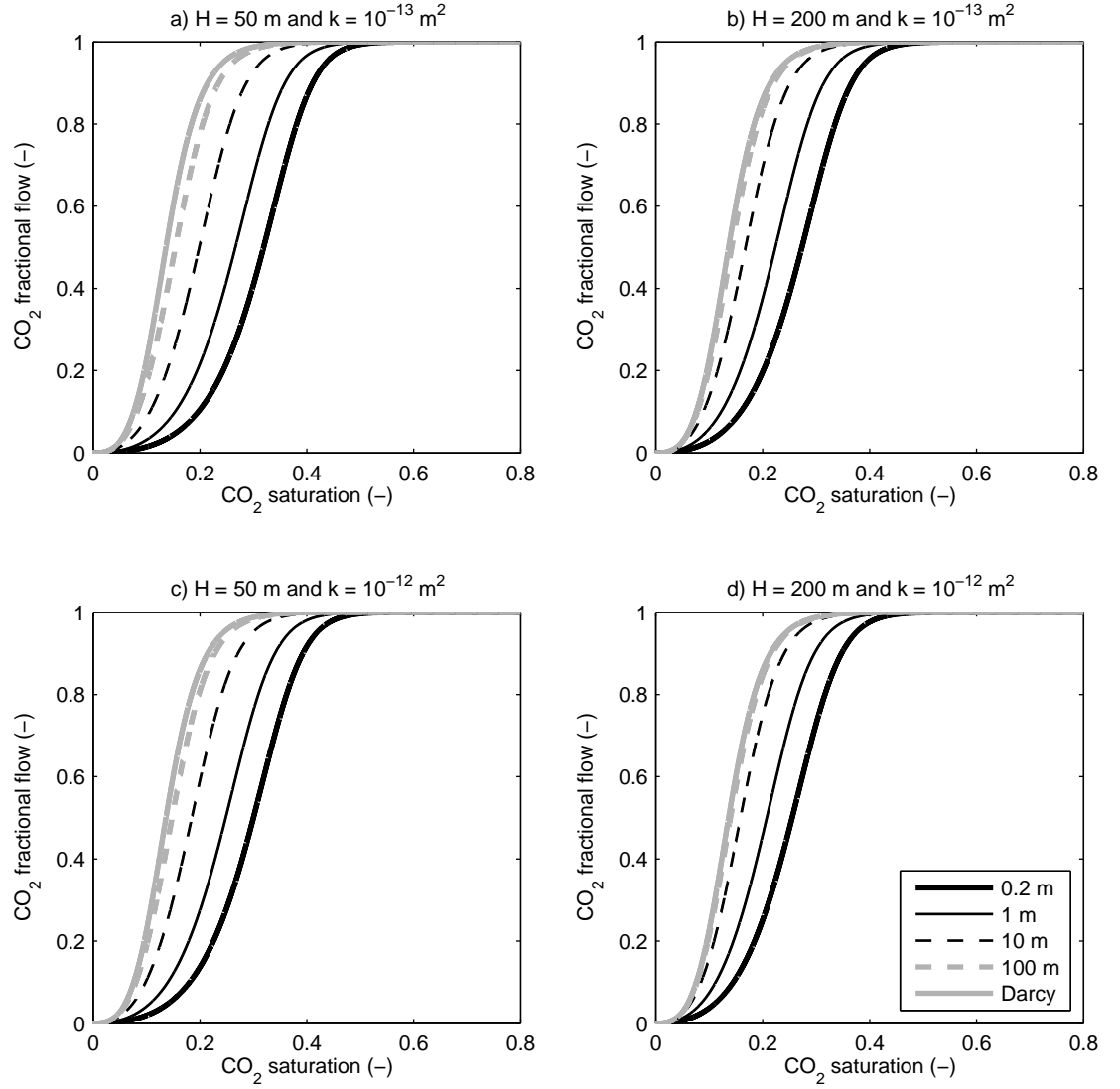


Figure 4.17: Comparison of non-Darcy fractional flow curves with respect to the formation thickness and permeability. Figure 4.17a corresponds to Figure 4.15.

Table 4.6: Performance of the Picard scheme: Number of iterations as a function of the Forchheimer flow constant and radial distance from the well for $Q_m=100 \text{ kg s}^{-1}$, $H=50 \text{ m}$ and $k=10^{-13} \text{ m}^2$.

$r \text{ (m)}$	$W \text{ (m}^{1.5}\text{)}$		
	$3.2 \cdot 10^{-9}$	$3.2 \cdot 10^{-8}$	$3.2 \cdot 10^{-7}$
0.2	16	23	26
1	11	21	24
10	5	18	21
100	3	11	18

4.4.2 Saturation profiles

Saturation profiles and shock fronts for any combination of parameters can be calculated using equations (4.36) and (4.37), respectively. One interesting aspect of the non-Darcy displacement is its influence on the displacement characteristics (Figure 4.18). As the wave velocity is a function of both saturation and the non-Darcy flow constant, the shock front will travel much more slowly in the case of non-Darcy flow. The explanation is that inertial effects slow down the gas phase flow compared to the case under Darcy flow conditions ($W=0$). Consequently, the displacement efficiency, that is the fraction of brine that is displaced from a unit volume of the aquifer, will be higher. This is favourable for CO_2 injection processes as higher gas saturations imply a larger storage capacity. Neglecting the non-Darcy behaviour can also lead to the overestimation of the lateral extent of the gas plume.

Under Darcy flow conditions, the shock saturation is not dependent on the injection rate. However, this is not the case when there is non-Darcy flow. The influence of the variable injection rate can be analysed by injecting a fixed mass of CO_2 . Computationally that was achieved by fixing the $Q_m t$ term in the expression for dimensionless time t_D (see equation (4.26)). Figure 4.19 shows that the shock front moves more slowly for the faster, more turbulent injection, which is due to the larger flow resistance to the gas phase when the injection rate is increased. As expected, higher injection rates will enhance the non-Darcy effect, resulting in higher gas saturations and hence better displacement efficiency. If the maximal allowable injection pressure is not reached, increasing injection rate allows larger volumes of CO_2 to be injected into a given reservoir volume.

Another interesting feature of the non-Darcy flow is the temporal change in saturation

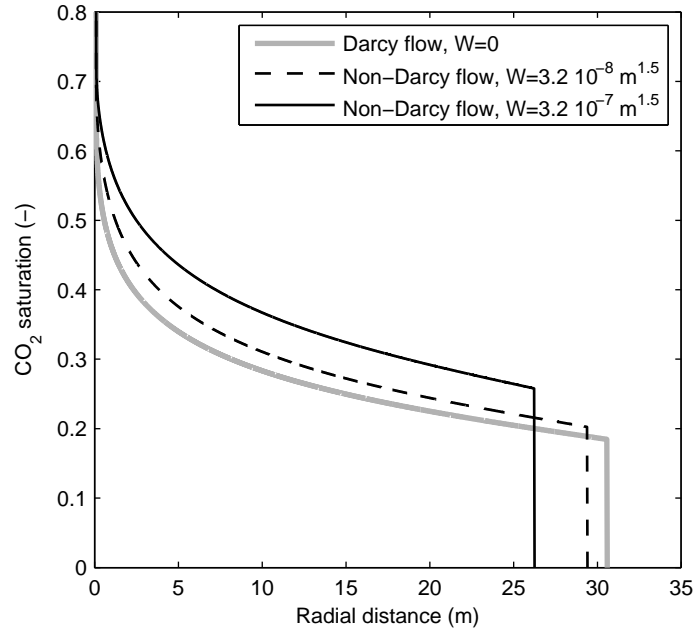


Figure 4.18: Saturation profiles of Darcy and non-Darcy displacements 12 hours after the beginning of the injection at the rate $Q_m=100 \text{ kg s}^{-1}$. The formation thickness is $H=50 \text{ m}$ and permeability is $k=10^{-13} \text{ m}^2$.

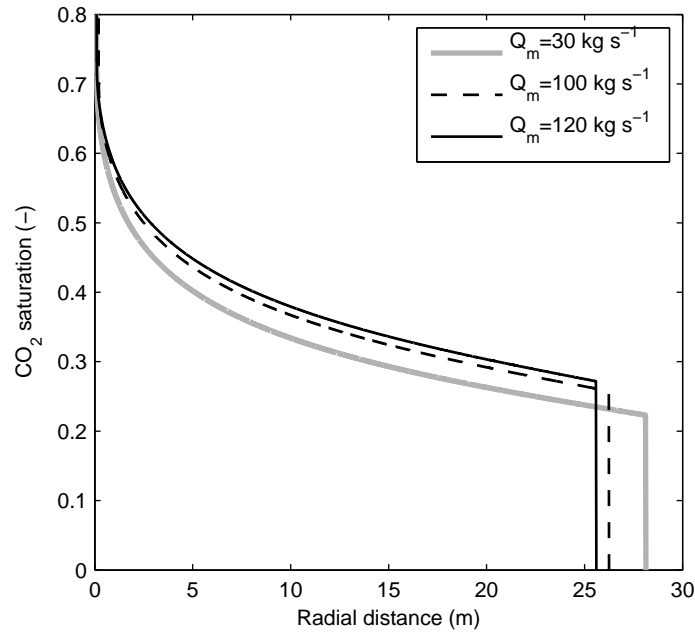


Figure 4.19: Saturation profiles of non-Darcy displacements for various mass injection rates, after a fixed mass of CO_2 has been injected for $W=3.2 \cdot 10^{-7} \text{ m}^{1.5}$, $H=50 \text{ m}$ and $k=10^{-13} \text{ m}^2$.

distribution. Figure 4.20 shows the results for formation thicknesses of 50 and 200 metres. Non-Darcy effects are most significant immediately after the injection begins, when the saturation front is close to the well. At this time, the leading front saturation is significantly higher than the one under Darcy conditions. As the front advances into the reservoir, non-Darcy flow effects decrease and leading shock saturations start to converge to the Darcy value. After this, the shock front will continue to advance with a constant velocity and saturation given by the Buckley and Leverett (1942) solution. A summary of simulations results is given in Table 4.7.

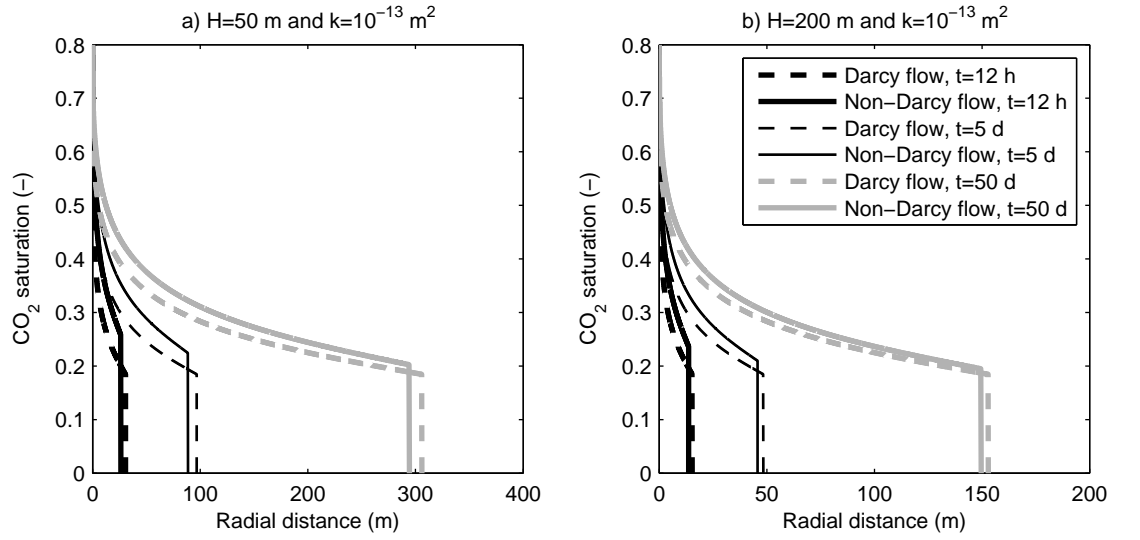


Figure 4.20: Comparison of CO₂ saturation distributions for cases a) and b) shown in Figure 4.17. Time is set to 0.5, 5 and 50 days after the beginning of the injection. The injection rate is $Q_m=100 \text{ kg s}^{-1}$ and the Forchheimer flow constant for non-Darcy flow is $W=3.2 \cdot 10^{-7} \text{ m}^{1.5}$.

4.4.3 Pressure buildup

Once the saturation profile has been determined, pressure can be calculated for any radial distance from the well. To emphasise the near-well area, results for pressure are presented with the x -axis set logarithmically. Results for an open aquifer and case *a* from Figure 4.20 before the pressure perturbation has reached the boundary ($t \leq t_c = 115$ days) are presented in Figure 4.21. The rapid pressure increase under non-Darcy conditions close to the well is expected, due to the significant influence of inertial effects in that zone.

Table 4.7: Simulation results for Darcy and non-Darcy flow for two cases shown in Figure 4.20: a) $H=50$ m and $k=10^{-13}$ m² and b) $H=200$ m and $k=10^{-13}$ m². The injection rate is $Q=100$ kg s⁻¹ and the initial pressure is $P_0=12$ MPa. Subscript L denotes the value of the parameter at the leading shock front.

		Case <i>a</i>			Case <i>b</i>	
	time (days)/ W (m ^{1.5})	0	$3.2 \cdot 10^{-8}$	$3.2 \cdot 10^{-7}$	0	$3.2 \cdot 10^{-7}$ m ^{1.5}
S_{1L} (—)	0.5	0.1845	0.2024	0.2577	0.1845	0.2363
r_L (m)	0.5	30.6	29.4	26.2	15.3	13.7
P_w (MPa)	0.5	34.2	41.9	94.2	18.2	23.7
S_{1L} (—)	5	0.1845	0.1914	0.2242	0.1845	0.2095
r_L (m)	5	96.7	95.4	88.6	48.4	45.8
P_w (MPa)	5	34.8	40.2	80.4	18.4	22.2
S_{1L} (—)	50	0.1845	0.1870	0.2024	0.1845	0.1948
r_L (m)	50	306	305	294	153	150
P_w (MPa)	50	35.4	39.4	71.4	18.5	21.4

Furthermore, as the inertial effects increase, the non-Darcy influence spreads further into the reservoir. Another interesting feature of the plot is the large increase in the near-well pressure as W changes by an order of magnitude from 10^{-8} to $10^{-7} \text{ m}^{1.5}$ (for numerical values see Table 4.7). This suggests that there may be a threshold value of the non-Darcy flow for a given formation and injection rate, above which the pressure buildup could induce the fracturing of the reservoir rock.

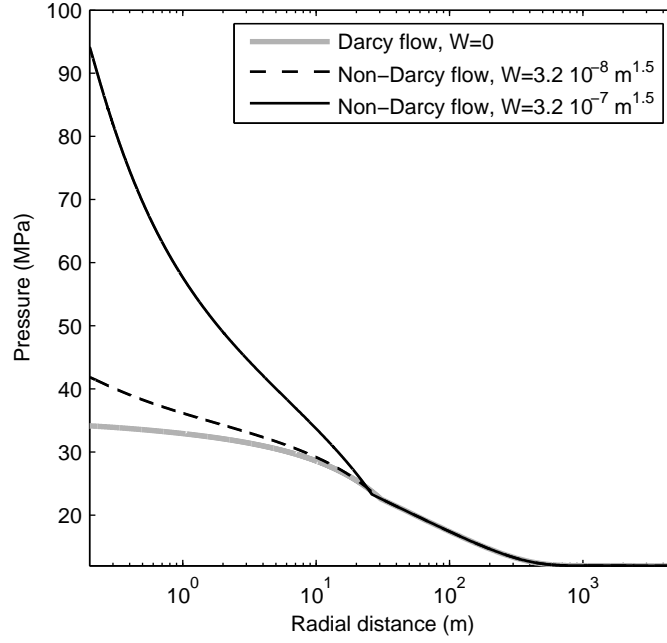


Figure 4.21: Pressure distribution along the reservoir for Darcy and non-Darcy flow 12 hours after the beginning of the injection. Open flow boundary is set at $r=5000 \text{ m}$. Remaining parameters are $Q_m=100 \text{ kg s}^{-1}$, $H=50 \text{ m}$ and $k=10^{-13} \text{ m}^2$.

Figure 4.22 shows the change of the open reservoir pressure in time for two different formation thicknesses. The thinner formation has a much higher pressure increase, both under Darcy and non-Darcy flow conditions. Interestingly, while the well pressure under linear flow conditions increases slightly in time, which is expected since the pressure perturbation is not yet influenced by the formation boundary, the non-Darcy well pressure decreases with respect to time after the beginning of the injection. The reason for such behaviour is related to the saturation dependence of the non-Darcy effect. At early times, the saturation front is close to the well and the whole profile is affected significantly by

inertial effects. As the saturation front advances into the reservoir, the far-field component of the saturation profile approaches Darcy flow conditions, while the gas saturation near the well approaches $1 - S_{2r}$.

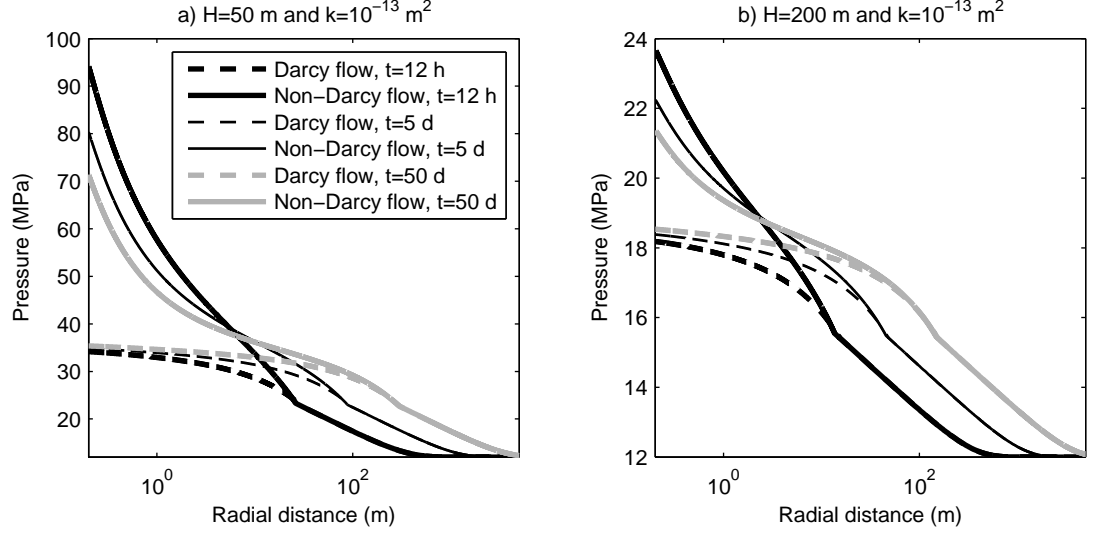


Figure 4.22: Comparison of pressure distributions for cases a) and b) shown in Figure 4.17. Time is set to 0.5, 5 and 50 days after the beginning of the injection, before the boundary impacts the pressure. The injection rate is $Q_m=100 \text{ kg s}^{-1}$ and the Forchheimer flow constant for non-Darcy flow is $W=3.2 \cdot 10^{-7} \text{ m}^{1.5}$. Open flow boundary is set at $r=5000 \text{ m}$.

The pressure distribution within the formation depends on the far-field boundary conditions. The response of both closed and open systems, after the influence of the boundary is felt at the well, is shown in Figure 4.23. In open formations, the constant pressure at the outer boundary determines the reservoir pressure distribution. As the two-phase mobility begins to dominate the displacement process in the reservoir, both Darcy and non-Darcy well pressures will decrease in time due to the relative permeability effects. In non-Darcy flow, the critical pressure buildup will occur immediately after the beginning of the gas injection process.

Conversely, in closed aquifers the accumulation of the fluids within the formation results in an additional pressure rise under both linear and non-Darcy flow conditions, as can be seen in the right side of Figure 4.23. This significant pressure buildup limits the injectivity of such formations. Due to well interference, the same problem can occur in systems

containing multiple wells. Therefore, multiple well systems should be carefully monitored to ensure the pressure does not increase above the formation fracture limit.

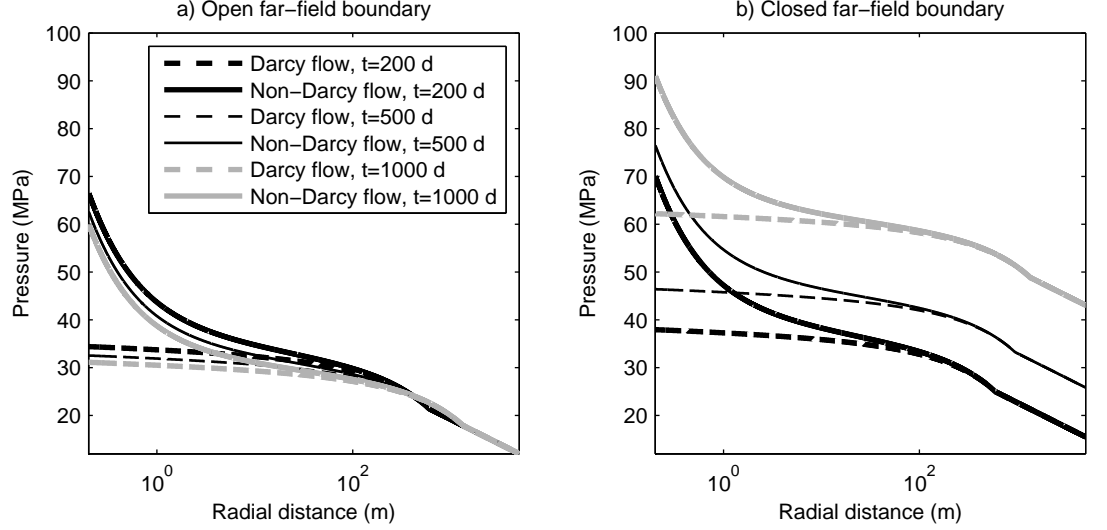


Figure 4.23: Comparison of pressure distributions for: a) open and b) closed formations. Time is set to 200, 500 and 1000 days after the beginning of the injection. The pressure effect has reached the boundary at $t=115$ and 62 days in open and closed formations, respectively. The parameters are $Q_m=100 \text{ kg s}^{-1}$, $W=3.2 \cdot 10^{-7} \text{ m}^{1.5}$, $H=50 \text{ m}$ and $k=10^{-13} \text{ m}^2$. The far-field boundary condition is set at $r=5000 \text{ m}$.

4.4.4 Comparison with a finite difference solution

In order to verify the method approach presented here, equation (4.27) was solved numerically using a forward in space finite difference approximation with an implicit scheme. For every time step, the following numerical representation of the problem:

$$\frac{\Delta S_1}{\Delta t_D} = - \left(\frac{f_{1,i+1} - f_{1,i}}{\Delta r_D} \right) \quad (4.77)$$

was solved using MATLAB code with ordinary differential equation solver ode15s. The subscripts i and $i + 1$ denote current and forward space nodes in the radial direction, respectively. The values of $f_1 = f_1(S_1, r_D)$ were calculated by implementing the same iterative scheme as used in the analytical solution.

Simulation results are presented in Figure 4.24. The numerical grid has intervals equal

to $\Delta r_D = 0.001$. The same resolution is used in the analytical simulation used for comparison. The plots show excellent agreement between numerical and analytical solutions for both Darcy (lower saturation profiles) and non-Darcy flow, verifying the numerical model and the proposed approach to the non-Darcy modelling of the gas-liquid systems. The numerical model is prone to numerical diffusion, leading to inaccurate prediction of the leading front characteristics, especially under non-Darcy flow conditions. To overcome this problem, grid resolution can be increased, but at the cost of computational efficiency.

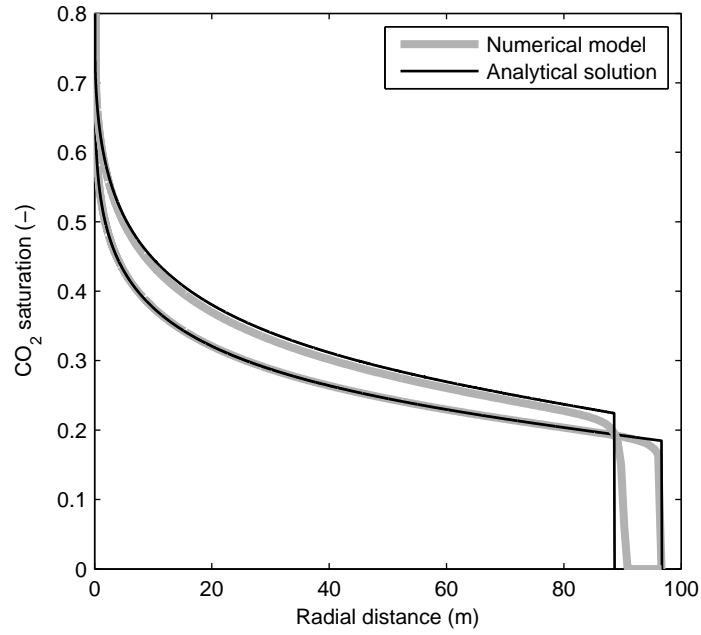


Figure 4.24: Comparison between analytical and numerical solutions for Darcy (lower saturations) and non-Darcy (higher saturations) flow 5 days after the beginning of the injection. The injection rate is $Q_m=100 \text{ kg s}^{-1}$ and the Forchheimer flow constant is $W=3.2 \cdot 10^{-7} \text{ m}^{1.5}$.

4.4.5 Limitations of the proposed solution

The application of the proposed solution to the analysis of full physics problems is limited by the underlying assumptions of phase incompressibility and immiscibility. Under Darcy flow conditions, the effects of CO_2 compressibility on storage in saline aquifers were analysed in Vilarrasa et al. (2010). They concluded that the influence on the interface po-

sition is not significant when viscous effects dominate. However, the pressure increase was overestimated when gas compressibility was neglected. Mathias et al. (2011a) examined the role of partial miscibility on pressure buildup. The well pressure declined due to the development of the dry-out zone and a corresponding increase in CO₂ relative permeability in the near-well region. In addition, the leading front saturation in compositional displacement will be higher than when the phase behaviour is neglected. Therefore, when Darcy flow conditions are valid, both phase behaviour and compressibility may lower reservoir pressures and increase the leading shock front saturation.

Under non-Darcy flow conditions, it can be assumed that the effects of compressibility and miscibility will become even more significant. Under the assumption of gas incompressibility, the parameter B_1 (see equation (4.14)), which defines the level of inertial effects, is a function of saturation only. In pressure dependent flow conditions however, its value will additionally vary due to the influence of the gas density. As non-Darcy effects are the most significant in the vicinity of the well, it is expected that gas compressibility will have a positive effect on injectivity by reducing the pressure peak that occurs at the well. The non-Darcy flow in compositional displacement is expected to reduce the rate of evaporation in the near-well region, and therefore contribute to the reduction of solid salt precipitation. Furthermore, combined with the compositional displacement, a reduction in pressure due to CO₂ compressibility will additionally affect evaporation of water and dissolution of CO₂ in aqueous phase. Hence, the non-Darcy solution proposed in this chapter is likely to overestimate well pressure and underestimate saturation at the displacement front. Therefore, it is the worst-case solution for a given set of input data.

Further limitation of the proposed model is related to the temperature change in the near-well region. Injected gas is cooler than the ambient formation temperature, and thermal effects such as Joule-Thomson cooling may occur. This effect represents a drop in temperature that occurs when a gas such as CO₂ expands from high pressure to low pressure at constant enthalpy. This could potentially have a significant impact on the loss of injectivity due to freezing of the resident brine (Oldenburg, 2007; Mathias et al., 2010).

Finally, the near-well region is likely to be highly heterogenous. Although the analytical solution in this study accounts for potential rapid changes in pressure under non-Darcy flow by refining the grid spacing close to the well, it cannot represent the changes in formation properties. Chandra et al. (2011) developed a high-resolution numerical scheme, which allowed representation of geological heterogeneity in the near-well region and improved fundamental understanding of interactions between the aquifer and the well. Results from

the present study could be an indicator if further grid refinement in numerical simulators is needed to account for non-Darcy effects.

4.5 Conclusions

Analytical solutions to two-phase flow systems are a useful tool for the preliminary analysis of complex problems such as CO₂ injection in saline aquifers. Though the well-established Buckley and Leverett (1942) formulation has been implemented successfully in a variety of oil recovery analyses, gas-liquid problems may require the extension of the model in order to account for the non-Darcy behaviour of the gas phase in the near-well region. This chapter presented the development of an analytical model for radial, non-Darcy two-phase flow, in which fractional flow is a function of both saturation and the distance from the well. Using the iterative procedure presented, equation (4.24) can be used to calculate the non-Darcy fractional flow function. Furthermore, the solution for the saturation profiles and shock front can be obtained by using equations (4.36) and (4.37), respectively.

The analysis of correlations for estimating fluid properties has shown that within the range of conditions representative of sedimentary basins, CO₂ properties are strongly pressure dependent, while brine properties vary with changes in temperature and salinity. By comparison with experimental data, power-law correlations were shown to most accurately represent the CO₂-brine system relative permeability curves. However, more experimental data in the middle of the effective permeability range ($10^{-13} \leq kk_{r1} \leq 10^{-11}$), and data for CO₂-brine systems are necessary to support the selection of the correlation for the Forchheimer coefficient for the gas phase, b_1 .

The results of the model application have shown that:

- Inertial effects are most significant in the area close to the well (Figure 4.15). As the distance from the well increases, the non-Darcy flow conditions become less significant, and the classical Buckley and Leverett (1942) solution can be used.
- The non-Darcy effects are most significant in low-permeability formations when gas is injected at high rates because of the largest resistance to phase flow within the limited pore space.
- In non-Darcy systems, the phase saturation at the shock front is controlled not only by the relative permeability functions, but also by the injection rate and the magnitude of the inertial effects, defined by the Forchheimer flow constant, W (Figures

4.18 and 4.19). In addition, the shock front velocity and saturation change in time as the displacement progresses into the reservoir (Figure 4.20 and Table 4.7). As the shock front moves further from the well, its saturation decreases but the shock accelerates until the Darcy flow limit is reached.

- There could be a limiting value of the Forchheimer flow constant, below which pressure increases are negligible compared to Darcy flows (Figure 4.21). Above that value, there is a significant additional pressure buildup that could limit the rate of gas injection due to the risk of fracturing.
- Before the pressure change reaches the boundary, the Darcy critical pressure at the well increases insignificantly, while non-Darcy systems follow the opposite pattern. For systems with closed formations, an additional pressure increase due to the influence of the far-field boundary condition was seen (Figure 4.23).

The verification of the proposed solution was confirmed by comparison with the corresponding numerical model (Figure 4.24). By neglecting the effects of compressibility and miscibility, the proposed solution is likely to estimate the upper limit values of well pressure and lower limit values of shock saturation for a given set of input data.

The preliminary analysis of CO₂ sequestration scenarios requires a reliable tool which takes into account as many characteristics of two-phase system behaviour as possible. The selection of the injection rate for CO₂ sequestration is a trade-off between the larger storage capacity over a short period of time and the larger pressure buildup. In examples presented in this chapter it was shown that non-Darcy conditions are more favourable for CO₂ storage than Darcy flow due to better displacement efficiency. The gas front will advance more slowly and will occupy more pore volume near the well over the same period of time. However, this comes at the cost of higher injection pressure at the well. Additional work has to be undertaken in order to examine the level of non-Darcy effects likely to occur in reservoirs suitable for CO₂ injection at reasonable injection rates, to confirm the values of Forchheimer flow constants used in the model presented here. Furthermore, the extension of the solution to include compressibility and partial miscibility and its comparison to commercial simulators would contribute significantly to the model usefulness for real storage analysis.

Chapter 5

Effects of partial miscibility

5.1 Introduction

When CO_2 is injected into an aquifer for storage, partial miscibility of CO_2 with water causes a three-region system to form in the reservoir. The three regions that form are: 1) a dry-out zone that develops immediately around the well, 2) an intermediate two-phase zone and 3) a brine zone ahead of the leading shock (Figure 5.1).

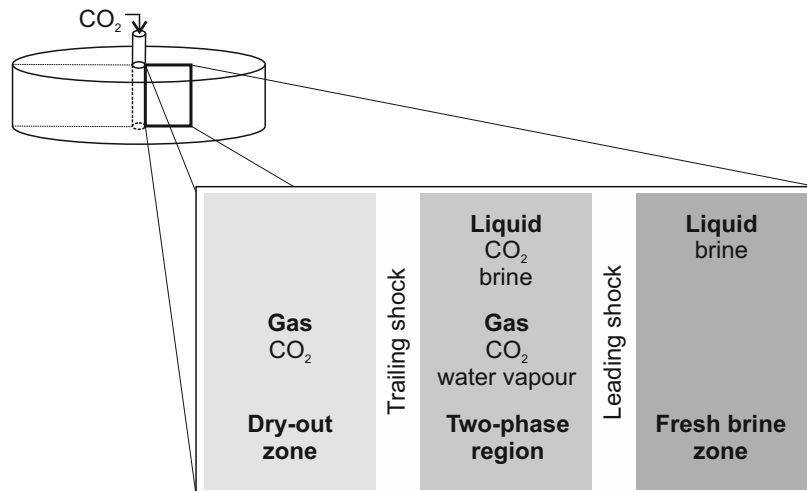


Figure 5.1: Approximation of the compositional model of CO_2 injection into a saline formation (Zeidouni et al., 2009).

The dry-out zone, which contains only gas, as all the water is either evaporated or displaced, did not appear in the displacement in the preceding chapter. Compared to

the immiscible case, the compositional displacement forms an additional shock front (the trailing shock), which determines the near-well zone with a constant CO₂ composition. The dry-out zone increases the pore space available for gas flow as compared with the examples in Chapter 4. However, that pore space may be reduced due to precipitation of salt that previously resided in the brine. This may decrease the near-well permeability and lead to a loss of the gas injectivity as compared with pure-water systems. To explore these effects, it is necessary to determine the amount of salt that will precipitate in the near-well region. Existing solutions (Burton et al., 2008; Pruess and Müller, 2009; Pruess, 2009; Zeidouni et al., 2009; Mathias et al., 2011a) imply that salt saturation can be obtained as a function of saturation at the trailing shock front, which is explained in more detail in section 2.3.2.

Saturation profiles can be obtained from fractional flow theory and strongly depend on the component flow velocities that form the convective part of the mass balance equation (Orr, 2007). In the previous chapter it was shown that the near-well flow can be significantly altered by non-Darcy effects. However, the solution presented in Chapter 4 was developed for immiscible displacement, and it cannot be used to model changes in the effective permeability due to processes that occur during gas injection into saline formations. This chapter presents the extension of the immiscible non-Darcy solution in the previous chapter. The improved model is used to explore the effects of partial miscibility on saturation and pressure profiles, as well as salt precipitation in the near-well region. The performance of the model is tested by comparison of analytical results with those obtained using ECLIPSE 300 simulations. Finally, this chapter discusses the influence of the Forchheimer flow parameter on the development of the dry-out zone and the implications for CO₂ injectivity.

5.2 Compositional non-Darcy two-phase displacement

If effects of miscibility are taken into account, then the mass continuity equation (4.9) can be extended to model incompressible, two-phase, two-component radial flow (Orr, 2007; Mathias et al., 2011a):

$$\frac{\partial}{\partial t}(w_{1c}\rho_c S_c + w_{1b}\rho_b S_b) + \frac{Q}{\pi H \phi} \frac{\partial}{\partial (r^2)}(w_{1c}\rho_c f_c + w_{1b}\rho_b f_b) = 0 \quad (5.1)$$

$$\frac{\partial}{\partial t}(w_{2c}\rho_c S_c + w_{2b}\rho_b S_b) + \frac{Q}{\pi H \phi} \frac{\partial}{\partial(r^2)}(w_{2c}\rho_c f_c + w_{2b}\rho_b f_b) = 0 \quad (5.2)$$

where w_{1c} , w_{2c} , w_{1b} and w_{2b} are the mass fraction of CO₂ (subscript c) and brine (subscript b) components in the gas (subscript 1) and liquid (subscript 2) phases, respectively, and ρ is the phase mass density with a dissolved component. Other notations correspond to those defined in Chapter 4. If the volume of each component does not change when components transfer from one phase to the other, then the local flow velocity is constant and equal to the injection velocity (Orr, 2007). For the two-component problem, equations (5.1) and (5.2) reduce to a single quasilinear equation, which after the dimensionless transformations given in equations (4.25) and (4.26) becomes:

$$\frac{\partial}{\partial t_D}(w_{1c}\rho_c S_c + w_{1b}\rho_b S_b) + \frac{\partial}{\partial r_D}(w_{1c}\rho_c f_c + w_{1b}\rho_b f_b) = 0 \quad (5.3)$$

Defining functions C_1 and F_1 as:

$$C_1 = s_{1c}S_c + s_{1b}(1 - S_c) \quad (5.4)$$

$$F_1 = s_{1c}f_c + s_{1b}(1 - f_c) \quad (5.5)$$

where volume fractions of CO₂ and brine in the gas phase, respectively are:

$$s_{1c} = \frac{w_{1c}\rho_c}{\rho_1} \quad (5.6)$$

$$s_{1b} = \frac{w_{1b}\rho_b}{\rho_1} \quad (5.7)$$

and ρ_1 is the gas phase mass density without vaporised water, leads to the dimensionless form of the conservation equation for pure convection with no volume change on mixing:

$$\frac{\partial C_1}{\partial t_D} + \frac{\partial F_1}{\partial r_D} = 0 \quad (5.8)$$

5.2.1 Non-Darcy overall fractional flow function

Assuming that the CO₂ fractional flow is a function of saturation and distance from the well, values of f_c can be obtained following the procedure described in Chapter 4, section 4.2. When substituted into equation (5.5), these values determine the overall fractional flow of the gas phase within the two phase region (part 2 of the displacement in the schematic in Figure 5.1):

$$F_1 = s_{1c}f_c + s_{1b}(1 - f_c) \quad (5.9)$$

Two phase flow will occur when CO₂ compositions are within the range of $s_{1b} \leq C_1 \leq s_{1c}$.

Under Darcy flow conditions, for any mixture that forms a single phase, the overall fractional flow is equal to the composition of the phase (Orr, 2007):

$$F_1 = C_1 \quad (5.10)$$

This models the flow within the brine region ($C_1 < s_{1b}$), as the liquid phase does not experience the Forchheimer flow. However, if the gas phase is flowing under non-Darcy conditions, a correction of the wave velocity within the CO₂ zone ($C_1 > s_{1c}$) is needed.

Non-Darcy single-phase gas flow

Single-phase gas flux can be obtained from the mass conservation equation (4.18) with q_2 set to zero, which gives:

$$q_1 = \frac{Q}{2r\pi H} \quad (5.11)$$

Under linear conditions, this flux would be equal to the Darcy velocity, q_1^0 with $k_{r1} = 1$ (see equation (4.15)). When non-Darcy flow occurs, however, mobility of the gas will be reduced due to inertial effects. The extent of the reduction can be defined by the ratio of two fluxes (see equations (4.16) and (4.17)), such that:

$$\beta = \frac{q_1^0}{q_1} = 1 + B_1|q_1| \quad (5.12)$$

For the single-phase gas flow, expression for B_1 (see equation (4.14)) takes the form:

$$B_1 = \frac{b_1 \rho_1 k}{\mu_1} \quad (5.13)$$

with the Forchheimer coefficient b_1 defined from the Janicek and Katz (1955) formulation for a single-phase flow:

$$b_1 = \frac{W}{k^{1.25} \phi^{0.75}} \quad (5.14)$$

Having defined the Forchheimer factor, β in the single-phase gas region, it is now possible to define the overall fraction flow function when $s_{1c} < C_1 < 1$ (Figure 5.2):

$$F_1 = \frac{1}{\beta}(C_1 - s_{1c}) + s_{1c} \quad (5.15)$$

In the case of Darcy flow ($\beta = 1$), equation (5.15) reduces to the model of fractional flow within the brine region. Note that for non-Darcy flow ($\beta > 1$), the Forchheimer factor changes with the radial distance from the well. Therefore, overall fractional flow function within the gas region is spatially dependent.

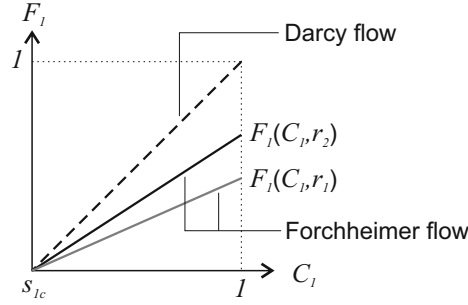


Figure 5.2: Overall fractional flow function within the single-phase gas region for spatially varying Forchheimer flow. Inertial effects increase with the proximity to the well ($r_w < r_1 < r_2$).

In summary, the overall fractional flow of the gas phase at any radial distance from the

well can be obtained from:

$$F_1 = \begin{cases} C_1, & 0 < C_1 < s_{1b} \\ S_c = 0 \\ s_{1c}f_c + s_{1b}(1 - f_c), & s_{1b} < C_1 < s_{1c} \\ 0 < S_c < 1 \\ \frac{1}{\beta}(C_1 - s_{1c}) + s_{1c}, & s_{1c} < C_1 < 1 \\ S_c = 1 \end{cases} \quad (5.16)$$

Note that in single-phase flow systems, fluid flux can be determined directly from the mass conservation equation (5.11), and hence the iterative procedure is not required.

5.2.2 Solution for composition by the MOC

The governing differential equation (5.8) has the same form as equation (4.27) derived for the non-Darcy immiscible displacement. In order to implement the solution by the MOC presented in Chapter 4 for the analysis of the miscible displacement, it is necessary to define the derivative $\partial F_1 / \partial C_1$.

Differentiation of equation (5.5) shows that (Orr, 2007):

$$\frac{\partial F_1}{\partial C_1} = \frac{\partial F_1}{\partial f_1} \frac{\partial f_1}{\partial C_1} = (s_{1c} - s_{1b}) \frac{\partial f_1}{\partial C_1} \quad (5.17)$$

where $\partial f_1 / \partial C_1$ can be obtained from equation (5.4):

$$\frac{\partial f_1}{\partial C_1} = \frac{\partial f_1}{\partial S_1} \frac{\partial S_1}{\partial C_1} = \frac{1}{(s_{1c} - s_{1b})} \frac{\partial f_1}{\partial S_1} \quad (5.18)$$

Combining equations (5.17) and (5.18) gives that $\partial F_1 / \partial C_1 = \partial f_1 / \partial S_1$. Thus, the gas compositions in the two-phase region can be obtained by implementing the initial condition (4.35) together with the revised form of equation (4.36), such that:

$$r_D = \int_0^{t_D} v(F_1, r_D) dt_D + r_{wD} = \int_0^{t_D} \left(\frac{\partial F_1}{\partial C_1} \right)_{r_D} dt_D + r_{wD} \quad (5.19)$$

where dimensionless radial distance, r_D and time, t_D are defined in equations (4.25) and (4.26), respectively. The solution within the two-phase region is a multivalued composition

profile at a fixed time, just as it is in the immiscible displacement problem. Hence, the transition into the single-phase liquid zone is defined by the leading shock front.

The existence of the upstream single-phase gas zone requires one more steep change in composition that is defined by the trailing shock. Equation (5.16) can be differentiated easily to obtain expressions for the wave velocity:

$$\left(\frac{\partial F_1}{\partial C_1}\right)_{r_D} = \begin{cases} 1, & 0 < C_1 < s_{1b} \\ S_c = 0 \\ \left(\frac{\partial f_c}{\partial S_c}\right)_{r_D}, & s_{1b} < C_1 < s_{1c} \\ 0 < S_c < 1 \\ \left(\frac{1}{\beta}\right)_{r_D}, & s_{1c} < C_1 < 1 \\ S_c = 1 \end{cases} \quad (5.20)$$

where the gas phase saturation, S_c , and composition, C_1 , are correlated by equation (5.4). Spatially varying values of $\partial F_1/\partial C_1$ define the resulting composition profile, shown in Figure 5.3 for both Darcy and non-Darcy displacements. Note that in non-Darcy miscible displacement, the wave velocity varies with the distance from the well in both gas and two-phase regions. The composition profile within these two regions has to be obtained from the numerical integration of equation (5.19).

Shock fronts at a fixed time can again be determined by implementing the equal area rule. Equating area A_1 with area A_2 gives an expression for the leading shock front, r_{LD} :

$$r_{LD} = \frac{1}{C_{1L}} \left[r_{bD} s_{1b} + \int_{C_{1c}}^{C_{1L}} r_D dC_1 \right] \quad (5.21)$$

while equating area A_3 with area A_4 defines the trailing shock front, r_{TD} under non-Darcy conditions:

$$r_{TD} = \frac{1}{1 - C_{1T}} \left[r_{cD}(1 - s_{1c}) + \int_{C_{1T}}^{1 - C_{2r}} r_D dC_1 \right] \quad (5.22)$$

where C_{1T} and C_{1L} are the trailing and leading shock front compositions, respectively, C_{1c} and C_{2r} are compositions corresponding to values of critical gas and residual brine saturations, respectively and r_{bD} and r_{cD} are single-phase radial extents of brine and CO_2 , respectively, obtained from equation (5.19). Derivation of expressions for shock fronts is

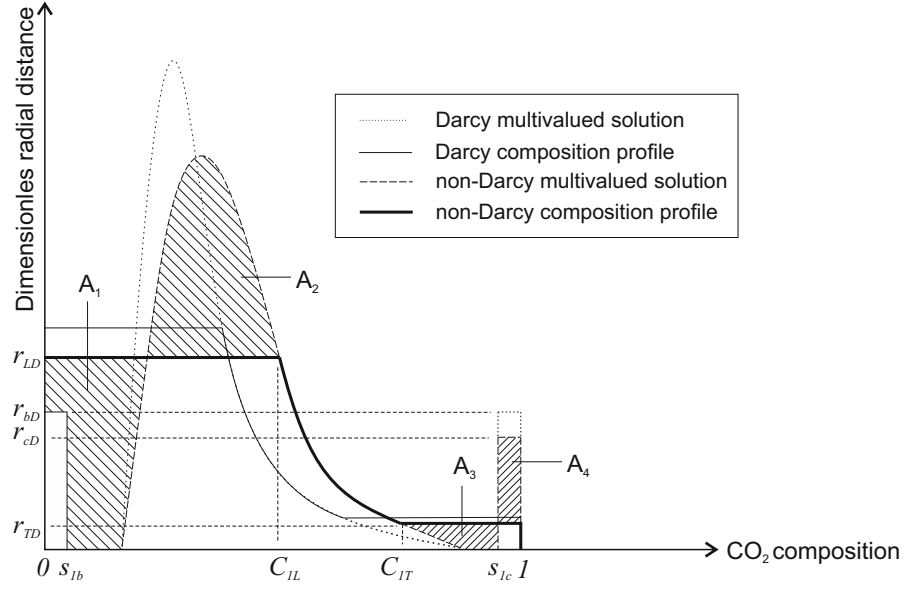


Figure 5.3: Equal area rule for miscible non-Darcy displacement.

explained in more detail in Appendix C. Numerical solutions of equations (5.21) and (5.22) define values of both front compositions and lateral extents of CO₂ and two-phase regions.

5.2.3 Solving for pressure

The solution for pressure in a miscible non-Darcy displacement can be obtained from the general expression for the pressure gradient defined by equation (4.38), which is modified to account for the contribution of the single-phase gas zone around the well and change of viscosities in the two-phase region due to phase miscibility:

$$\frac{dP}{dr_D} = -\frac{Q}{4\pi Hk} \begin{cases} \frac{1}{r_D} \left(\frac{1}{\beta} \frac{k_{rs}}{\mu_1} \right)^{-1}, & r_{wD} \leq r_D < r_{TD} \\ \frac{1}{r_D} \left(\frac{1}{\beta} \frac{k_{r1}}{\mu_c} + \frac{k_{r2}}{\mu_b} \right)^{-1}, & r_{TD} \leq r_D \leq r_{LD} \\ \frac{\mu_2}{r_D}, & r_D > r_{LD} \end{cases} \quad (5.23)$$

where k_{rs} is the permeability reduction factor due to salt precipitation, which will be discussed in more detail below, and μ_c and μ_b are viscosity of CO₂ and brine components,

respectively. Integration of equation (5.23) with respect to r_D gives:

$$P - P_0 = \frac{Q}{4\pi H k} \begin{cases} \mu_1 G_c(r_D) + \mu_c G_p(r_D) + \mu_2 G_b(r_D), & r_{wD} \leq r_D < r_{TD} \\ \mu_c G_p(r_D) + \mu_2 G_b(r_D), & r_{TD} \leq r_D \leq r_{LD} \\ \mu_2 G_b(r_D), & r_D > r_{LD} \end{cases} \quad (5.24)$$

where

$$G_c(r_D) = - \int_{r_D}^{r_{TD}} \frac{1}{r_D} \frac{\beta}{k_{rs}} dr_D \quad (5.25)$$

Two-phase integral function, $G_p(r_D)$ can be calculated using equation (4.41), with values of viscosity substituted to account for the phase mixing:

$$G_p(r_D) = - \frac{1}{\mu_c} \int_{r_D}^{r_{LD}} \frac{1}{r_D} \left(\frac{1}{\beta} \frac{k_{r1}}{\mu_c} + \frac{k_{r2}}{\mu_b} \right)^{-1} dr_D \quad (5.26)$$

Values of $G_b(r_D)$ can be obtained directly from expressions defined in Chapter 4 (see equations (4.44) and (4.50)). For open aquifers, the brine pressure integral takes the form:

$$G_b(r_D) = \begin{cases} E \left(\frac{Q\mu_2 c_2 r_D}{4\pi H k t_D} \right), & t_D < t_{cD} \\ \ln \left(\frac{1}{r_D} \right), & t_D \geq t_{cD} \end{cases} \quad (5.27)$$

while in closed systems it becomes:

$$G_b(r_D) = \begin{cases} E \left(\frac{Q\mu_2 c_2 r_D}{4\pi H k t_D} \right), & t_D < t_{cD} \\ \frac{4\pi H k t_D}{Q\mu_2 c_2} + \ln \left(\frac{1}{r_D} \right) - \frac{3}{2} + \frac{r_D - r_{LD}}{2}, & t_D \geq t_{cD} \end{cases} \quad (5.28)$$

Note that in miscible non-Darcy displacement, inertial effects will influence the pressure distribution within both gas and CO₂-brine regions.

5.2.4 Permeability reduction due to salt precipitation

Salt precipitation in the CO₂-brine system can be modelled by implementing the analytical solution presented in Zeidouni et al. (2009) and explained in more detail in Section 2.3.2. The model assumes that the salt precipitation occurs upstream of the trailing shock and

can be calculated as a function of the trailing shock saturation of the gas phase, S_{cT} :

$$S_s = \frac{\rho_2 w_{2s}(1 - S_{cT})}{\rho_s} \quad (5.29)$$

where S_s is volumetric saturation of precipitated salt, w_{2s} is the mass fraction of salt in liquid phase and ρ_s is salt mass density. Note that mass fractions in the liquid phase of the components considered are interrelated by $w_{2c} + w_{2b} + w_{2s} = 1$. Moreover, saturations are related, such that $S_c + S_b + S_s = 1$.

Having defined salt saturation, the change in the near-well permeability can be described by the permeability reduction factor defined by the Kozeny-Carman grain model (Bolton et al., 1999). The model estimates permeability reduction due to salt precipitation, k_{rs} based on the ratio of permeability, k_s to initial permeability, k given by (Zeidouni et al., 2009):

$$k_{rs} = \frac{k_s}{k} = \left(\frac{\phi_s}{\phi} \right)^3 \left(\frac{1 - \phi}{1 - \phi_s} \right)^2 \quad (5.30)$$

where ϕ is the initial formation porosity and ϕ_s is the porosity decreased due to salt precipitation defined as:

$$\phi_s = \phi(1 - S_s) \quad (5.31)$$

High values of S_s , which imply significant precipitation of the solid salt and reduction of the pore space available for the phase flow, will result in low values of the permeability reduction factor. Therefore, the higher the value of k_{rs} , the less pore space is affected by salt precipitation and the formation is more suitable for CO₂ injection. If permeability reduction due to salt precipitation is ignored, the value of k_{rs} converges to 1.

Although the model presented here is a simplified representation of the physical process, Pruess and Spycher (2007) showed that in the problem of radial miscible displacement with no volume change upon mixing, development of a spatially significant three-phase zone is not possible. The inner boundary of a potential brine-salt-gas region advances into the reservoir much faster than the precipitation front at the end of the zone that occurs when water evaporates across the trailing shock, making the three-phase zone self-sharpening and preventing it from developing further.

5.3 Model development

The improved non-Darcy solution, which can model two-phase miscible displacement and solid salt precipitation, was implemented to examine these effects on the aforementioned problem of CO₂ injection into a saline aquifer. The solution algorithm is shown in Figure 5.4. To obtain fractional flow curves, the miscible model requires two additional components compared to the immiscible solution: 1) calculation of mutual solubilities of water (H₂O) and CO₂ and 2) correction of fluid properties to account for phase mixing. This is discussed in more detail below.

5.3.1 Phase behaviour of CO₂-brine systems

In analyses of miscible CO₂-brine displacement, the partitioning of water and CO₂ between liquid and gas phases can be modelled as a function of temperature, pressure and salinity using the correlations given by Spycher et al. (2003) and Spycher and Pruess (2005). The first step in the process of calculating mutual solubilities of water and CO₂ is to obtain the activity coefficient, γ . In this study, the model of Rumpf et al. (1994) was used:

$$\gamma = \exp \left[2m_s \left(0.254 - \frac{76.82}{T} - \frac{10656}{T^2} + \frac{6312 \cdot 10^3}{T^3} \right) - 0.0084m_s^2 \right] \quad (5.32)$$

In equation (5.32) molality of salt, m_s is defined as:

$$m_s = \frac{1}{1 - w_{2s}} \frac{1000w_{2s}}{M_s} \quad (5.33)$$

where $M_s=58.448 \text{ g mol}^{-1}$ is the molar mass of sodium chloride salt (NaCl). The mass fraction of salt in the liquid phase, w_{2s} is equal to the brine salinity, K_s in g cm^{-3} . Note that in equation (5.32), temperature T is in Kelvins.

Fugacity coefficients, Φ , for CO₂ and water, can be obtained using the following expression (Spycher et al., 2003):

$$\Phi_c = \exp \left\{ \ln \left(\frac{V}{V - d_c} \right) + \left(\frac{d_c}{V - d_c} \right) - \left(\frac{2a_c}{RT^{1.5}d_c} \right) \ln \left(\frac{V + d_c}{V} \right) + \left(\frac{a_c d_c}{RT^{1.5}d_c^2} \right) \left[\ln \left(\frac{V + d_c}{V} \right) - \left(\frac{d_c}{V + d_c} \right) \right] - \ln \left(\frac{PV}{RT} \right) \right\} \quad (5.34)$$

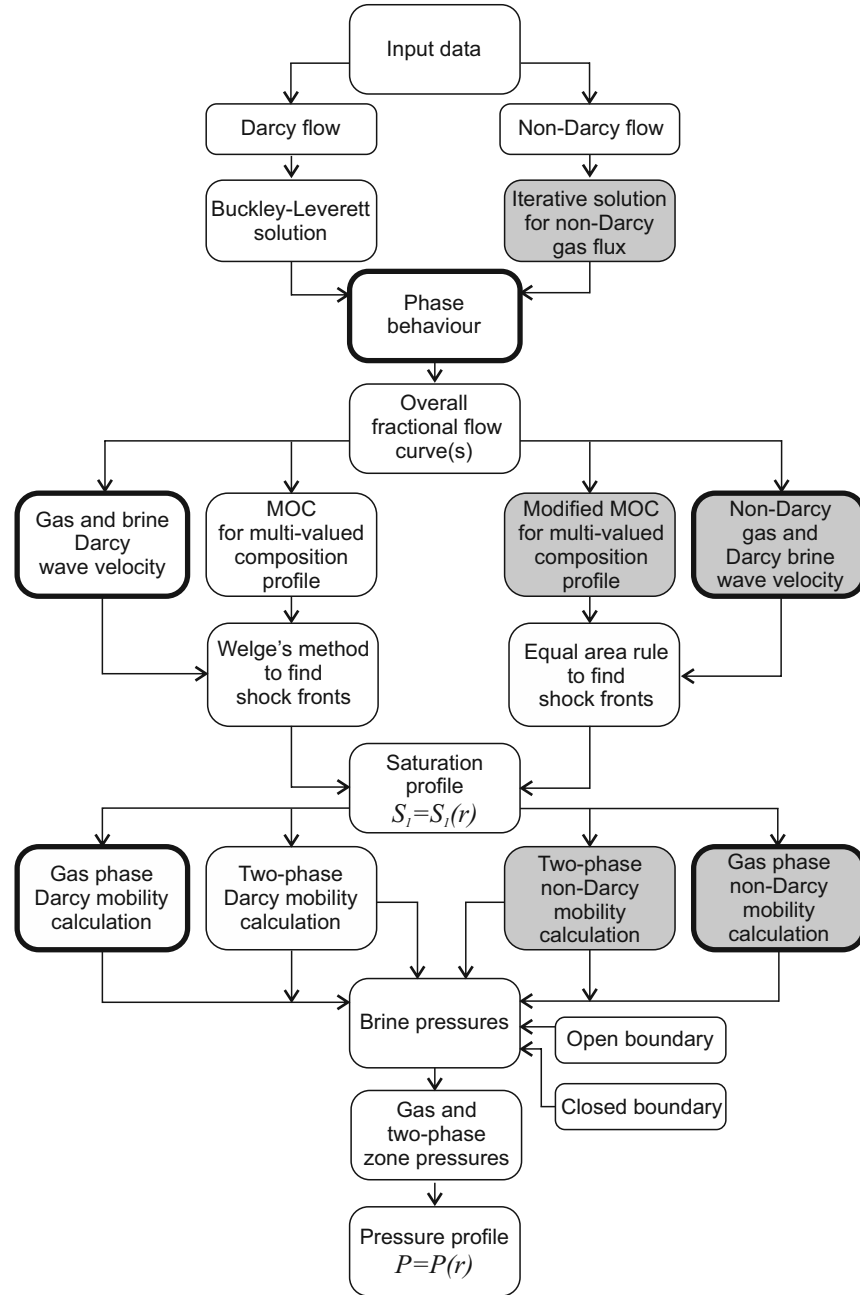


Figure 5.4: Solution algorithm for the two-phase Darcy and non-Darcy miscible displacements. Modules that implement novel approaches to the non-Darcy problem solution are additionally highlighted in grey. Model components added to the immiscible solution algorithm to account for the phase behaviour are highlighted with a thick black border.

$$\Phi_h = \exp \left\{ \ln \left(\frac{V}{V - d_c} \right) + \left(\frac{d_h}{V - d_c} \right) - \left(\frac{2a_{hc}}{RT^{1.5}d_c} \right) \ln \left(\frac{V + d_c}{V} \right) + \left(\frac{a_c d_h}{RT^{1.5}d_c^2} \right) \left[\ln \left(\frac{V + d_c}{V} \right) - \left(\frac{d_c}{V + d_c} \right) \right] - \ln \left(\frac{PV}{RT} \right) \right\} \quad (5.35)$$

where intermolecular attraction for CO₂, a_c is defined as in Chapter 4 (see equation (4.53)). Intermolecular repulsion for CO₂, d_c is a constant and equal to $d_c = 27.8 \text{ cm}^3 \text{ mol}^{-1}$. The procedure for calculating molar volume, V is detailed in section 4.3. In equation (5.35), the additional parameters are:

$$a_{hc} = 7.89 \cdot 10^7 \text{ bar cm}^6 \text{ K}^{0.5} \text{ mol}^{-2} \quad (5.36)$$

$$d_h = 18.8 \text{ cm}^3 \text{ mol}^{-1} \quad (5.37)$$

and the pressure P is in bars. Finally, equilibrium constants for components that form the two-phase mixture, Θ can be defined as a function of temperature T (in °C), such that:

$$\log(\Theta_c) = 1.189 + 1.304 \cdot 10^{-2}T - 5.446 \cdot 10^{-5}T^2 \quad (5.38)$$

$$\log(\Theta_h) = -2.209 + 3.097 \cdot 10^{-2}T - 1.098 \cdot 10^{-4}T^2 + 2.048 \cdot 10^{-7}T^3 \quad (5.39)$$

Having defined all the elements of a mutual solubility model for a CO₂-brine system, the water mole fraction in the gas phase, λ_{1h} can be obtained from (Spycher and Pruess, 2005):

$$\lambda_{1h} = \frac{(1 - \Gamma_c)55.508}{(1/\Gamma_h - \Gamma_c)(\nu m_s + 55.508) + \nu m_s} \quad (5.40)$$

where ν is the stoichiometric number of ions contained in the dissolved salt (equal to 2 for NaCl). Solubility parameters, Γ , for water and CO₂ respectively are:

$$\Gamma_h = \frac{\Theta_h}{\Phi_h P} \exp \left[\frac{(P - P_{atm})\bar{V}_h}{RT} \right] \quad (5.41)$$

$$\Gamma_c = \frac{\Phi_c P}{55.508 \gamma \Theta_c} \exp \left[-\frac{(P - P_{atm})\bar{V}_c}{RT} \right] \quad (5.42)$$

where $P_{atm}=1.01325$ bar is atmospheric pressure. Average volumes per mole of water and CO_2 are equal to $\bar{V}_h=32.6 \text{ cm}^3 \text{ mol}^{-1}$ and $\bar{V}_c=18.1 \text{ cm}^3 \text{ mol}^{-1}$, respectively (Table 2, Spycher and Pruess (2005)). Finally, the CO_2 mole fraction in the liquid phase, λ_{2c} is obtained from:

$$\lambda_{2c} = \Gamma_c(1 - \lambda_{1h}) \quad (5.43)$$

Once the mole fractions are determined using the solubility model, mass fractions can be calculated from (Pruess, 2005):

$$w_{2c} = \frac{m_c M_c}{1000 + m_s M_s + m_c M_c} \quad (5.44)$$

$$w_{2b} = 1 - w_{2c} - w_{2s} \quad (5.45)$$

$$w_{1b} = \frac{\lambda_{1h} M_c}{\lambda_{1h} M_h + (1 - \lambda_{1h}) M_c} \quad (5.46)$$

$$w_{1c} = 1 - w_{1b} \quad (5.47)$$

where $M_c=44.01 \text{ g mol}^{-1}$ and $M_h=18.02 \text{ g mol}^{-1}$ are the molar mass of CO_2 and water, respectively. The molality of the gas component, m_c can be obtained from:

$$m_c = \frac{\lambda_{2c}(2m_s + 1000/M_h)}{1 - \lambda_{2c}} \quad (5.48)$$

Table 5.1 shows mutual solubilities of water and CO_2 for a range of reservoir pressures considered in the present study. The difference between solubilities at limiting pressures, that is 10 and 60 MPa, is 0.1% for gas phase and 0.4% for liquid phase, indicating that compositional changes within the reservoir are insignificant.

5.3.2 Estimation of fluid properties for mixtures

For modest reservoir temperatures (i.e. $T \leq 100^\circ\text{C}$), the amount of water that is present in the gas phase is relatively insignificant (Pruess and Spycher, 2007). In this study, the properties of the gas phase within the two-phase region are therefore estimated using

Table 5.1: Mutual solubilities of CO₂ and water as a function of pressure at $T = 40^\circ\text{C}$ and brine salinity of 15 g cm^{-3} .

Pressure (MPa)	Mass fraction of			
	CO ₂ in gas phase (-)	water in gas phase (-)	CO ₂ in liquid phase (-)	water in liquid phase (-)
10	0.9984	0.0016	0.8395	0.0105
20	0.9977	0.0023	0.8382	0.0118
40	0.9974	0.0026	0.8365	0.0135
60	0.9974	0.0026	0.8352	0.0148

density and viscosity correlations presented in Chapter 4 (see equations (4.54) and (4.55)) for pure CO₂ without water present, that is $\rho_c = \rho_1$ and $\mu_c = \mu_1$.

Pruess and Spycher (2007) showed that dissolution of CO₂ in the liquid phase causes an increase in brine density. They suggested a correlation for the liquid phase density assuming the additivity of the volumes of brine and dissolved CO₂, such that:

$$\rho_b = \left(\frac{1 - w_{2c}}{\rho_2} + \frac{w_{2c}}{\rho_p} \right)^{-1} \quad (5.49)$$

where ρ_2 is brine density without dissolved CO₂ defined in equation (4.56) and ρ_p is the partial density of dissolved CO₂ obtained from (Pruess, 2005):

$$\rho_p = \frac{1000M_c}{37.51 - 9.585 \cdot 10^{-2}T + 8.74 \cdot 10^{-4}T^2 - 5.044 \cdot 10^{-7}T^3} \quad (5.50)$$

where T is in $^\circ\text{C}$. In this study, effects of dissolved CO₂ on brine viscosity are neglected, that is $\mu_b = \mu_2$, where liquid phase viscosity is given by equation (4.58).

5.4 Model results

The example of miscible CO₂ injection in saline aquifers presented here is based on the same initial and boundary conditions described in Table 4.5. Formation characteristics were set to a thickness of $H=200 \text{ m}$ and a permeability of $k=10^{-13} \text{ m}^2$. The gas was injected at a constant mass rate of $Q_m=100 \text{ kg s}^{-1}$. Two possible cases were analysed: 1) a reference case with brine salinity of 0.15 g cm^{-3} and 2) a higher salinity case with

$K_s=0.30 \text{ g cm}^{-3}$. The reduction of permeability due to salt precipitation was ignored, that is $k_{rs}=1$. Effects of phase mixing on CO_2 and brine viscosity were neglected (i.e. $\mu_c = \mu_1$ and $\mu_b = \mu_2$). The results of compositional calculations and fluid property estimations are presented in Table 5.2. A low percentage of brine evaporated into the flowing gas phase (less than 0.2% in both cases) justifies the assumption of water vapour having a negligible influence on the CO_2 phase density. Relative permeability values for the two-phase region correspond to those shown in Figure 4.13.

Table 5.2: Fluid properties and phase behaviour of CO_2 -brine system with initial conditions defined in Table 4.5.

Parameter	Reference case	Higher salinity
	value	case value
Salt concentration, K_s (g cm^{-3})	0.15	0.30
Gas phase density, $\rho_1 = \rho_c$ (kg m^{-3})	640	640
Pure brine density, ρ_2 (kg m^{-3})	1103	1223
Brine density with dissolved CO_2 , ρ_b (kg m^{-3})	1107	1224
Salt density, ρ_s (kg m^{-3})	2170	2170
Gas phase viscosity, $\mu_1 = \mu_c$ (Pa s)	$4.99 \cdot 10^{-5}$	$4.99 \cdot 10^{-5}$
Liquid phase viscosity, $\mu_2 = \mu_b$ (Pa s)	$8.91 \cdot 10^{-4}$	$13 \cdot 10^{-4}$
Liquid phase compressibility, c_2 (Pa^{-1})	$5 \cdot 10^{-10}$	$4 \cdot 10^{-10}$
Mass fractions of		
CO_2 in gas phase, w_{1c} (—)	0.9981	0.9983
brine in gas phase, w_{1b} (—)	0.0019	0.0017
CO_2 in liquid phase, w_{2c} (—)	0.0284	0.0160
brine in liquid phase, w_{2b} (—)	0.8216	0.6840
salt in liquid phase, w_{2s} (—)	0.1500	0.3000

5.4.1 Overall fractional flow function

Having determined the phase behaviour of the miscible CO_2 -brine system, it is possible to calculate the fractional flow functional dependance on CO_2 concentration for any radial distance from the well (Figure 5.5). Multiple fractional flow curves, characteristic for

the immiscible displacement, are replicated here, representing the behaviour of the system within the two-phase region. The brine region corresponds to the zone of low CO_2 concentrations, with the linear change of fractional flow with respect to CO_2 composition and constant characteristic velocity.

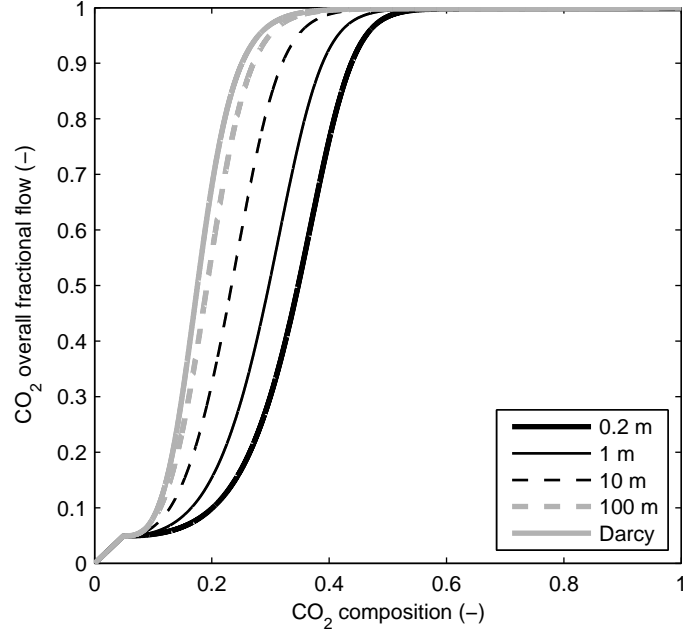


Figure 5.5: Non-Darcy overall fractional flow curves as a function of gas phase composition and radial distance from the well for $Q_m=100 \text{ kg s}^{-1}$, $W=3.2 \cdot 10^{-7} \text{ m}^{1.5}$ and $K_s=0.15 \text{ g cm}^{-3}$.

The overall fractional flow function that represents the near-well region containing pure CO_2 is shown in Figure 5.6. In contrast to the brine region, the gas phase characteristic velocity is influenced by inertial effects, represented by the slope of the overall fractional flow function, that is by the value of β (see equation 5.15). Compared to the fluid flux approaching Darcy flow conditions at 100 m from the well ($\beta=1.1$), the influence of non-Darcy effects at the well ($r=r_w=0.2 \text{ m}$) could be as high as 90% reduction of gas flux compared to Darcy flow ($\beta=61.7$). Although constant with respect to CO_2 composition, gas phase flow in the CO_2 region is spatially varying, following the same pattern as in the two-phase zone. Consequently, saturation and pressure profiles will be altered, compared to those obtained with the Darcy model.

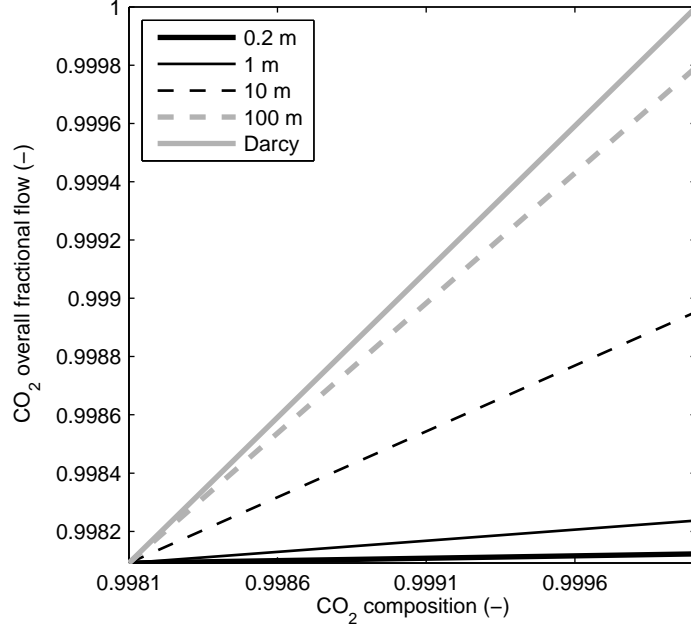


Figure 5.6: Spatially varying non-Darcy overall fractional flow in near-well CO₂ region as a function of gas phase composition for $Q_m=100 \text{ kg s}^{-1}$, $W=3.2 \cdot 10^{-7} \text{ m}^{1.5}$ and $K_s=0.15 \text{ g cm}^{-3}$.

Model with constant Forchheimer coefficient

Results presented in the previous section account for the change of the Forchheimer coefficient, b_1 with respect to phase saturation. However, the model can be simplified to calculate the Forchheimer coefficient independently of phase saturations and relative permeability, that is to use equation (5.14) for both CO₂ and two-phase regions:

$$b_1 = \frac{W}{k^{1.25} \phi^{0.75}} \quad (5.51)$$

This modification in the analytical model enables comparison of results with reservoir simulator estimations, which will be discussed in more detail below. Furthermore, it allows evaluation of effects of variable non-Darcy displacement on saturation and pressure profiles and the formation of the dry-out region during CO₂ injection. Figure 5.7 shows overall fractional flow curves for the model with the constant value of $b_1 = 1.903 \cdot 10^{10} \text{ m}^{-1}$. Non-Darcy effects are reduced significantly compared to the case with the variable Forchheimer coefficient (see Figure 5.5). The Forchheimer flow is limited to a very narrow area around the well ($r \leq 1 \text{ m}$, approximately).

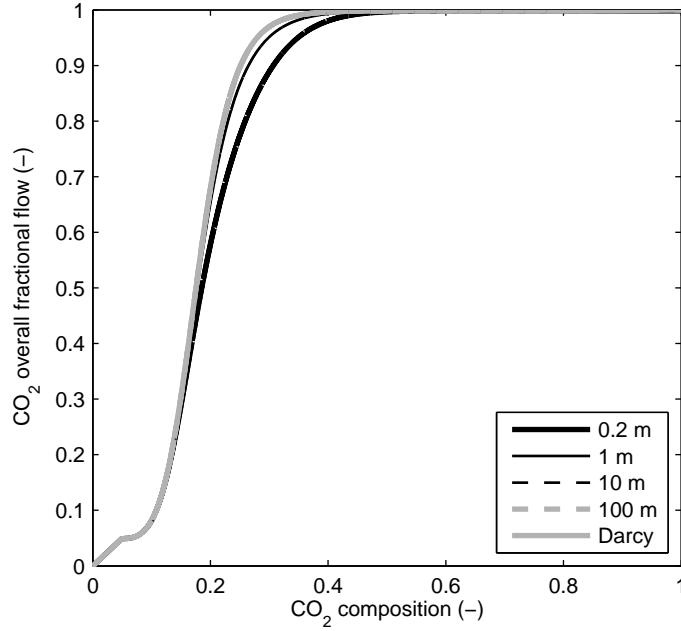


Figure 5.7: Non-Darcy overall fractional flow curves as a function of gas phase composition and radial distance from the well in the model with constant Forchheimer coefficient, b_1 . Parameters are set to $Q_m=100 \text{ kg s}^{-1}$, $W=3.2 \cdot 10^{-7} \text{ m}^{1.5}$ and $K_s=0.15 \text{ g cm}^{-3}$.

5.4.2 Saturation and pressure distributions

Compared to the immiscible displacement results, the saturation profiles show the same behaviour within the two-phase and brine regions (Figure 5.8a). In the case of the miscible displacement, a dry-out zone around the well is formed. The location of the trailing evaporation shock varies insignificantly with respect to flow conditions considered (Table 5.3). There is, however, a significant difference between saturation distributions under constant and variable non-Darcy flow conditions. Assuming a constant value of b_1 can lead to an underestimation of the displacement efficiency of non-Darcy CO_2 -brine systems.

Figure 5.8b shows the decline in reservoir pressures within the CO_2 region (for numerical values see Table 5.3). In non-Darcy displacement with variable b_1 , pressure at the well was reduced by 10% compared to the immiscible case. This is due to the increase of the CO_2 relative permeability that occurs once all the brine is evaporated into the flowing gas phase. Again there is evident discrepancy between the two non-Darcy solutions. The more efficient displacement with variable b_1 comes at a cost of a significant pressure buildup within the two-phase region.

The results in Table 5.3 show that salinity increase does not affect significantly the

Table 5.3: Simulation results for miscible Darcy ($W=0$) and non-Darcy ($W=3.2 \cdot 10^{-7} \text{ m}^{1.5}$) flow and reference and higher salinity cases five days since the beginning of injection. Subscripts L and T denote values of the parameter at the leading and trailing shock fronts, respectively. Results for immiscible displacement from Table 4.7, case b are repeated for comparison.

Parameter	$K_s=0.15 \text{ g cm}^{-3}$					$K_s=0.30 \text{ g cm}^{-3}$		
	Darcy		Non-Darcy			Darcy		Non-Darcy
	imm.*	misc.	imm.var. b_1	misc.con. b_1	misc.var. b_1		con. b_1	var. b_1
$S_{1T}(-)$	–	0.4673	–	0.4924	0.5361	0.4604	0.4891	0.5282
$r_T(\text{m})$	–	1.48	–	1.46	1.44	1.37	1.35	1.33
$S_{1L}(-)$	0.1845	0.1845	0.2095	0.1940	0.2191	0.1691	0.1778	0.2008
$r_L(\text{m})$	48.4	48.4	45.8	48.2	42.3	50.2	49.9	42.8
$P_w(\text{MPa})$	18.4	18.1	22.2	19.0	20.2	19.9	20.9	22.2
$S_s(-)$	–	0.0406	–	0.0387	0.0354	0.0912	0.0864	0.0798
$k_{rs}(-)$	–	0.866	–	0.872	0.882	0.718	0.730	0.748

*imm. = immiscible, misc. = miscible, con. = constant, var. = variable

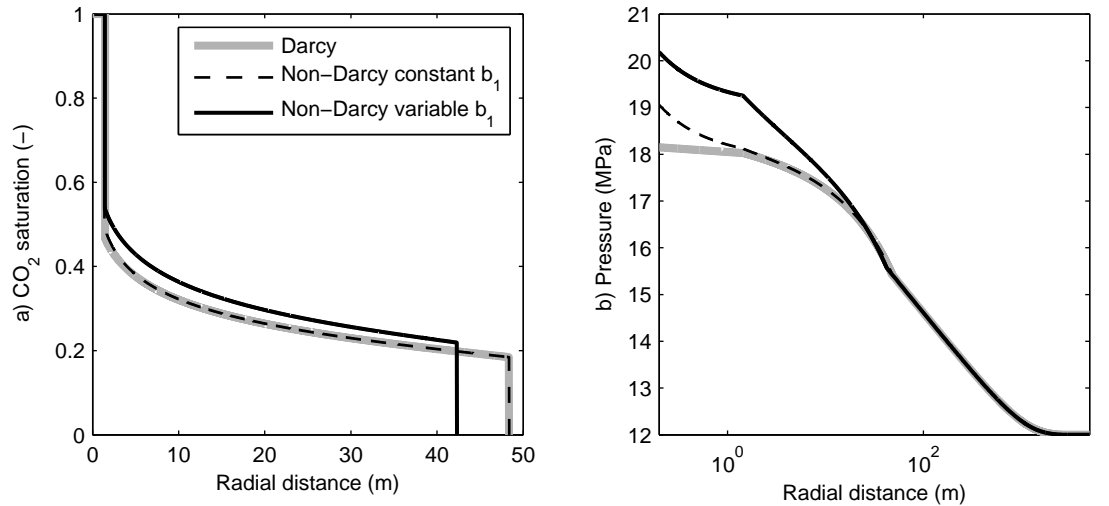


Figure 5.8: Effects of the Forchheimer coefficient variability on: a) CO₂ saturation and b) pressure distributions five days after the beginning of injection for $Q_m=100 \text{ kg s}^{-1}$, $W=3.2 \cdot 10^{-7} \text{ m}^{1.5}$ and $K_s=0.15 \text{ g cm}^{-3}$.

saturation distribution. However, the corresponding well pressures differ considerably. This is confirmed by results for Darcy displacement showed in Figure 5.9. The reason is that higher salt concentration increases brine density and viscosity (see Table 5.2). Hence, flow resistance is higher in higher salinity brines. The main cause of the increased well pressure in higher salinity case is additional pressure buildup within the single-phase liquid zone. The Forchheimer flow will follow the same pattern as this effect is due to the change in brine properties only.

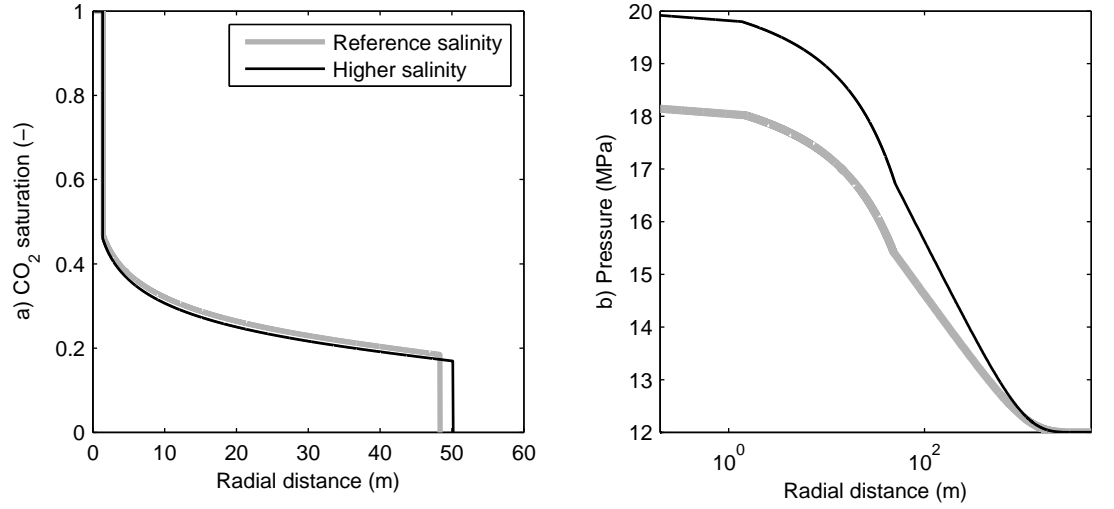


Figure 5.9: Effects of brine salinity in Darcy displacement on: a) CO₂ saturation and b) pressure distributions five days after the beginning of injection for $Q_m=100 \text{ kg s}^{-1}$. Reference salinity case is for $K_s=0.15 \text{ g cm}^{-3}$ and higher salinity for $K_s=0.30 \text{ g cm}^{-3}$.

5.4.3 Permeability reduction

Effects of the non-Darcy flow on near-well permeability were analysed for two of the brine salinity cases selected. The results are shown in Figure 5.10. During the initial injection stage ($t \leq 50$ days), the decrease in the wave velocity within the single-phase gas region due to inertial effects showed to be insignificant, which may indicate the negligible influence of non-Darcy effects on the single-phase flow mobility. Hence, the development of the dry-out front is not affected by the Forchheimer flow in the examples presented here (subfigures 5.10a and 5.10d).

The non-Darcy effects within the two-phase region, however, are more significant be-

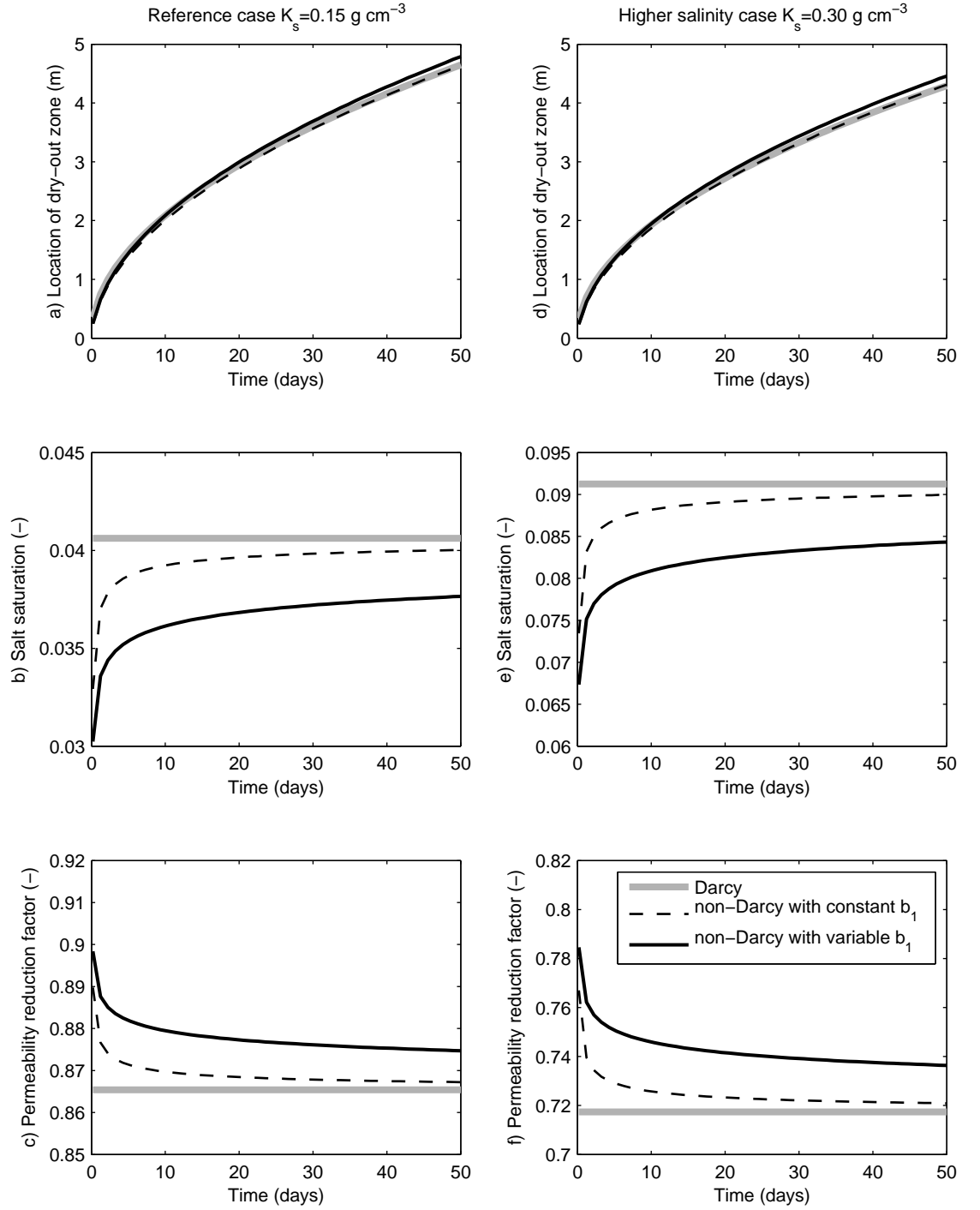


Figure 5.10: Effects of the Forchheimer coefficient variability on permeability reduction parameters for: a)–c) reference case with $K_s=0.15 \text{ g cm}^{-3}$ and d)–f) higher salinity case with $K_s=0.30 \text{ g cm}^{-3}$. The injection rate is $Q_m=100 \text{ kg s}^{-1}$ and the Forchheimer flow constant is $W=3.2 \cdot 10^{-7} \text{ m}^{1.5}$.

cause of reduced gas permeability due to the liquid phase flow. This increases the shock saturation at the trailing front compared to Darcy flow conditions, and delays the time to the breakthrough. Salt saturation, and consequently near-well permeability, are significantly altered. Up to 25% less salt may precipitate in non-Darcy flow. Compared to constant salt precipitation under Darcy conditions, which is related to the constant value of the trailing front saturation, the non-Darcy model predicts low initial solid saturations (subfigures 5.10b and 5.10e). This implies less permeability reduction under non-Darcy conditions (subfigures 5.10c and 5.10f). Higher formation permeability under non-Darcy flow conditions during early injection times is particularly important because of the substantial initial pressure buildup at the well. Non-Darcy flow is even more favourable for the CO₂ injection processes if b_1 varies with respect to saturation. Note that values of k_r indicate the percentage of pore space that is not affected by salt precipitation.

An increase in brine salinity was shown to have a negligible effect on development of the dry-out zone compared to the reference case. Values of salt saturation, however, are increased in proportion to the increment of brine salinity (Table 5.3). Consequently, permeability reduction increases as well. Compared to approximately 12% of initial porosity being reduced due to salt precipitation in the reference salinity case, this value for the higher salinity brine can be as high as 28%. This is likely to cause additional pressure buildup at the well, which is not addressed in pressure calculations in this study due to ignoring the effects of salt precipitation on the change of permeability within the dry-out zone. This issue, however, would need to be explored further.

5.4.4 Comparison with reservoir simulator

The analytical solution for the miscible non-Darcy displacement is valid under the assumptions made for its derivation, which include vertical pressure equilibrium, negligible capillary pressure, incompressible fluids and Forchheimer flow of the gas phase. To test the validity of the non-Darcy compositional model proposed here, its results were compared to those from the reservoir simulator ECLIPSE 300 (Schlumberger, 2002).

The simulation model was set up for a fully penetrating well, located in the centre of a circular domain with a radial grid. The CO2STORE option was used for the modelling of CO₂ injection in saline aquifers, which uses the same equation of state implemented in this study. To ensure the accuracy of the model in the near-well region, the radial extent of 5 km was divided into sub-domains (Mathias et al., 2011b). The near-well zone was set at 10 m from the well and discretised into 1000 equally spaced nodes. Three intermediate

zone boundaries were located at 50, 500 and 2000 metres from the well, each containing 500 nodes. Finally, the outer zone of 3000 m was divided into 250 nodes. Mathias et al. (2011b) showed that for the conditions relevant to CO₂ storage, gravity has a negligible influence on vertically averaged pressures. The numerical simulations were performed with just one vertical layer that is equal to the thickness of the aquifer. The top of the layer was assumed to be located at 1000 m below the ground surface. The mean initial pressure of 12 MPa was invoked by setting the hydrostatic equilibrium datum in the centre of vertical domain, at a depth of 1100 m.

When the aquifer is assumed to be infinite in extent, the boundary condition at the outer boundary of the model should represent the initial pressure distribution. In the simulation model, the constant pressure condition was implemented by modifying the grid so that the outermost grid block pore volume was multiplied by a factor of 10^{10} . The CO₂ injection boundary condition was controlled using a constant surface volumetric injection rate, which corresponds to the mass injection rate used in the analytical model simulations.

A three-component (CO₂, H₂O and NaCl) system was analysed, with the SOLID option activated to allow for salt to be present in both liquid and solid phases. The Rumpf et al. (1994) model was selected for the calculation of activity coefficients. The same relative permeability functions were used as in the analytical solution (see Figure 4.13). The capillary pressure, P_C was calculated using the van Genuchten (1980) relationship:

$$P_C = P_{C0} \left[(\bar{S})^{-\frac{1}{p}} - 1 \right]^{1-p} \quad (5.52)$$

where P_{C0} is a reference capillary pressure and p is the van Genuchten capillary model parameter. The effective brine saturation, \bar{S} is defined in equation (4.64). The capillary pressure–saturation relationship obtained is shown in Figure 5.11, and values of P_{C0} and p are given in Table 5.4.

In the reservoir simulator, non-Darcy flow can be modelled using the Forchheimer equation with a constant value of the coefficient b_1 . It is only possible to include porosity and saturation dependency of b_1 by modelling velocity dependent relative permeability. In that case, however, the near-well effects are taken into account through the rate-dependent skin factor. The results cannot be compared directly to those of the Forchheimer analytical solution, because skin effect is defined only in the computational cell where the well is located. This approach is not adequate for modelling gas phase flow, as the non-Darcy behaviour is likely to appear in an extended region around the well. To enable a compar-

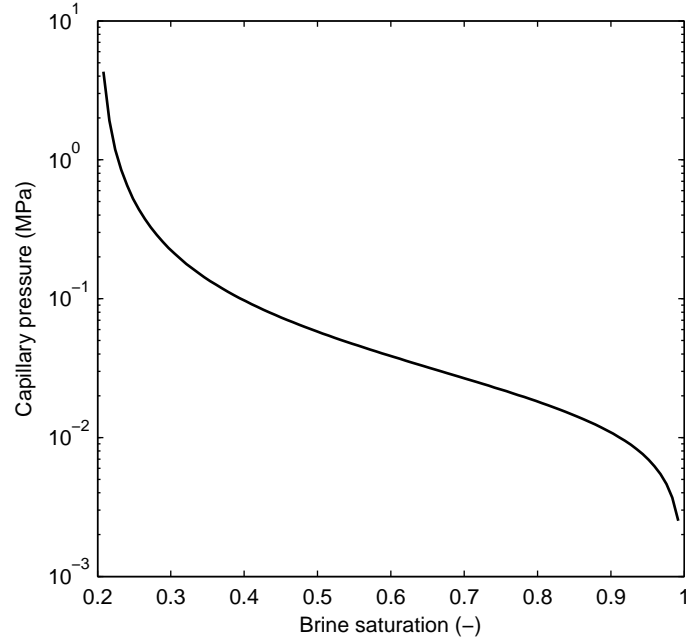


Figure 5.11: The simulation model capillary pressure function obtained using the van Genuchten (1980) model. Input parameters are given in Table 5.4.

ison of solutions, the analytical model results were obtained using equation (5.51) for the constant Forchheimer coefficient in both CO_2 and two-phase regions. The values of the parameters used in the reservoir simulator are given in Table 5.4. Note that the value of b_1 set in the simulation model corresponds to a value of the Forchheimer flow constant of $3.2 \cdot 10^{-7} \text{ m}^{1.5}$, which was used in analytical model calculations.

Table 5.4: Model parameters used in the reservoir simulator. Corresponding initial and boundary conditions are given in Table 4.5.

Parameter	Value
Surface injection rate, Q ($\text{m}^3 \text{ day}^{-1}$)	$4.6 \cdot 10^6$
Rock compressibility, c_r (Pa^{-1})	$4.5 \cdot 10^{-10}$
Reference capillary pressure, P_{C0} (Pa)	19600
van Genuchten capillary model parameter, p ($-$)	0.46
Forchheimer parameter for the gas phase, b_1 (cm^{-1})	$1.9 \cdot 10^8$

Figure 5.12 compares the gas saturation and pressure profiles obtained from the reservoir simulator and the non-Darcy analytical solution with the constant Forchheimer coefficient. The analytical model accurately predicts the CO₂ saturation distribution in the vicinity of the well and the location of the dry-out front. Moreover, the change in the phase saturation within the two-phase zone is estimated correctly. However, due to the assumption of constant CO₂ properties based on the initial pressure, as well as incompressible and viscous-dominated displacement, the analytical solution does not account for the change in the gas phase mobility that occurs in the compressible displacement. Therefore, the location of the leading shock front is somewhat overestimated, especially for later times.

The analytical solution pressures capture accurately the distribution obtained from the simulator results (Figure 5.12b). However, the reservoir pressure is consistently overestimated in the analytical solution. This is again due to an assumption of the incompressible displacement. Using a constant CO₂ density based on the initial pressure does not account for the reduction of the gas volumetric injection rate once the pressures within the reservoir increase after the beginning of the injection.

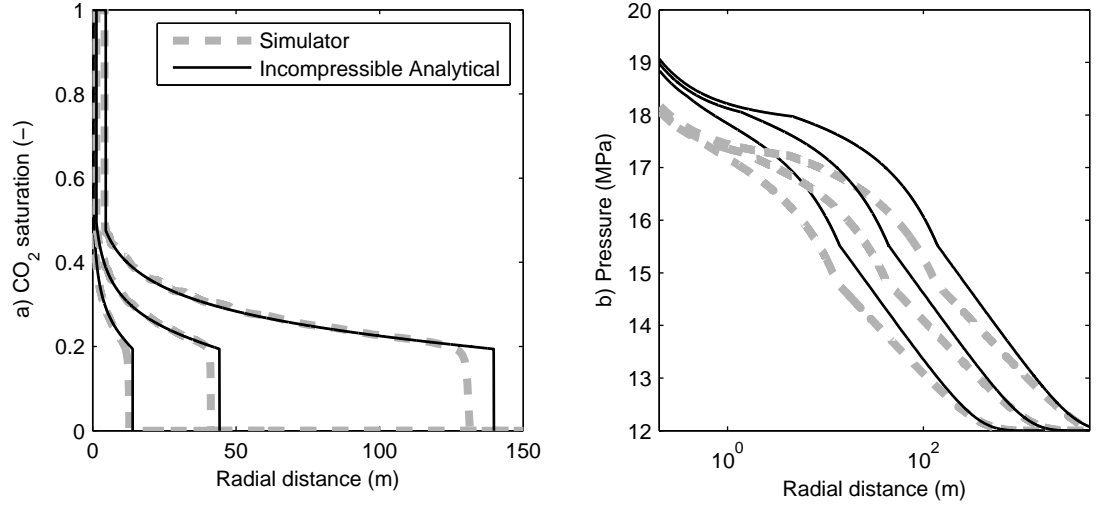


Figure 5.12: Comparison of: a) CO₂ saturation and b) pressure distributions for the reference case (i.e. $K_s=0.15 \text{ g cm}^{-3}$) during the early injection period ($t=0.5, 5$ and 50 days). The injection rate is $Q_m=100 \text{ kg s}^{-1}$ and the Forchheimer flow constant for non-Darcy flow is $W=3.2 \cdot 10^{-7} \text{ m}^{1.5}$. The Forchheimer coefficient, b_1 is assumed to be independent of the gas phase saturation for the purpose of benchmarking.

Although reservoir pressures cannot be estimated accurately, Figure 5.13 shows that the incompressible analytical solution performs well against the reservoir simulator within the near-well region, and gives a safety margin for pressure estimations. The radial extent of the dry-out zone, which defines the region of reduced permeability, shows excellent agreement with the numerical data during early injection times ($t \leq 10$ days, Figure 5.13a). The analytical model, however, overestimates slightly the extent of the dry-out front during later times. This may be due to effects of compressibility on reducing the gas mobility that were not captured by the analytical model. The analytical model also overestimates the solid salt saturation (Figure 5.13b), with the deviation from the S_s values produced by the reservoir simulator up to 10%. Note that the salt precipitation model cannot capture the initial increase of the salt saturation due to the water imbibition in the close proximity of the well. Nevertheless, the incompressible compositional analytical solution can be applied for the preliminary analysis of the near-well permeability reduction under non-Darcy conditions.

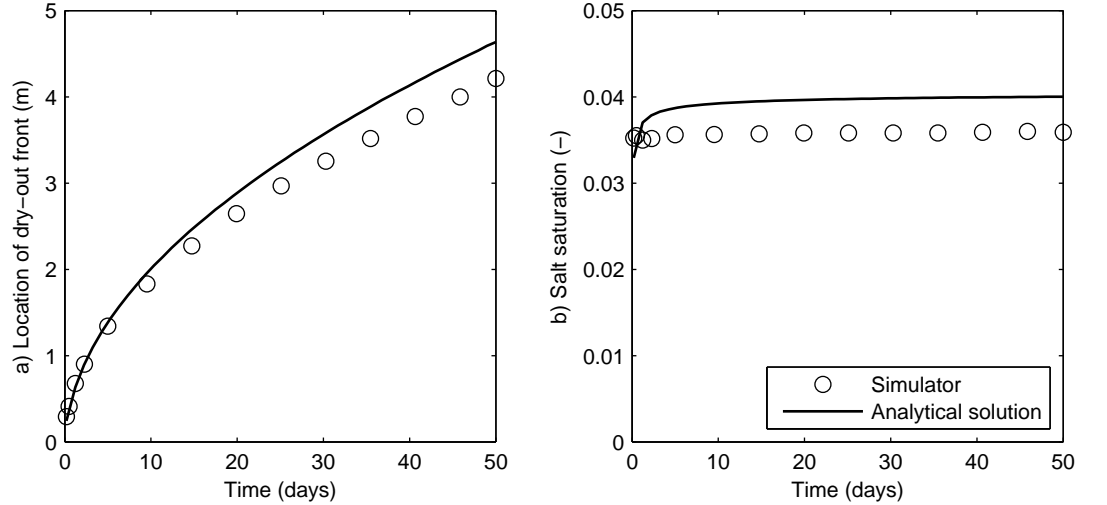


Figure 5.13: Comparison of: a) development of the dry-out front and b) salt saturation for the reference case (i.e. $K_s=0.15 \text{ g cm}^{-3}$) during early injection period ($t \leq 50$ days). The injection rate is $Q_m=100 \text{ kg s}^{-1}$ and the Forchheimer flow constant for non-Darcy flow is $W=3.2 \cdot 10^{-7} \text{ m}^{1.5}$. The Forchheimer coefficient, b_1 is assumed to be independent of the gas phase saturation for the purpose of benchmarking.

5.5 Conclusions

In order to adequately estimate the CO₂ storage capacity, it is necessary to determine all the factors that may influence the injection process. One of the most important is the salt precipitation in the near-well region, which may decrease the injectivity and give rise to an additional pressure buildup by decreasing the aquifer permeability. Conversely, the evaporation of brine gives lower pressure buildup in the gas phase region because loss of the residual water allows for higher CO₂ permeability. This chapter has investigated the effects of non-Darcy flow on the development of the dry-out zone, which in turn directly influences the salt precipitation pattern. Solid salt saturation was assumed to be a function of the liquid phase saturation immediately downstream of the trailing shock front.

The analysis of the influence of non-Darcy flow on miscible displacement showed that the trailing shock, which defines the boundary between the dry-out and two-phase zones, had a lower water saturation downstream than the corresponding Darcy and constant Forchheimer shock fronts (Figure 5.8a). Reduced amount of evaporated brine led to a lower salt saturation under variable non-Darcy conditions (Figure 5.10). Consequently, the permeability reduction in the near-well region was reduced, especially during early times when the most significant pressure buildup under non-Darcy conditions occurs.

An increase in brine salinity was shown to have a negligible effect on development of the dry-out front. However, in the case of high-salinity brine, additional pressure increase within the single-phase liquid zone has had an influence on the whole pressure profile (Figure 5.9). Furthermore, the process of salt precipitation was shown to reduce significantly the near-well permeability. This could have important implications for pressure buildup at the well, which needs to be explored further.

Validation of the compositional non-Darcy model was performed by comparing the simulation results to those from the reservoir simulator ECLIPSE 300. To enable the direct comparison of results, the analytical solution was modified to simulate the non-Darcy two-phase flow with a constant value of the Forchheimer coefficient, b_1 . Analysis of saturation and pressure profiles (Figure 5.12) showed that the incompressible model failed to predict accurately the radial extent of the leading shock front. Moreover, it significantly overestimated the reservoir pressures. Both of these may be addressed by adding compressibility into the analytical solutions, which will be done in the next chapter. The analytical solution, however, performed well in the near-well region, where it accurately modelled the development of the dry-out front, especially during initial stages of injection

(Figure 5.13a). The analytical solution applied for modelling salt saturation also gave accurate predictions. The estimations diverged from the reservoir simulator results no more than 10%.

Compositional analyses of CO₂ injection problems are necessary to take into account the process of salt precipitation, which may significantly change the pressure distribution within the aquifer. In this chapter it was shown that under non-Darcy flow, these effects are even more significant and favourable to the CO₂ injection process with respect to the smaller loss of permeability due to salt precipitation. The incompressible analytical non-Darcy model gave accurate predictions of the location of the permeability-reduced zone and slightly higher estimations of salt saturation. However, results can be applied for the preliminary analysis of the potential CO₂ storage sites.

Although the solution presented in this chapter improved the immiscible solution from Chapter 4, its application is still limited by the assumptions of a homogeneous formation and incompressible flow. Furthermore, it is assumed that the viscous forces dominate the displacement process and that capillary pressure is negligible. A better applicability of the non-Darcy model can be achieved if the effects of compressibility are included. In addition, the analytical solution can be improved to model the decrease in mobility as a function of salt saturation, which would enable more accurate analyses of the influence of permeability reduction on the pressure distribution.

Chapter 6

Effects of CO₂ compressibility

6.1 Introduction

In Chapter 4 it was shown that CO₂ properties vary significantly as the pressure in the reservoir increases, making the assumption of gas incompressibility physically unrealistic. Furthermore, comparison of results between the compositional analytical solution and reservoir simulator in Chapter 5 showed that by neglecting the compressibility of CO₂, gas plume lateral extent and near-well reservoir pressures can be overestimated significantly.

The change in CO₂ properties affects both saturation and pressure solutions. Under Darcy flow conditions, variable gas viscosity will change CO₂ mobility, while the density of the compressed gas will influence the volumetric flow in the reservoir. In non-Darcy two-phase flow, however, the system becomes more complex:

- Pressure buildup during CO₂ injection increases CO₂ viscosity and therefore directly affects the mobility of the gas phase (see equation (4.24)). Under non-Darcy flow, increased gas viscosity also reduces the value of the Forchheimer flow parameter, B_1 (see equation (4.14)).
- Increasing the CO₂ density decreases the gas phase volume and hence decreases the volumetric injection rate (see equation (4.76)). In Darcy displacements, fractional flow function is independent of the injection rate and therefore the influence of the compressibility is limited only to the aforementioned viscosity-induced changes. Non-Darcy fractional flow will, however, change with the reduction in the volumetric injection rate due to its influence on the pressure distribution, which in turn determines the spatially variable gas phase velocity (see iterative procedure for determination of the non-Darcy gas phase velocity presented in section 4.2). In addition, higher gas

density will affect the value of the parameter B_1 in both CO_2 and two-phase regions.

This chapter extends the compositional non-Darcy model, presented in Chapter 5, to explore effects of CO_2 compressibility on non-Darcy two-phase flow. A correction to account for CO_2 compressibility by varying the gas density and viscosity is applied by modifying the approach presented by Vilarrasa et al. (2010). The new model includes the change of the fluid flux with respect to gas compressibility. The reservoir simulator ECLIPSE 300 (Schlumberger, 2002) was used as a benchmark for verifying the analytical model with non-variable inertial effects, that is when the Forchheimer coefficient is assumed to be independent of the gas phase saturation. Finally, the importance of considering CO_2 compressibility and non-Darcy effects in analysis of CO_2 injection problems was discussed.

6.2 Compressible two-phase flow

The mass conservation equations that describe incompressible, immiscible and radial two-phase flow in a homogeneous, confined aquifer were derived in Chapter 4 (see equations (4.3) and (4.4)). Assuming the gas compressibility ($c_1 = -\frac{1}{V} \frac{dV}{dP}$), the system of governing equations becomes:

$$\frac{\partial(S_1\rho_1)}{\partial t} + \frac{1}{\phi} \left[\frac{\rho_1 q_1}{r} + \frac{\partial(\rho_1 q_1)}{\partial r} \right] = 0 \quad (6.1)$$

$$\frac{\partial S_2}{\partial t} + \frac{1}{\phi} \left[\frac{q_2}{r} + \frac{\partial q_2}{\partial r} \right] = 0 \quad (6.2)$$

These two-phase flow governing equations can be transformed by applying the self-similar function (Bedrikovetsky, 1993) :

$$q = \frac{U(\xi)}{\sqrt{2t}} \quad (6.3)$$

$$\xi = \frac{r}{\sqrt{2t}} \quad (6.4)$$

where U is scaled fluid flux and ξ is the self-similar transformation function. By applying the fractional flow theory and the self-similar transformations (6.3) and (6.4), the system

(6.1)-(6.2) reduces to the system of ordinary differential equations:

$$-\xi \frac{d(S_1 \rho_1)}{d\xi} + \frac{1}{\phi} \left[\frac{\rho_1 f_1 U}{\xi} + \frac{d}{d\xi} (\rho_1 f_1 U) \right] = 0 \quad (6.5)$$

$$\xi \frac{dS_1}{d\xi} + \frac{1}{\phi} \left[\frac{(1-f_1)U}{\xi} + \frac{d}{d\xi} [(1-f_1)U] \right] = 0 \quad (6.6)$$

Substitution of the total derivative $dS_1/d\xi$ from equation (6.6) into the equation (6.5) gives the expression for the change of the fluid flux in a compressible displacement:

$$\frac{dU}{d\xi} = \frac{\phi}{\rho_1} \frac{d\rho_1}{d\xi} \left(\xi S_1 - \frac{f_1 U}{\phi} \right) - \frac{U}{\xi} \quad (6.7)$$

The two-phase compressible displacement can therefore be described by the system of equations (6.6) and (6.7), which after reverting into the original notation become:

$$\frac{\partial S_1}{\partial t} + \frac{q}{\phi} \frac{\partial f_1}{\partial r} - \frac{1}{\phi} \left[(1-f_1) \frac{q}{r} + (1-f_1) \frac{\partial q}{r} \right] = 0 \quad (6.8)$$

$$\frac{dq}{dr} = \phi \frac{1}{\rho_1} \frac{d\rho_1}{dP} \frac{dP}{dr} \left(\frac{r S_1}{2t} - \frac{f_1 q}{\phi} \right) - \frac{q}{r} \quad (6.9)$$

The details of the derivation of governing equations for a compressible two-phase displacement are given in Appendix D. Note that if the gas phase is assumed to be incompressible, that is $d\rho_1/dP = 0$, equation (6.9) reverts to equation (4.6), and the governing mass conservation equation (6.8) corresponds to the one derived for immiscible and incompressible flow (see equation (4.8)).

The system (6.8)-(6.9) cannot be solved analytically. However, if the problem is treated as an incompressible displacement where effects of compressibility are taken into account by correcting the reference pressure used to determine the fluid properties and volumetric injection rate, the solution can be found by implementing an iterative procedure (Vilarrasa et al., 2010).

6.2.1 Compressibility correction

The compressible flow problem is highly nonlinear, because fluid properties and reservoir pressures are mutually correlated. One possible solution to the problem is an iterative procedure, as proposed by Vilarrasa et al. (2010). In that study, it was assumed that a

compressible two-phase displacement can be approximated with an incompressible solution in which CO₂ properties are calculated at some reference pressure. If the CO₂ density that corresponds to the reference pressure is ρ_P , then the fluid flux can be defined as:

$$q = \frac{Q_m}{\rho_P 2r\pi H} \quad (6.10)$$

The problem can be simplified further by applying the dimensionless transformation defined in Chapter 4:

$$r_D = \frac{r^2}{r_e^2} \quad (6.11)$$

$$t_D = \frac{Q_m t}{\rho_P \pi r_e^2 H \phi} \quad (6.12)$$

Substitution of equations (6.10)-(6.12) into equation (6.8) gives the same dimensionless form of a governing partial differential equation as in the incompressible displacement:

$$\frac{\partial S_1}{\partial t_D} + \frac{\partial f_1}{\partial r_D} = 0 \quad (6.13)$$

and therefore, all the theory presented previously for the modelling of immiscible and compositional non-Darcy flow can be applied. To solve the problem, however, it is necessary to define convergence criterion in order to determine the reference CO₂ density.

In the Vilarrasa et al. (2010) iteration algorithm, the reference density corresponds to the average CO₂ density within the two-phase region. The initial estimate of the mean CO₂ density was taken from the literature (Bachu, 2003), and the convergence criterion was suggested to be either 1) changes in the interface position, or 2) changes in the mean CO₂ density. When applied to the model developed in this study, however, the convergence criterion proposed by Vilarrasa et al. (2010) proved to be inaccurate. The solution calculated at the converged reference pressure consistently underestimated pressures compared to those obtained by the reservoir simulator. A possible reason could be that the analytical solutions presented in this study use nonlinear relative permeability functions, which results in the solution being more sensitive to pressure changes than the one for the gravity-dominated flow analysed in Vilarrasa et al. (2010). Furthermore, the change of the fluid flux in the radial direction is influenced by the gas compressibility. Therefore, in this study, a velocity convergence criterion is suggested to determine the reference CO₂ density.

Velocity convergence algorithm

In a compressible two-phase displacement, the change of the fluid flux is defined by equation (6.9). If gas compressibility, c_1 is defined as (Bear, 1979):

$$c_1 = \frac{1}{\rho_1} \frac{d\rho_1}{dP} \quad (6.14)$$

and pressure change is a function of total fluid flux

$$\frac{dP}{dr} = -\frac{q}{k} \left(\frac{k_{r1}}{\mu_1} + \frac{k_{r2}}{\mu_2} \right)^{-1} \quad (6.15)$$

then equation (6.9) becomes

$$\frac{dq}{dr} = \frac{q\phi c_1}{k} \left(\frac{f_1 q}{\phi} - \frac{rS_1}{2t} \right) \left(\frac{k_{r1}}{\mu_1} + \frac{k_{r2}}{\mu_2} \right)^{-1} - \frac{q}{r} \quad (6.16)$$

Equation (6.16) is nonlinear with respect to q . However, it can be rearranged such that:

$$q = -r \frac{dq}{dr} \left[1 + \frac{\phi c_1 r^2 S_1}{2kt} \left(\frac{k_{r1}}{\mu_1} + \frac{k_{r2}}{\mu_2} \right)^{-1} - \frac{c_1 r f_1}{k} \left(\frac{k_{r1}}{\mu_1} + \frac{k_{r2}}{\mu_2} \right)^{-1} q \right]^{-1} \quad (6.17)$$

The following terms are defined:

$$q_0 = -r \frac{dq}{dr} \quad (6.18)$$

$$Z_1 = \frac{c_1 r f_1}{k} \left(\frac{k_{r1}}{\mu_1} + \frac{k_{r2}}{\mu_2} \right)^{-1} \quad (6.19)$$

$$Z_2 = \frac{\phi c_1 r^2 S_1}{2kt} \left(\frac{k_{r1}}{\mu_1} + \frac{k_{r2}}{\mu_2} \right)^{-1} \quad (6.20)$$

where q_0 is the fluid flux in the incompressible displacement (see equation (4.6)) and Z_1 and Z_2 are compressible flow parameters. These terms transform equation (6.17) into:

$$q = \frac{q_0}{1 + Z_2 - Z_1 q} \quad (6.21)$$

Having defined fluid flux as a function of gas compressibility, the following algorithm for modelling the compressible two-phase flow is suggested (Figure 6.1):

1. Initial estimations of the reference CO₂ density, $(\rho_P)^i$ and corresponding viscosity are obtained from the initial reservoir pressure, as described in Chapter 4. Corrections to account for phase miscibility are not needed because it is assumed that partial solubility has a negligible influence on the gas phase properties.
2. Saturation and pressure profiles are calculated using the analytical models presented in Chapters 4 and 5, with a fluid flux $q = q_0$ calculated from equation (6.10)

$$q = \frac{Q_m}{2r\pi H(\rho_P)^i} \quad (6.22)$$

3. After the pressure profile is obtained, the CO₂ density distribution and gas compressibility are determined based on the density function $\rho_1 = \rho_1(P)$. The density models will be discussed in more detail below.
4. Equation (6.21) is rearranged into the form of a quadratic form $Z_1 q^2 - (1 + Z_2)q + q_0 = 0$, whose solution is the fluid flux assuming compressible displacement:

$$q = \frac{(1 + Z_2) + \sqrt{(1 + Z_2)^2 - 4Z_1 q_0}}{2Z_1} \quad (6.23)$$

The solution assumes that the correct solution is the positive root of the quadratic equation. Expressions for Z_1 and Z_2 are given in equations (6.19) and (6.20), respectively.

5. Using values of the fluid flux from equation (6.23), the mean flux is obtained from:

$$\bar{q} = \frac{1}{r_L - r_w} \int_{r_w}^{r_L} q \, dr \quad (6.24)$$

The value of the velocity integral in equation (6.24) was obtained numerically, using the trapezoidal rule.

6. Steps 2-5 are repeated until the solution converges to within some defined tolerance. The convergence criterion chosen was the change in the mean velocity, that is the error between $(\bar{q})^i$ and $(\bar{q})^{i+1}$ is compared with set tolerance criterion. If the solution has not converged, the value of the reference CO₂ density is updated based on the

value of the fluid flux at the well, $q_w = q(r = r_w)$:

$$(\rho_P)^{i+1} = \frac{Q_m}{2r_w \pi H q_w} \quad (6.25)$$

The CO₂ viscosity is assumed to be a function of CO₂ density (see equation (4.55)) and its value is updated based on the value of $(\rho_P)^{i+1}$.

Note that the same approach can be applied for the modelling of non-Darcy immiscible displacement, if the saturation and pressure profiles are determined following the procedure given in Chapter 4.

6.3 Model development

To determine the change of CO₂ density and compressibility in the reservoir, it is necessary to define the $\rho_1 = \rho_1(P)$ function. This is discussed in more detail below.

6.3.1 Density functions

Gas compressibility, c_1 is defined by (Bear, 1979):

$$c_1 = \frac{1}{\rho_1} \frac{d\rho_1}{dP} = -\frac{1}{V} \frac{dV}{dP} \quad (6.26)$$

In the model developed in this study, three functional dependences for $\rho_1 = \rho_1(P)$ were implemented:

1. CO₂ density is assumed to be a function of the gas molar volume, V defined using the Redlich and Kwong (1949) equation of state and calculated as presented in section 4.3.1. CO₂ compressibility can then be obtained by differentiating equation (4.52) with respect to V , which gives:

$$c_1 = \frac{1}{V} \left[\frac{RT}{(V - d_c)^2} + \frac{a_c(2V + d_c)}{T^{0.5}V^2(V + d_c)^2} \right]^{-1} \quad (6.27)$$

2. Equation (6.26) can be differentiated by fixing the value of gas compressibility at some reference pressure, which gives:

$$\rho_1 = \rho_{10} \exp [c_P(P - P_0)] \quad (6.28)$$

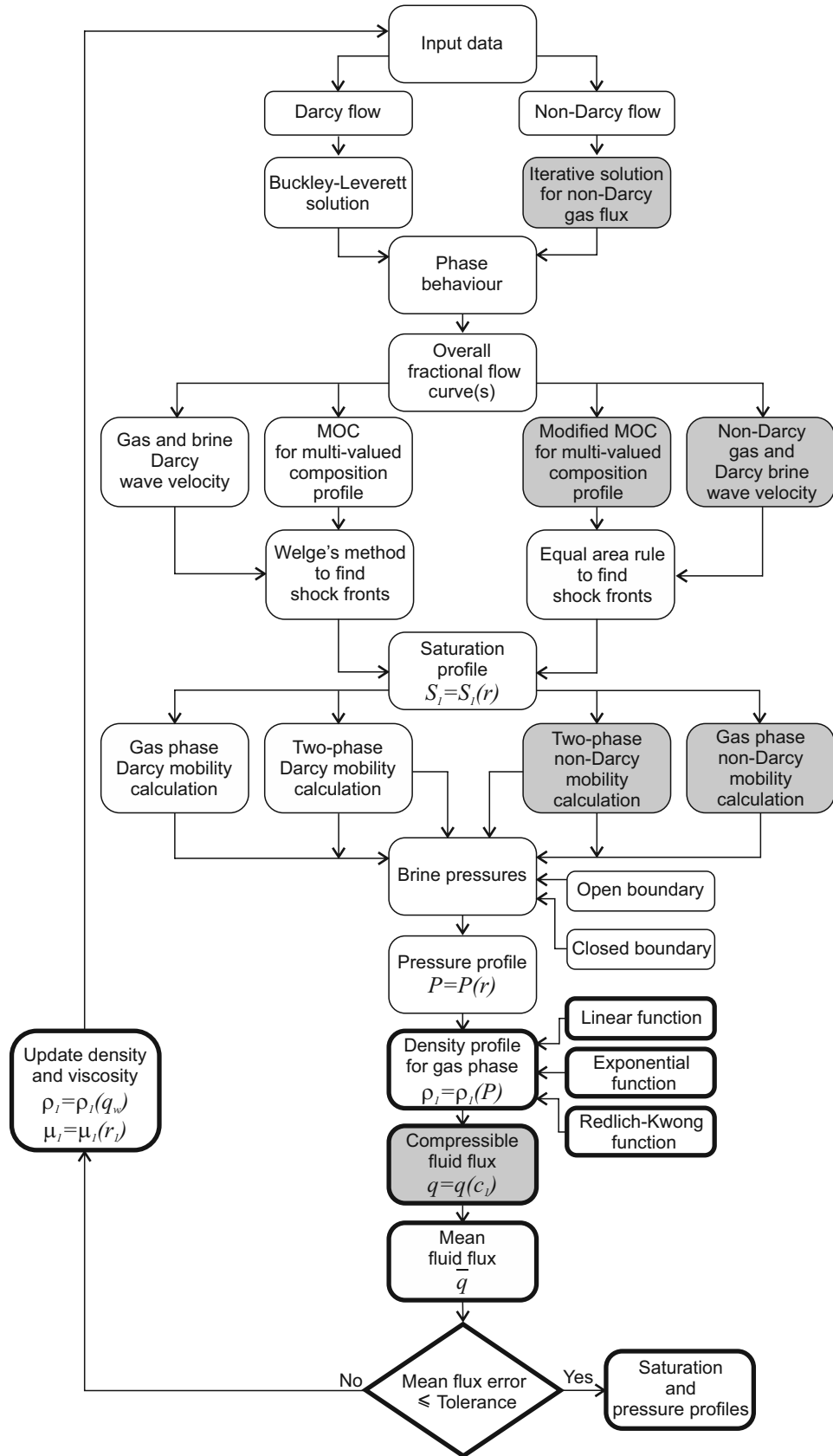


Figure 6.1: Algorithm to account for CO₂ compressibility in Darcy and non-Darcy solutions. Additional modules, compared with those developed in chapters 4 and 5, are shown with a thick black line.

where ρ_{10} is CO₂ density at the initial reservoir pressure, P_0 , and c_P is CO₂ compressibility at a reference pressure. Since $d\rho_1/dP = \rho_1 c_P$, CO₂ compressibility is constant and equal to the reference compressibility $c_1 = c_P$.

3. Without losing significant accuracy, equation (6.28) can be approximated by the first two terms of the Taylor series as:

$$\rho_1 = \rho_{10}[1 + c_P(P - P_0)] \quad (6.29)$$

which gives the following formulation for CO₂ compressibility

$$c_1 = \frac{c_P}{1 + c_P(P - P_0)} \quad (6.30)$$

To calculate CO₂ density using equations (6.28) and (6.29), it is necessary to determine the value of c_P . In this study, the reference compressibility was assumed to be determined by the aquifer temperature. Its value was obtained by fitting the linear relationship within the range of pressures from P_0 to $P_{max}=60$ MPa. Values of ρ_1 at these end points were determined using the Redlich and Kwong (1949) equation of state. Results for $T = 40^\circ\text{C}$ and $P_0=12$ MPa are presented in Figure 6.2. The optimised value of the reference compressibility is equal to $c_P = 1.04 \cdot 10^{-8} \text{ Pa}^{-1}$. Neither the linear nor exponential correlation could reproduce accurately the highly nonlinear CO₂ density change over the injection pressure range obtained from the Redlich and Kwong (1949) approximation.

Figure 6.3 shows a summary plot of CO₂ compressibility for the different density functions. The Redlich and Kwong (1949) equation of state predicts a highly nonlinear compressibility of the system. In particular, CO₂ compressibility significantly decreases as pressures approach the upper limit of P_{max} . The linear $\rho_1 = \rho_1(P)$ correlation relaxes the compressibility dependence on the reservoir pressure, while the exponential function compressibility is pressure independent and significantly diverges from the nonlinear ones, especially at high reservoir temperatures. Various density functions, however, could be used for testing the performance of numerical schemes.

6.4 Model results

The compressible non-Darcy model was implemented for the reference case CO₂ injection problem presented in Chapter 5 (i.e. $K_s = 0.15 \text{ g cm}^{-3}$). Initial and boundary conditions

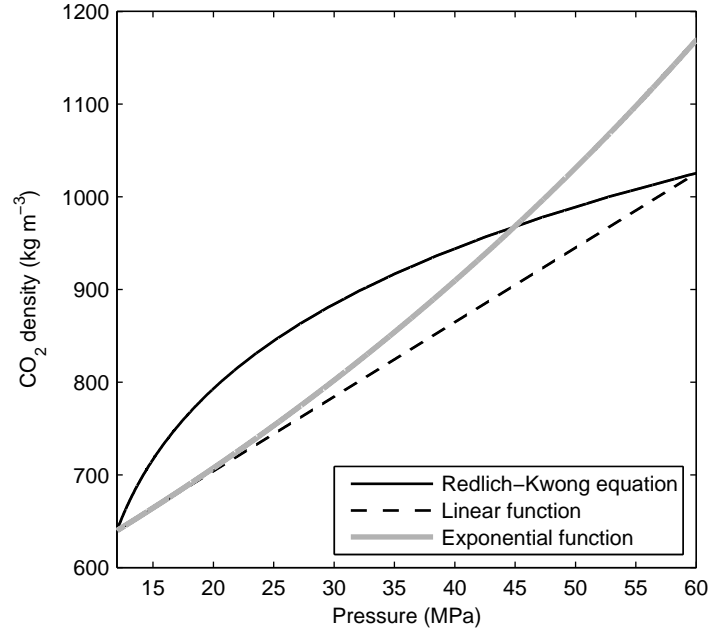


Figure 6.2: CO₂ density functions at $T = 40^\circ\text{C}$. Exponential and linear correlations are calculated from equations (6.28) and (6.29), respectively, with $c_P = 1.04 \cdot 10^{-8} \text{ Pa}^{-1}$ and $\rho_{10} = 691.8 \text{ kgm}^{-3}$ at $P_0 = 12 \text{ MPa}$.

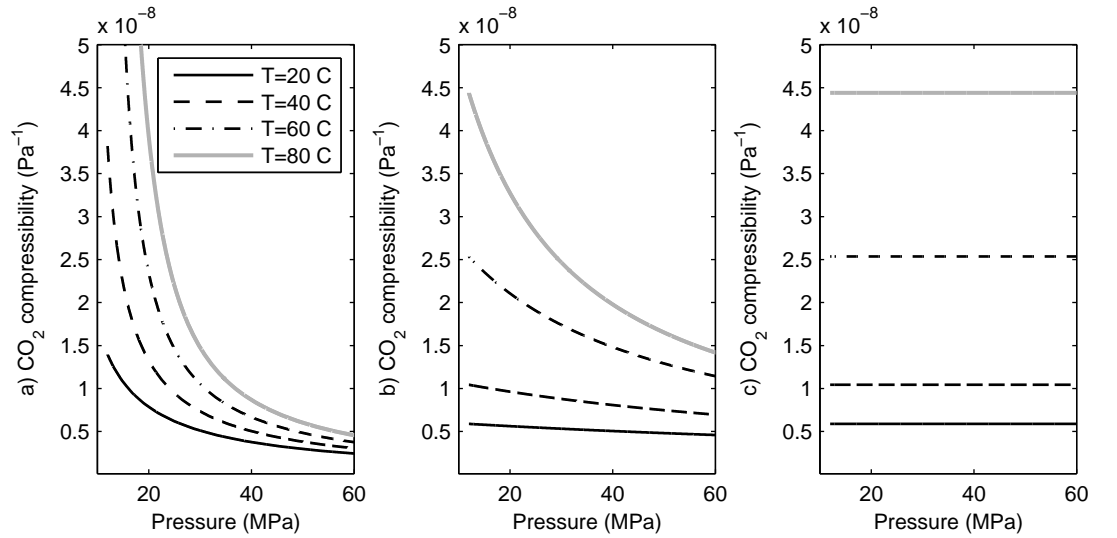


Figure 6.3: CO₂ compressibility as a function of reservoir temperature and pressure calculated from: a) Redlich and Kwong (1949) approximation (equation (6.27)), b) linear density approximation (equation (6.30)) and c) exponential density approximation ($c_1 = c_P$).

and fluid properties are given in Tables 4.5 and 5.2. The relative permeability values for the two-phase region are shown in Figure 4.13. The iterative scheme used an error tolerance of 0.001 and the maximum number of iterations set to 100. In all simulations, the Redlich and Kwong (1949) density model was used.

6.4.1 Saturation and pressure profiles

The analytical solutions presented in this study enabled comparison of different modelling scenarios of the CO₂ injection problem. The summary of the results for a fixed time ($t = 5$ days) is shown in Figure 6.4. In both Darcy and non-Darcy displacements, incompressible solutions overpredicted the gas plume extent and pressure buildup (subfigures 6.4a and 6.4c). While the extension of the Darcy solution with the constant Forchheimer coefficient does not influence the saturation distribution, the results of the near-well pressure are significantly altered. Finally, a fully non-Darcy compressible displacement with saturation-dependent Forchheimer flow significantly influences both saturation and pressure distributions (subfigures 6.4b and 6.4d). The compressible solution gives higher gas saturations along the two-phase region and at the shock fronts. This would be advantageous in terms of both displacement efficiency and salt precipitation in the near-well region. Gas compressibility reduces the pressures within the reservoir, which again is favourable for the CO₂ injection process.

The effects of non-Darcy flow in compressible displacement can be seen in the results given in Table 6.1. As in the incompressible displacement, there is no significant difference between leading front location values for Darcy and constant non-Darcy flow, while the well pressure is sensitive to any change in the non-Darcy flow modelling. Moreover, the pressure at the well in variable non-Darcy displacement decreases with time because the inertial effects become less significant as the gas plume advances further into the reservoir.

6.4.2 Effects on CO₂ injectivity

To quantify the effects of non-Darcy flow on the key parameters for CO₂ injection in saline aquifers, the following relative error functions are defined:

$$\epsilon_L = \frac{r_{Lf} - r_{Ld}}{r_{Lf}} \quad (6.31)$$

$$\epsilon_P = \frac{P_{wf} - P_{wd}}{P_{wf}} \quad (6.32)$$

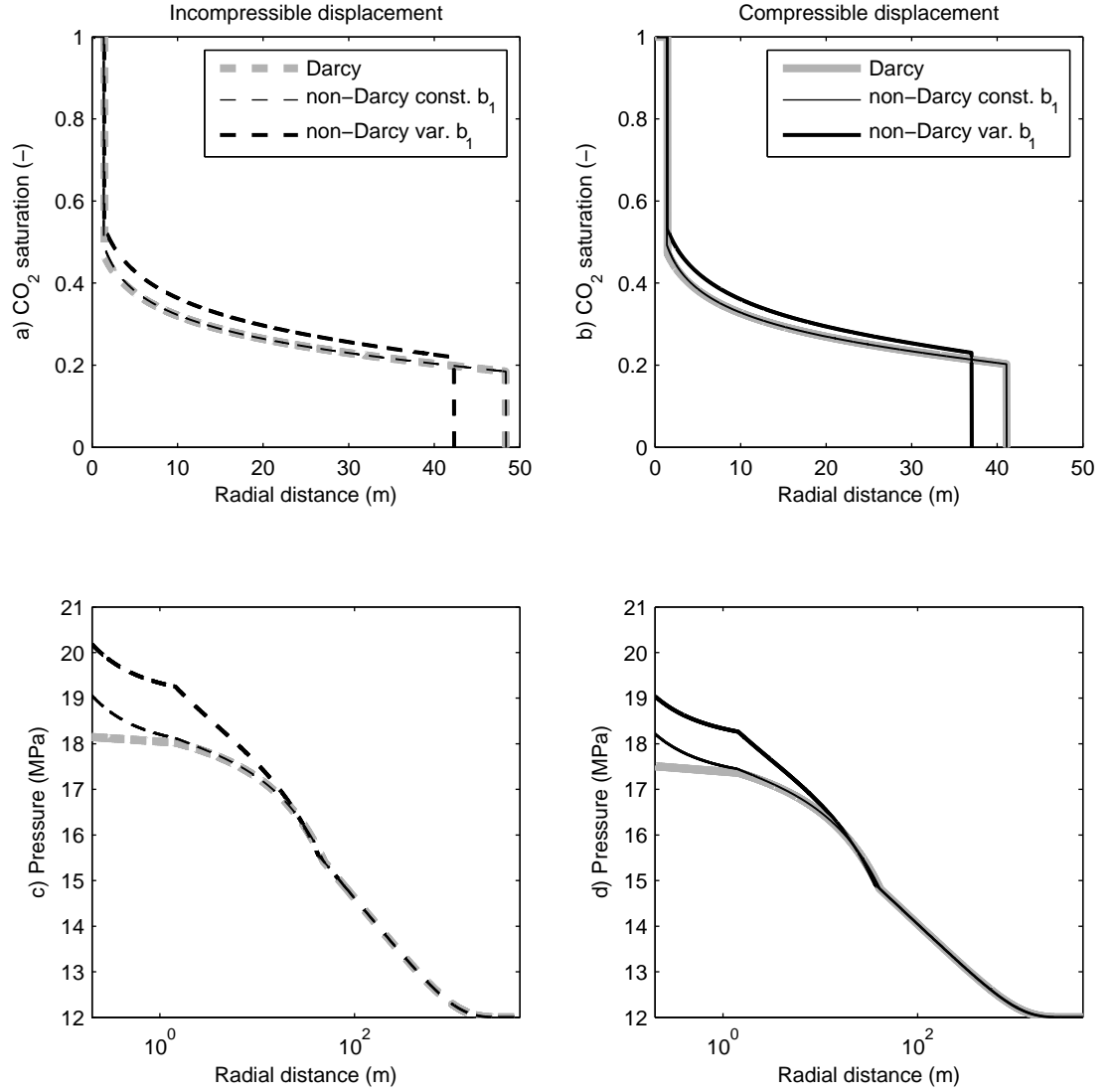


Figure 6.4: Effects of non-Darcy flow in incompressible and compressible displacements on a)-b) CO₂ saturation and c)-d) pressure distributions 5 days after the beginning of injection for $Q_m = 100 \text{ kg s}^{-1}$. Forchheimer coefficient for non-Darcy flow is $W = 3.2 \cdot 10^{-7} \text{ m}^{1.5}$.

Table 6.1: Simulation results for compressible Darcy ($W=0$) and non-Darcy ($W=3.2 \cdot 10^{-7} \text{ m}^{1.5}$) flow with constant and variable Forchheimer coefficient b_1 .

	time	Darcy	Non-Darcy	
	(days)		constant b_1	variable b_1
$\rho_P(\text{ kg m}^{-3})$	0.5	788	796	829
$r_L(\text{ m})$	0.5	13.3	13.2	11.4
$P_w(\text{ MPa})$	0.5	17.5	18.2	20.7
$\rho_P(\text{ kg m}^{-3})$	5	789	798	808
$r_L(\text{ m})$	5	42.1	41.9	38.1
$P_w(\text{ MPa})$	5	17.6	18.3	19.2
$\rho_P(\text{ kg m}^{-3})$	50	790	799	801
$r_L(\text{ m})$	50	133	132	124
$P_w(\text{ MPa})$	50	17.7	18.4	18.6

where ϵ_L and ϵ_P are the relative errors in leading front location and well pressure estimations, respectively, assuming that variable non-Darcy flow conditions are representative for the injection formation. Subscripts f and d represent Forchheimer and Darcy flow, respectively. Results for the possible range of mass injection rates ($3 \leq Q_m \leq 120 \text{ kg m}^{-3}$) and variable formation permeabilities are shown in Figure 6.5. The errors associated with neglecting the non-Darcy effects increase significantly with increasing injection rate, that is when viscous effects dominate the displacement process. The error is more significant in the less permeable formations, where the fluid flow is restricted by the narrow flow paths. Errors in predicting the location of the leading front are within the range of 6-10%, with the Darcy model consistently overpredicting the plume extent (Figure 6.5a). The effect of formation permeability is particularly evident in the well pressure estimations (Figure 6.5b). If the formation permeability is reduced by an order of magnitude, well pressures at high injection rates may be underestimated by more than 10%.

The compressible non-Darcy model enables the analysis of the non-Darcy effects on the CO_2 injectivity. If CO_2 injectivity is defined as (Metz, 2005):

$$I = \frac{Q_m}{\Delta P} = \frac{Q_m}{P_w - P_0} \quad (6.33)$$

where $P_0=12 \text{ MPa}$ is the initial reservoir pressure, the results shown in Figure 6.6 demon-

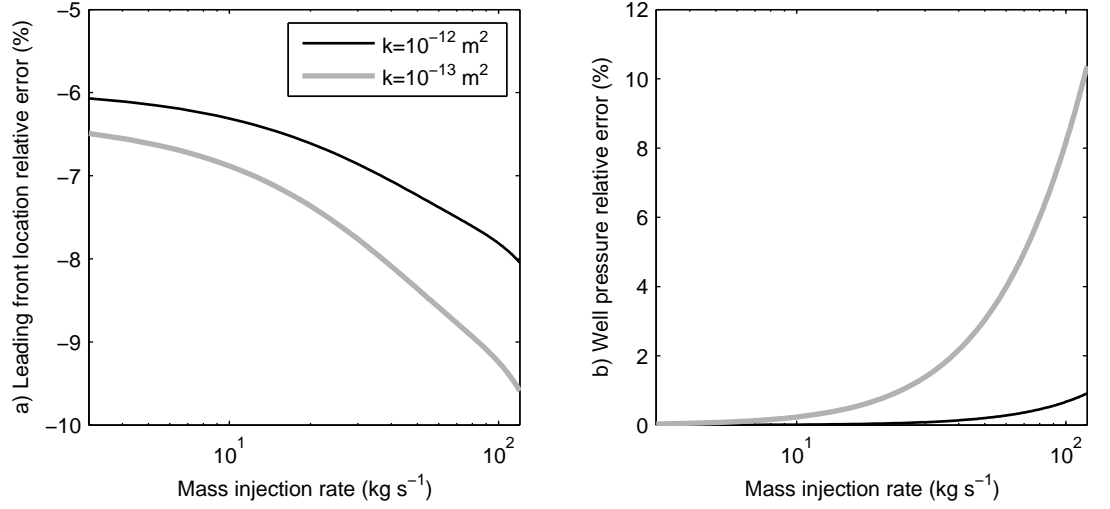


Figure 6.5: Relative error in a) leading front location and b) well pressure estimations associated with neglecting the non-Darcy effects in compressible displacement. Formation thickness is $H = 200$ m and Forchheimer coefficient for non-Darcy flow is $W=3.2 \cdot 10^{-7} \text{ m}^{1.5}$.

strate clearly the difference in the response of the Darcy and non-Darcy systems. Under Darcy flow conditions, the increase in the injection rate implies almost linear increase in the CO₂ injectivity with pressure. This is because the basic assumption of Darcy flow is a linear relationship between the fluid flux and pressure gradient. Under non-Darcy conditions, however, that is not the case. In non-Darcy displacements, the pressure within the reservoir increases inertial effects with respect to the injection rate. At high flow velocities, the influence of the pressure buildup at the well starts to suppress the positive effect of the increasing injection rate, and the injectivity starts to decline. Therefore, if non-Darcy flow conditions are assumed to be valid, the optimal injection rate should be selected as the maximum of the injectivity function. Results also show that in non-Darcy displacements, the maximum of the injectivity function depends on the formation permeability. Low permeability formations (Figure 6.6b) are highly sensitive to non-Darcy effects and could experience a significant loss of CO₂ injectivity at high injection rates.

6.4.3 Comparison with reservoir simulator

The performance of the compressible solution was tested by comparing its results to the output from the reservoir simulator ECLIPSE 300 presented in Chapter 5. Since the simulator cannot model directly the Forchheimer coefficient dependence on phase saturations, the analytical solution was set to model the non-Darcy flow with a constant value of b_1 .

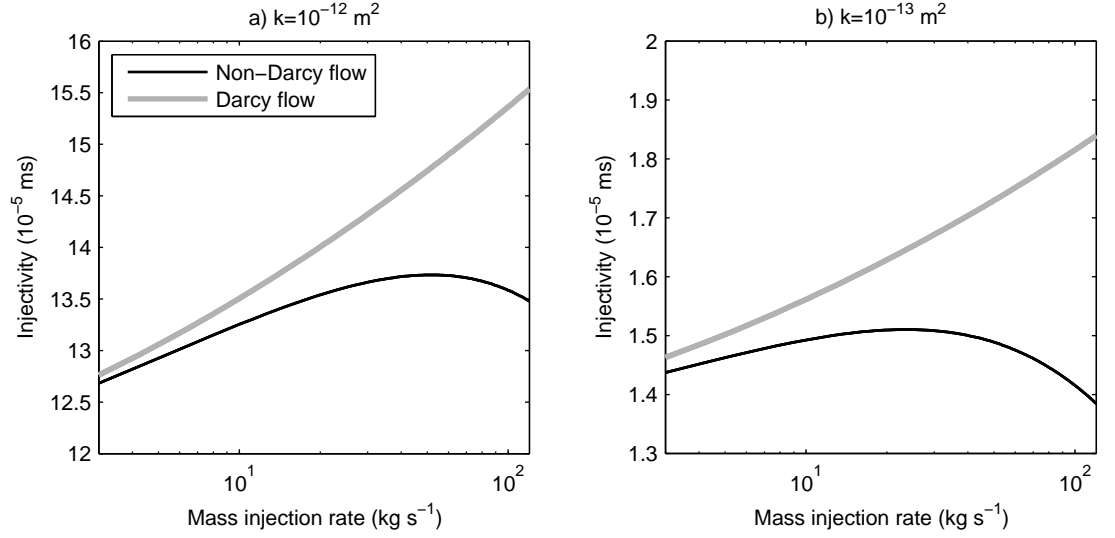


Figure 6.6: CO₂ injectivity under Darcy and non-Darcy flow conditions and variable formation permeabilities. Formation thickness is $H = 200 \text{ m}$ and Forchheimer coefficient for non-Darcy flow is $W=3.2 \cdot 10^{-7} \text{ m}^{1.5}$.

Reservoir simulator parameters are given in Table 5.4.

Figure 6.7 shows CO₂ saturation and pressure distributions before the influence of the boundary is felt at the well, as modelled by the incompressible and compressible non-Darcy models and the reservoir simulator. Both saturation and pressure profiles show excellent agreement between simulator and compressible model results. The results also show the possible errors in leading front location and reservoir pressures estimations if effects of compressibility are neglected. Incompressible model predictions overestimate both pressure and frontal advance, and would therefore indicate a less favourable outcome for CO₂ storage.

In all analytical model simulations of compressible flow, the solution converged in five or less iterations, making the model computationally very efficient. Results in Table 6.1 show the values of the reference CO₂ density, ρ_P , which is time-dependent and proportional to the value of P_w . While values of ρ_P for Darcy and constant non-Darcy displacements do not vary significantly with respect to time, compressible solutions for variable non-Darcy flow require high gas densities to accurately match the full compressible displacement modelled by the reservoir simulator.

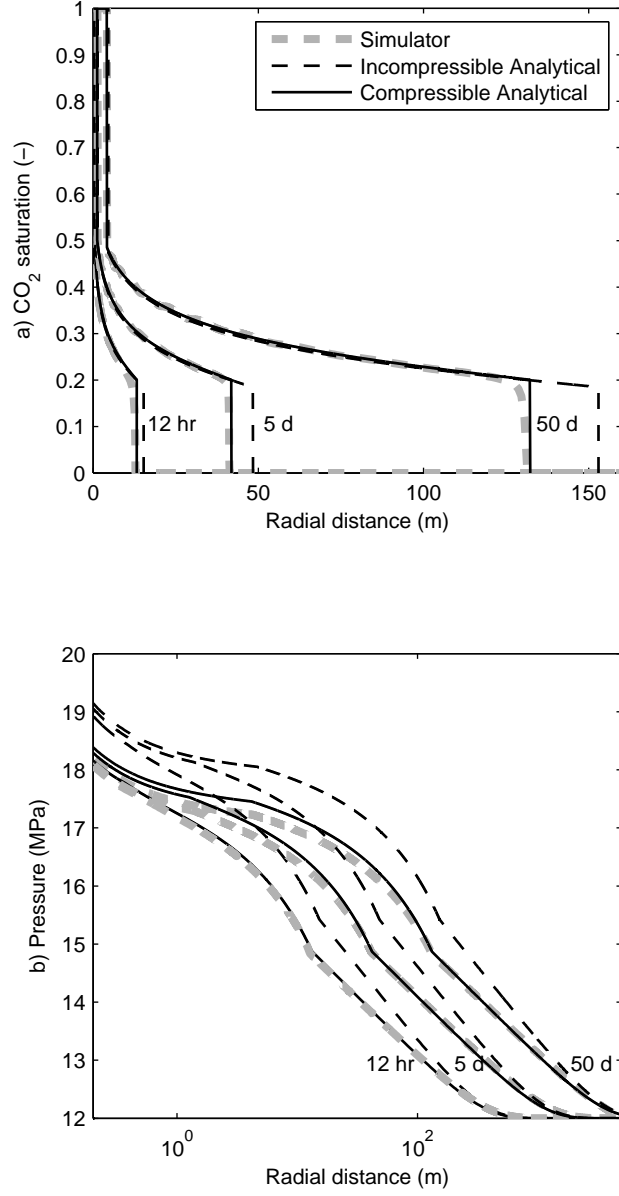


Figure 6.7: Comparison of a) CO₂ saturation and b) pressure distributions during early injection period ($t \leq 50$ days). The injection rate is $Q_m = 100 \text{ kg s}^{-1}$ and the Forchheimer flow constant for non-Darcy flow is $W = 3.2 \cdot 10^{-7} \text{ m}^{1.5}$. The Forchheimer coefficient, b_1 is assumed to be independent of the gas phase saturation for the purpose of benchmarking.

6.5 Conclusions

To obtain the most accurate estimations of key parameters that define the behaviour of the injected CO₂, it is necessary to account for the compressibility of the gas phase. In this chapter, the compositional non-Darcy model presented in Chapter 5 was extended to include a compressibility correction of gas phase properties. The iterative algorithm given by Vilarrasa et al. (2010) was modified so that:

1. The initial estimation of fluid properties was based on the initial reservoir pressure.
2. Three density functions (linear, exponential and Redlich and Kwong (1949)) were selected for the modelling of the $\rho_1 = \rho_1(P)$ relationship. Systems with highly nonlinear compressibility should be modelled using the Redlich and Kwong (1949) approximation (Figure 6.3). Linear and exponential correlations could be used to verify numerical schemes during their development stage, when simpler models enable easier tracking of possible errors in the code.
3. The velocity convergence criterion was derived based on the change of the mean fluid flux under compressible flow conditions.

The comparison of possible modelling scenarios of CO₂ injection problems showed the significance of including the full physics of the displacement for analysis of both Darcy and non-Darcy flow. If the effects of gas compressibility are neglected, both pressure and shock front estimations will be overpredicted (Figure 6.4). The analysis of non-Darcy effects on shock front location and pressure prediction in compressible displacement has shown that by neglecting non-Darcy flow, relative errors up to 10% in leading shock front location and well pressure estimation may be obtained (Figure 6.5). Estimation errors were highly sensitive to the change in the injection rate and formation permeability, significantly increasing for highly non-Darcy flow through low permeability formations.

While CO₂ injectivity under Darcy conditions can be increased by increasing the injection rate, non-Darcy injectivity has been shown to have a limiting value determined by the substantial pressure increase at high injection rates (Figure 6.6). The maximum injectivity was further constrained by the low formation permeability.

The application of the non-Darcy model with a constant Forchheimer coefficient and its comparison with the corresponding simulation results showed excellent agreement of both saturation and pressure distributions (Figure 6.7). This verified the compressible non-Darcy solution for analyses of CO₂ injection problems.

Although still limited to constant formation properties and not taking into account the effects of capillary forces and salt precipitation on pressure distribution, and effects of formation dissolution due to chemical reactions on permeability increase, the compressible non-Darcy model presented in this chapter therefore improves significantly the predictions of the CO₂ behaviour during injection into saline formations. This computationally efficient solution, which includes various density functions, can be used for reliable estimations of key parameters that define the suitability of an aquifer for CO₂ storage, as well as for analysis of injection scenarios. Furthermore, it can be used as a benchmark for any numerical model of the corresponding problem.

Chapter 7

Summary and Conclusions

The most important research questions regarding CO₂ injectivity are how much, how fast and for how long can CO₂ be injected into a formation. To answer these questions, it is necessary to determine all the effects that control CO₂ injectivity and their relative influence under conditions representative of sedimentary formations. This thesis aimed to develop analytical equations to describe non-Darcy two-phase displacement in saline formations and hence:

- Improve the understanding of the non-Darcy flow and how it controls the movement of water and gas through the subsurface formation, and in particular through the near-well region.
- Provide solutions that can be used to verify the numerical solutions that are used to perform predictions of complex flows and/or they can be used as a part of a numerical scheme to speed up the calculations.

7.1 Summary of thesis

7.1.1 Single-phase system pressure buildup

The first step in analysing the non-Darcy effects on fluid movement through a confined aquifer was to develop an analytical solution for the pressure buildup at the well during water injection into a closed formation. The model assumes that before the influence of the formation boundary is felt at the well, a modified form of the solution given by Mathias et al. (2008) can be implemented. During semi-steady state flow conditions, when the boundary begins to affect the well pressure, the analytical solution derived in this study becomes valid. By comparing the results of the Forchheimer analytical solution and the

corresponding finite difference scheme for a closed circular formation, it was shown in Chapter 3 that there is a high level of agreement between the solutions for all levels of inertial effects. The solution showed that non-Darcy well pressures were increased compared to linear flow.

The analytical solution was then modified to address the problem of multiple well systems with non-Darcy liquid flow. The problem was approached from the perspective of determining the pressure at the critical well, which was located in the centre of an array of equally spaced wells. It was proposed that a single well situated in a circular region of the equivalent plan area adequately represents such a system. The performance of the multiple well solution was verified by comparison of results with the numerical model simulations of the original square domain problem. Results showed that if the equivalent radius of a confined aquifer is expressed as a function of the well spacing, transformed to account for the plan area difference, then the critical well pressure can be determined using the same solution given for a circular domain.

Although limited to confined aquifers, the analytical model presented in Chapter 3 enables analysis of the Forchheimer liquid flow, both in closed formations and multiple well systems. Furthermore, the presented methodology potentially can be implemented for multiple well system analysis of non-Darcy two-phase flow problems.

7.1.2 Two-phase system saturation distribution and salt precipitation

The quantity of CO₂ that can be injected in a saline formation is influenced by the process of salt precipitation, which occurs due to the vaporisation of a resident brine into the flowing gas phase and can significantly decrease the effective aquifer porosity in a near-well region. In this study, the analytical model formulated by Zeidouni et al. (2009) for estimating solid salt saturation was implemented. The solution is based on the assumption that salt saturation is a function of the liquid phase saturation immediately downstream of the trailing shock. The first step, therefore, was to determine the saturation distribution during the CO₂ injection process. Furthermore, the location of the leading edge of the gas plume determines how far CO₂ will spread.

Immiscible displacement

The analysis of experimental data from the literature in Chapter 4 has shown that the gas phase may exhibit non-Darcy behaviour. Furthermore, in radial displacements, the fluid flux changes with the distance from the well. These were the reasons for extending the

Buckley and Leverett (1942) solution to include:

- The non-Darcy flow of the gas phase using the two-phase extension of the Forchheimer equation (Forchheimer, 1901; Wu et al., 2011).
- An iterative procedure for the calculation of the non-Darcy gas phase velocity.
- A spatially varying fractional flow function.
- Modification of the method of characteristics for determining the saturation profile to account for the non-Darcy change of gas flux with the distance from the well.

The results presented in Chapter 4 showed excellent agreement with the corresponding numerical solution, emphasising two main differences in the response of the CO₂-brine system to non-Darcy flow conditions compared to the corresponding Darcy flow:

1. The fractional flow function varies with the distance from the well, representing the influence of inertial effects in slowing down the gas phase flow closer to the well. This results in better displacement efficiency by the injected gas.
2. The displacement is controlled additionally by the injection rate and level of inertial effects, which could play a significant role in the assessment of the aquifer suitability for CO₂ injection. Highly non-Darcy flow conditions will result in the gas plume advancing more slowly into the reservoir, with higher saturation values along the two-phase region and across the leading shock front. Neglecting non-Darcy effects could therefore lead to an overestimation of the lateral extent of the CO₂ plume.

Compositional displacement

The extension of the immiscible model to the compositional non-Darcy solution presented in Chapter 5 enabled analysis of near-well effects and salt precipitation modelling. In this model:

- The single-phase CO₂ region was added, to account for the loss of pore space due to salt precipitation.
- Within the gas region, non-Darcy effects were modelled by modifying the representation of the gas phase wave velocity to account for spatially varying flow.

The resulting compositional non-Darcy solution was verified by comparing results with the simulations from the reservoir simulator ECLIPSE 300. Results showed that:

1. The saturation distribution within the single-phase gas and two-phase regions was well reproduced by the non-Darcy model.
2. The analytical model managed to mimic accurately the near-well behaviour of the gas phase and showed that non-Darcy conditions will result in a reduction in salt precipitation compared to the situation during Darcy flow, especially during the initial stages of injection.
3. Salt saturation and permeability reduction values were increased in proportion to the increment of brine salinity.
4. There was a significant disagreement in the leading shock front predictions, and slight disagreement in estimations of the dry-out front extent, which was found to be due to neglecting the effects of gas compressibility.

Compressible displacement

The final improvement of the non-Darcy solution was achieved in Chapter 6 by including the effects of CO₂ compressibility. This involved modifying the Vilarrasa et al. (2010) iteration algorithm so that:

- The initial fluid properties were chosen to be calculated at the initial reservoir pressure.
- The convergence criterion was based on the change of the mean fluid flux under compressible flow conditions.

The compressible solution could use any of three different density functions (linear, exponential and Redlich and Kwong (1949)). The Redlich and Kwong (1949) model is most suitable for systems where compressibility changes nonlinearly with reservoir pressure.

The compressible model showed excellent agreement with results obtained from the reservoir simulator. Furthermore, analysis of non-Darcy flow using a saturation-dependent Forchheimer parameter showed that:

1. Compressible flow results in higher gas saturations within the two-phase region and decreased mobility of the gas phase, which has positive effects on CO₂ injectivity.
2. The relative error associated with neglecting the non-Darcy effects was increasing with the mass injection rate, indicating the significance of non-Darcy effects in

viscous-dominated flows. The Darcy model was overestimating the lateral plume extent over the whole range of analysed injection scenarios.

7.1.3 Two-phase system pressure buildup

The rate at which CO₂ can be injected in a confined saline formation determines the increase of the pressure within the reservoir formation near the well. In this study, the pressure distribution in a two-phase non-Darcy displacement was obtained by adding together the pressure gradients, starting from the far-field formation boundary:

- Within the single-phase brine region, solutions for pressure were obtained using transient (Theis, 1935) and semi-steady state analytical solutions, depending on the boundary condition, and the time at which the influence of the far-field boundary is felt at the well.
- The pressure distribution within two-phase and CO₂ regions was found by numerical integration of the mass conservation equation solved for the non-Darcy flow of the gas phase. Integration parameters, that is the relative permeability and the Forchheimer factor, were obtained from the gas phase saturation profile using $S_1 - k_r$ and $S_1 - \beta$ correlations determined from the modelling of two-phase displacement.

The duration of CO₂ injection is defined by the formation boundary or distance between the injection wells. If the aquifer is infinite in extent or bounded by a constant pressure boundary, then for a constant injection rate, CO₂ injectivity will increase with time. In a low permeability formation, however, there will be a significant increase in pressure once the influence of the boundary is felt at the well. To explore these effects, the non-Darcy pressure solution was designed to include two modules for the brine region, which account for the influence of the formation boundary:

- A pressure integral for open aquifers, where the solution is found by implementing the Thiem (1906) analytical solution.
- A pressure integral for closed aquifers, where the solution was found by setting the value of the well radius as the outside edge of the two-phase region (Mathias et al., 2011b).

The transition between transient and boundary-dependent solutions was determined analytically based on the transition times.

Pressure distribution

The results presented in Chapter 4 showed that the most important change in the displacement in the non-Darcy flow is the significant increase of the pressure in the two-phase region compared to Darcy flow conditions. The non-Darcy pressure solution had the following properties:

1. The solution was shown to be highly sensitive to the level of inertial effects defined by the value of the Forchheimer flow constant. This could indicate the threshold value of non-Darcy flow for a given formation, which would determine its suitability for CO₂ injection processes.
2. Before the perturbation has reached the formation boundary, estimations of the well pressure decreased with respect to time since the beginning of the injection. The reason is that during initial stages of injection, the saturation front is close to the well and the whole profile is under the significant influence of the non-Darcy effects. This indicated that the critical period for CO₂ storage under non-Darcy conditions, when the fracturing of the formation may occur, is immediately after the beginning of the injection process.

Analysis of the effects of the formation boundary yielded the expected pressure response. The pressure increase in closed formations proved to be significant in both Darcy and non-Darcy displacements. This indicated that significant pressure buildup may also occur in systems of multiple wells due to the well interference. Therefore, the careful planning and monitoring of these systems is necessary in order to prevent a pressure increase above the formation fracture limit.

Effects of miscibility and compressibility

After extending the model to encompass compositional and compressible analysis, the significant pressure increase obtained from the immiscible simulations was shown to have been slightly overestimated. The results indicated:

1. A reduction of the reservoir pressure in the compositional displacement within the newly formed CO₂ region, which was due to the increase of the gas relative permeability once all of the brine had evaporated into the flowing gas phase.
2. A further pressure decrease in two-phase and dry-out zones, due to the effects of CO₂ compressibility, hence reducing the adverse effects of non-Darcy flow.

3. The sensitivity of pressure estimations to changes in brine salinity. In the higher salinity case, the pressure increase within the single-phase liquid zone resulted in the additional pressure buildup at the well .

Finally, analysis of the influence of non-Darcy flow on CO₂ injectivity showed that the optimum injection rate is given by the maximum of the injectivity function, which is constrained by the increase of the well pressure at high injection rates and low formation permeability.

7.2 Summary of contributions to knowledge

The main contribution of this thesis is the development of a set of analytical solutions that can model a spatially varying non-Darcy flow in a radial two-phase system, taking into account effects of phase miscibility and gas compressibility. These were applied to the modelling of CO₂ injection into saline aquifers. The models permit analysis of the near-well effects during the injection process for various reservoir properties, which is crucial in determining the suitability of a formation for CO₂ storage and quick ranking of the storage sites. They can be also used to validate numerical simulations before they are used to drive important decisions regarding the efficiency and design of CO₂ storage projects.

Another important contribution is the insight that these models give into the non-Darcy two-phase displacement process occurring during CO₂ injection. The application examples analysed in this study indicated that Darcy flow models may be inadequate for the analysis of CO₂ injection processes in low permeability formations when gas is injected at high rates. In these cases, supercritical CO₂ is likely to experience non-Darcy behaviour, which may potentially slow down the gas phase flow. This could have the following implications for CO₂ storage into saline aquifers:

- The additional pressure increase in the near-well region, which is highly sensitive to the level of inertial effects. For the highest level of non-Darcy flow analysed, the pressure at the well increased up to 190% compared to the case of Darcy flow.
- Better displacement efficiency of the injected gas. The radial extent of the CO₂ plume was reduced by a maximum of 15% compared to the Darcy flow.
- Reduction in the solid salt saturation. Up to 25% less solid salt may precipitate during early injection times compared to the Darcy flow.

The most significant pressure buildup in non-Darcy flow will occur immediately after the beginning of the injection process and will decrease with time, until it becomes influenced by the formation boundary. Furthermore, non-Darcy CO₂ injectivity was shown to be limited by increase of the pressure at the well at high injection rates. It was also found to be highly sensitive to the formation permeability, which alters the selection criterion for the optimal injection strategy.

Finally, another advance arising from this thesis concerns non-Darcy liquid flow in closed formations. It was shown that by implementing the area transformation factor, the analytical solution for a closed circular domain can be used to calculate the critical pressure at a well located in an array of equally spaced wells.

7.3 Recommendations for further work

The models presented in this study provide a comprehensive description of two-phase non-Darcy displacements. However, there are a couple of aspects that need to be explored further, which are discussed in more detail below.

7.3.1 Estimation of Forchheimer coefficient

In this study, the non-Darcy models were applied to data obtained from the literature and all parameters may not be consistent for a single formation. In particular, the values of the Forchheimer flow constant for the gas phase, W were derived from the scarce experimental data, which cover a very narrow range of formation permeabilities. More data are needed that can be used to predict the Forchheimer coefficient for a wider range of conditions and to validate the values of parameters used in simulations. Ideally, these values should be representative of realistic porous formations. One approach could be to predict the values of the Forchheimer coefficient using Lattice-Boltzmann simulations of two-phase flow (Pan et al., 2004) in CT-images of a real porous media (Dong, 2007). This approach was successfully applied by Chukwudozie et al. (2012) to obtain values of the non-Darcy factor for single-phase flow in Castlegate sandstones.

7.3.2 Correction of pressure estimation due to salt precipitation

In Chapter 5 it was shown that salt precipitation contributes significantly to the permeability reduction in the near-well area. Up to 15% of the initial pore space could become unavailable for the fluid flow due to this process, which could have a significant influence

on the additional pressure buildup. However, in the pressure simulations performed in this study, the influence of the reduced permeability due to salt precipitation was ignored. Commercial simulators, such as ECLIPSE 300, have the option to update the permeability as a result of salt precipitation over time (see option SOLIDMMS in CO2STORE module). In analytical two-phase flow modelling, however, such transient analysis is not easy to implement. A possible solution could be to assume that the pressure distribution at a fixed time is a function of the permeability reduction at that time. If so, the ratio of the permeability reduction could be obtained from equations (5.30) and (5.31) and implemented into the expression for the gas phase pressure integral function (5.25). This, however, does not take into account the decrease in gas mobility as a function of salt precipitation within the dry-out zone.

7.3.3 Modelling the effects of rock dissolution

In addition to salt precipitation during CO₂ injection, the dissolution of primary minerals can change formation porosity and permeability and consequently affect fluid flow patterns. Noh et al. (2007) formulated a mathematical model based on mineral precipitation/dissolution rates. They coupled the model with fractional flow theory to investigate the influence of geochemistry on the CO₂ injection process. This study could be the starting point for the extension of the non-Darcy two-phase model to include the effects of rock dissolution during CO₂ injection and determine which of the two competing geochemical processes (precipitation or dissolution) will dominate the non-Darcy displacement.

7.3.4 Multiple well analysis in two-phase displacement

To achieve the desired CO₂ reduction targets, it is likely that the storage process will include multi-well injection. This is even more likely to happen if the non-Darcy flow is included in the analysis, because of the additional pressure increase at the well. Therefore, the behaviour of the two-phase system with multiple wells needs to be assessed. One approach that could be tested is the application of the area transformation factor defined by equation (3.18) in the governing equation for the two-phase flow. Pressure calculations should be performed using the distance between adjacent wells as the value for the closed outer boundary. The performance of the model could be tested against the numerical solution of the original problem (for example, a two-dimensional scheme in a reservoir simulator with an array of equally spaced wells).

7.3.5 Reservoir simulator with saturation-dependent Forchheimer flow

The results presented in Chapters 5 and 6 highlighted an important issue with the ECLIPSE module in that it cannot model a saturation-dependent Forchheimer flow. Consequently, the reservoir simulator may be substantially underestimating the impact of non-Darcy flow in CO₂ injection displacements. Better Forchheimer models in reservoir simulators could provide a reliable tool for making decisions related to design and implementation of carbon capture and storage.

7.3.6 Extending the validity of analytical models

The thorough quantification of non-Darcy effects in CO₂ storage in saline aquifers could be obtained using the solutions developed in this study to cover a wide range of aquifer properties and injection scenarios. This could provide a strong argument for including the non-Darcy analysis in CO₂ storage design projects. Furthermore, the comparison of the analytical model with a reservoir simulator that can take into account the near-well heterogeneity, for example using the scheme given by Chandra et al. (2011), could give valuable information on effects of variable formation properties on near-well pressures and potential necessity to combine the numerical near-well model with non-Darcy flow module for more reliable estimations of pressure increase during CO₂ injection.

7.4 Implications and conclusions

The potential for non-Darcy behaviour of subsurface flow has been known since the beginning of the last century, when the study by Forchheimer (1901) was published. An analytical solution that models the late time pressure distribution during immiscible CO₂ displacement has been presented by Mathias et al. (2009a), but otherwise the non-Darcy behaviour of the gas phase in CO₂ storage models has been overlooked. It is known that Forchheimer flow increases the pressure at the well. However, until this study, it was not known how significant the non-Darcy effects were likely to be in compositional and/or compressible displacements and what were the implications for CO₂ injectivity. Despite the uncertainties in estimations of the Forchheimer flow parameter that need to be explored further, the preliminary results clearly indicate that the pressure buildup and saturation profiles in low permeability formations when CO₂ is injected at high rates are influenced significantly by inertial effects. Depending on the aquifer properties, the salt precipitation calculations might significantly differ from those obtained for Darcy flow, and consequently

parameter values for permeability reduction may be impacted. The injectivity of CO₂ will have particularly important consequences for the number and location of injection wells, potentially requiring more wells than would have been estimated assuming Darcy flow conditions.

In conclusion, this thesis presents a novel approach to describe the spatially varying non-Darcy flow in deep saline aquifers. This includes modules for immiscible, compositional and compressible displacements. The models are analytical in a sense that they implement the modification of the method of characteristics for solving the governing non-linear partial differential equation. The simulation is driven by the mass injection rate and aquifer properties, and predicts saturation and pressure spatial distributions at different times. The results from the application of the model to the CO₂ injection process showed that the saturation and pressure changes obtained from numerical simulators were reproduced accurately by the model. For the range of aquifer properties analysed in this study, pressures in the near-well region and shock front saturations were significantly increased under non-Darcy flow conditions, and the extent of the gas plume was reduced. This implied that the CO₂-brine displacement process may be strongly influenced by non-Darcy effects in the examples shown. There is strong evidence that the CO₂ injectivity exhibits a different pattern under non-Darcy flow conditions, which may have important implications for the selection of optimal injection scenarios. It was also shown that the non-Darcy two-phase flow is highly sensitive to the injection rate, level of inertial effects and formation permeability. Hence, relatively modest changes in any of those parameters might lead to significantly different saturation and pressure distribution patterns in two-phase displacement.

References

- Adams, J. J. and Bachu, S. (2002). Equations of state for basin geofluids: algorithm review and intercomparison for brines. *Geofluids*, 2(4):257–271.
- Ahmadi, A., Abbasian Arani, A. A., and Lasseux, D. (2010). Numerical simulation of two-phase inertial flow in heterogeneous porous media. *Transport in Porous Media*, 84(1):177–200.
- Bachu, S. (2003). Screening and ranking of sedimentary basins for sequestration of CO₂ in geological media in response to climate change. *Environmental Geology*, 44(3):277–289.
- Bachu, S. and Adams, J. J. (2003). Sequestration of CO₂ in geological media in response to climate change: capacity of deep saline aquifers to sequester CO₂ in solution. *Energy Conversion and Management*, 44(20):3151–3175.
- Barree, R. D. and Conway, M. W. (2004). Beyond beta factors: a complete model for Darcy, Forchheimer, and trans-Forchheimer flow in porous media. In *SPE Annual Technical Conference and Exhibition, 26-29 September 2004, Houston, Texas*, SPE 89325.
- Batzle, M. L. and Wang, Z. (1992). Seismic properties of pore fluids. *Geophysics*, 57(11):1396–1408.
- Bear, J. (1979). *Hydraulics of groundwater*. McGraw-Hill, New York, USA.
- Bedrikovetsky, P. (1993). *Mathematical theory of oil and gas recovery: with applications to ex-USSR oil and gas fields*. Springer Publishing, New York, USA.
- Belhaj, H. A., Agha, K. R., Nouri, A. M., Butt, S. D., Vaziri, H. H., and Islam, M. R. (2003). Numerical modeling of Forchheimer’s equation to describe Darcy and non-Darcy flow in porous media. In *SPE Asia Pacific Oil and Gas Conference and Exhibition, 9-11 September 2003, Jakarta, Indonesia*, SPE 80440.

- Bennion, B. and Bachu, S. (2005). Relative permeability characteristics for supercritical CO₂ displacing water in a variety of potential sequestration zones. In *SPE Annual Technical Conference and Exhibition, 9-12 October 2005, Dallas, Texas*, SPE 95547.
- Birkholzer, J. T., Zhou, Q., and Tsang, C. F. (2009). Large-scale impact of CO₂ storage in deep saline aquifers: A sensitivity study on pressure response in stratified systems. *International Journal of Greenhouse Gas Control*, 3(2):181–194.
- Bolton, E. W., Lasaga, A. C., and Rye, D. M. (1999). Long-term flow/chemistry feedback in a porous medium with heterogenous permeability: kinetic control of dissolution and precipitation. *American Journal of Science*, 299(1):1–68.
- Buckley, S. E. and Leverett, M. C. (1942). Mechanism of fluid displacement in sands. *Petroleum Technology*, 146(1337):107–116.
- Burton, M. M., Kumar, N., and Bryant, S. (2008). Time-dependent injectivity during CO₂ storage in aquifers. In *SPE/DOE Symposium on Improved Oil Recovery, 20-23 April 2008, Tulsa, Oklahoma*, SPE 113937.
- Cavanagh, A. and Wildgust, N. (2011). Pressurization and brine displacement issues for deep saline formation CO₂ storage. *Energy Procedia*, 4:4814–4821.
- Cavanagh, A. J., Haszeldine, R. S., and Blunt, M. J. (2010). Open or closed? A discussion of the mistaken assumptions in the Economides pressure analysis of carbon sequestration. *Journal of Petroleum Science and Engineering*, 74(1-2):107–110.
- Chadwick, A., Smith, D., Hodrien, C., Hovorka, S., Mackay, E., Mathias, S., Lovell, B., Kalaydjian, F., Sweeney, G., Benson, S., Dooley, J., and Davidson, C. (2010). The realities of storing carbon dioxide – A response to CO₂ storage capacity issues raised by Ehlig-Economides & Economides. *Available from Nature Precedings*, <http://dx.doi.org/10.1038/npre.2010.4500.1>.
- Chandra, V. S., Hamdi, H., Corbett, P., and Geiger, S. (2011). Improving reservoir characterisation and simulation with near wellbore modeling. In *SPE Reservoir Characterisation and Simulation Conference and Exhibition*, SPE 148104.
- Chen, C., Wan, J., and Zhan, H. (2003). Theoretical and experimental studies of coupled seepage-pipe flow to a horizontal well. *Journal of Hydrology*, 281(1):159–171.

- Chen, C. S. and Chang, C. C. (2003). Well hydraulics theory and data analysis of the constant head test in an unconfined aquifer with the skin effect. *Water Resources Research*, 39(5):1121–1136.
- Chen, Z., Lyons, S., and Qin, G. (2001). Derivation of the Forchheimer law via homogenization. *Transport in Porous Media*, 44(2):325–335.
- Choi, E. S., Cheema, T., and Islam, M. R. (1997). A new dual-porosity/dual-permeability model with non-Darcian flow through fractures. *Journal of Petroleum Science and Engineering*, 17(3):331–344.
- Chukwudozie, C. P., Tyagi, M., Sears, S. O., and White, C. D. (2012). Prediction of non-Darcy coefficients for inertial flows through the Castlegate sandstone using image-based modeling. *Transport in Porous Media*, 95:563–580.
- Corey, A. T. (1954). The interrelation between gas and oil relative permeabilities. *Producers Monthly*, 19(1):38–41.
- Dake, L. P. (1983). *Fundamentals of reservoir engineering*. Elsevier Science, Amsterdam, Netherlands.
- Darcy, H. (1856). Les Fontaines publiques de la ville de Dijon. Technical report, Dalmont, Paris.
- Dentz, M. and Tartakovsky, D. M. (2009). Abrupt-interface solution for carbon dioxide injection into porous media. *Transport in Porous Media*, 79(1):15–27.
- Dietz, D. N. (1953). A theoretical approach to the problem of encroaching and bypassing edge water. *Proceedings of the Koninklijke Nederlandse Akademie van Wetenschappen*, 56:1–83.
- Dietz, D. N. (1965). Determination of average reservoir pressure from build-up surveys. *Journal of Petroleum Technology*, 17(8):955–959.
- Dong, H. (2007). *Micro-CT imaging and pore network extraction*. PhD thesis, Imperial College London.
- Eck, B. J., Barrett, M. E., and Charbeneau, R. J. (2012). Forchheimer flow in gently sloping layers: Application to drainage of porous asphalt. *Water Resources Research*, 48(1):W01530.

- Ehlig-Economides, C. and Economides, M. J. (2010). Sequestering carbon dioxide in a closed underground volume. *Journal of Petroleum Science and Engineering*, 70(1-2):123–130.
- Eiken, O., Ringrose, P., Hermanrud, C., Nazarian, B., Torp, T. A., and Høier, L. (2011). Lessons learned from 14 years of CCS operations: Sleipner, In Salah and Snøhvit. *Energy Procedia*, 4:5541–5548.
- Evans, E. V. and Evans, R. D. (1988). The influence of an immobile or mobile saturation upon non-Darcy compressible flow of real gases in propped fractures. *Journal of Petroleum Technology*, 40(10):1343–1351.
- Ewing, R. E., Lazarov, R. D., Lyons, S. L., Papavassiliou, D. V., Pasciak, J., and Qin, G. (1999). Numerical well model for non-Darcy flow through isotropic porous media. *Computational Geosciences*, 3(3):185–204.
- Fenghour, A., Wakeham, W. A., and Vesovic, V. (1998). The viscosity of carbon dioxide. *Journal of Physical and Chemical Reference Data*, 27(1):31–44.
- Forchheimer, P. (1901). Wasserbewegung durch boden. *Z. Ver. Deutsch. Ing*, 45(1):1782–1788.
- Frederick, D. C. and Graves, R. M. (1994). New correlations to predict non-Darcy flow coefficients at immobile and mobile water saturation. In *SPE Annual Technical Conference and Exhibition, 25-28 September 1994, New Orleans, Louisiana*, SPE 28451.
- Fuller, R. C., Prevost, J. H., and Piri, M. (2006). Three-phase equilibrium and partitioning calculations for CO₂ sequestration in saline aquifers. *Journal of Geophysical Research*, 111:B06207.
- Gasda, S. E., Nordbotten, J. M., and Celia, M. A. (2009). Vertical equilibrium with subscale analytical methods for geological CO₂ sequestration. *Computational Geosciences*, 13(4):469–481.
- Geertsma, J. (1974). Estimating the coefficient of inertial resistance in fluid flow through porous media. *Old SPE Journal*, 14(5):445–450.
- Gewers, C. and Nichol, L. (1969). Gas turbulence factor in a microvugular carbonate. *Journal of Canadian Petroleum Technology*, 8(2):51–56.

- Giorgi, T. (1997). Derivation of the Forchheimer law via matched asymptotic expansions. *Transport in Porous Media*, 29(2):191–206.
- Giorgis, T., Carpita, M., and Battistelli, A. (2007). 2D modeling of salt precipitation during the injection of dry CO₂ in a depleted gas reservoir. *Energy Conversion and Management*, 48(6):1816–1826.
- Gray, W. G., Herrera, P., Gasda, S. E., and Dahle, H. K. (2011). Derivation of vertical equilibrium models for CO₂ migration from pore scale equations. *International Journal of Numerical Analysis and Modeling*, 9(3):745–776.
- Greenberg, M. D. (1978). *Foundations of applied mathematics*. Prentice-Hall, New Jersey, USA.
- Hassanizadeh, S. M. and Gray, W. G. (1987). High velocity flow in porous media. *Transport in Porous Media*, 2(6):521–531.
- Heinemann, N., Wilkinson, M., Pickup, G. E., Haszeldine, R. S., and Cutler, N. A. (2012). CO₂ storage in the offshore UK Bunter sandstone formation. *International Journal of Greenhouse Gas Control*, 6:210–219.
- Holditch, S. A. and Morse, R. A. (1976). The effects of non-Darcy flow on the behavior of hydraulically fractured gas wells. *Journal of Petroleum Technology*, 28(10):1169–1179.
- Hurter, S., Labregere, D., and Berge, J. (2007). Simulations for CO₂ injection projects with compositional simulator. In *Geophysical Research Abstracts*, volume 9, page 11055, SPE 108540.
- Irmay, S. (1958). On the theoretical derivation of Darcy and Forchheimer formulas. *Transaction American Geophysical Union*, 39(4):702–707.
- Janicek, J. D. and Katz, D. L. V. (1955). Applications of unsteady state gas flow calculations. In *University of Michigan Research Conference, 20 June 1955*.
- Juanes, R. and Lie, K. A. (2007). Numerical modeling of multiphase first-contact miscible flows. Part 1. Analytical Riemann solver. *Transport in porous media*, 67(3):375–393.
- Kelkar, M. (2000). Estimation of turbulence coefficient based on field observations. *SPE Reservoir Evaluation & Engineering*, 3(2):160–164.

- Kestin, J., Khalifa, H. E., and Correia, R. J. (1981). *Tables of the dynamic and kinematic viscosity of aqueous NaCl solutions in the temperature range 20-150 C and the pressure range 0.1-35 MPa*. American Chemical Society and the American Institute of Physics for the National Bureau of Standards, Washington, USA.
- Kohl, T., Evans, K. F., Hopkirk, J., Jung, R., and Rybach, L. (1997). Observation and simulation of non-Darcian flow transients in fractured rock. *Water Resources Research*, 33(3):407–418.
- Kolditz, O. (2001). Non-linear flow in fractured rock. *International Journal of Numerical Methods for Heat & Fluid Flow*, 11(6):547–575.
- Krevor, S. C. M., Pini, R., Zuo, L., and Benson, S. M. (2012). Relative permeability and trapping of CO₂ and water in sandstone rocks at reservoir conditions. *Water Resources Research*, 48(2):W02532.
- Kutasov, I. M. (1993). Equation predicts non-Darcy flow coefficient. *Oil and Gas Journal*, 91(11):66–67.
- Lee, J. Y. and Lee, K. K. (1999). Analysis of the quality of parameter estimates from repeated pumping and slug tests in a fractured porous aquifer system in Wonju, Korea. *Ground Water*, 37(5):692–700.
- LeFloch, P. G. (2002). *Hyperbolic systems of conservation laws: The theory of classical and nonclassical shock waves*. Birkhäuser, Basel, Switzerland.
- Legrand, J. (2002). Revisited analysis of pressure drop in flow through crushed rocks. *Journal of Hydraulic Engineering*, 128(11):1027–1031.
- LeVeque, R. J. (1992). *Numerical methods for conservation laws*. Birkhäuser, Basel, Switzerland.
- Li, D. and Engler, T. (2001). Literature review on correlations of the non-Darcy coefficient. In *SPE Permian Basin Oil and Gas Recovery Conference, 15-17 May 2001, Midland, Texas*, SPE 70015.
- Lighthill, M. J. and Whitham, G. B. (1955). On kinematic waves. I. Flood movement in long rivers. *Proceedings of the Royal Society of London. Series A. Mathematical and Physical Sciences*, 229(1178):281–316.

- Liu, X., Civan, F., and Evans, R. (1995). Correlation of the non-Darcy flow coefficient. *Journal of Canadian Petroleum Technology*, 34(10):50–54.
- Lu, C., Lee, S. Y., Han, W. S., McPherson, B. J., and Lichtner, P. C. (2009). Comments on "Abrupt-interface solution for carbon dioxide injection into porous media" by M. Dentz and D. Tartakovsky. *Transport in Porous Media*, 79(1):29–37.
- Luckner, L., Van Genuchten, M. T., and Nielsen, D. R. (1989). A consistent set of parametric models for the two-phase flow of immiscible fluids in the subsurface. *Water Resources Research*, 25(10):2187–2193.
- Martin, R. and Dillion, P. (2002). Aquifer storage and recovery. Technical report, Department of Water, Land and Biodiversity Conservation.
- Mathias, S. A. and Butler, A. P. (2006). Linearized Richards' equation approach to pumping test analysis in compressible aquifers. *Water Resources Research*, 42(6):W06408.
- Mathias, S. A., Butler, A. P., and Zhan, H. (2008). Approximate solutions for Forchheimer flow to a well. *Journal of Hydraulic Engineering*, 134(9):1318–1325.
- Mathias, S. A., Gluyas, J. G., de Miguel, G. J. G. M., and Hosseini, S. A. (2011a). Role of partial miscibility on pressure buildup due to constant rate injection of CO₂ into closed and open brine aquifers. *Water Resources Research*, 47(12):W12525.
- Mathias, S. A., Gluyas, J. G., Oldenburg, C. M., and Tsang, C. F. (2010). Analytical solution for Joule–Thomson cooling during CO₂ geo-sequestration in depleted oil and gas reservoirs. *International Journal of Greenhouse Gas Control*, 4(5):806–810.
- Mathias, S. A., Gonzalez Martinez de Miguel, G. J., Thatcher, K. E., and Zimmerman, R. W. (2011b). Pressure buildup during CO₂ injection into a closed brine aquifer. *Transport in Porous Media*, 89(3):383–397.
- Mathias, S. A., Hardisty, P. E., Trudell, M. R., and Zimmerman, R. W. (2009a). Approximate solutions for pressure buildup during CO₂ injection in brine aquifers. *Transport in Porous Media*, 79(2):265–284.
- Mathias, S. A., Hardisty, P. E., Trudell, M. R., and Zimmerman, R. W. (2009b). Screening and selection of sites for CO₂ sequestration based on pressure buildup. *International Journal of Greenhouse Gas Control*, 3(5):577–585.

- Mathias, S. A. and Todman, L. C. (2010). Step-drawdown tests and the Forchheimer equation. *Water Resources Research*, 46(7):W07514.
- Metz, B. (2005). *IPCC special report on carbon dioxide capture and storage*. Cambridge University Press, Cambridge, UK.
- Mijic, A. (2009). Forchheimer flow in multiple well systems. Master’s thesis, Imperial College London.
- Moutsopoulos, K. N. (2007). One-dimensional unsteady inertial flow in phreatic aquifers induced by a sudden change of the boundary head. *Transport in Porous Media*, 70(1):97–125.
- Nickalls, R. W. D. (1993). A new approach to solving the cubic: Cardan’s solution revealed. *The Mathematical Gazette*, 77(480):354–359.
- Noh, M., Lake, L., Bryant, S., and Araque-Martinez, A. (2007). Implications of coupling fractional flow and geochemistry for CO₂ injection in aquifers. *SPE Reservoir Evaluation & Engineering*, 10(4):406–414.
- Nordbotten, J. M. and Celia, M. A. (2006). Similarity solutions for fluid injection into confined aquifers. *Journal of Fluid Mechanics*, 561:307–327.
- Nordbotten, J. M., Celia, M. A., and Bachu, S. (2004). Analytical solutions for leakage rates through abandoned wells. *Water Resources Research*, 40(4):W04204.
- Nordbotten, J. M., Celia, M. A., and Bachu, S. (2005). Injection and storage of CO₂ in deep saline aquifers: A analytical solution for CO₂ plume evolution during injection. *Transport in Porous media*, 58(3):339–360.
- Novotny, R. and Pech, P. (2005). Analytical solutions for well drawdown with well losses: 2. Real well near boundary - solution by image well. *Journal of Environmental Hydrology*, 13(28):1–7.
- Oldenburg, C. M. (2007). Joule-Thomson cooling due to CO₂ injection into natural gas reservoirs. *Energy Conversion and Management*, 48(6):1808–1815.
- Oldenburg, C. M., Stevens, S. H., and Benson, S. M. (2004). Economic feasibility of carbon sequestration with enhanced gas recovery (CSEGR). *Energy*, 29(9):1413–1422.

- Orr, F. M. (2007). *Theory of gas injection processes*. Tie-Line Publications, Holte, Denmark.
- Pan, C., Hilpert, M., and Miller, C. T. (2004). Lattice-Boltzmann simulation of two-phase flow in porous media. *Water Resources Research*, 40(1):W01501.
- Pech, P. and Novotny, R. (2005). Analytical solutions for well drawdown with well losses: 1. Multiple well system near a boundary. *Journal of Environmental Hydrology*, 13(27):1–10.
- Pope, G. (1980). The application of fractional flow theory to enhanced oil recovery. *Old SPE Journal*, 20(3):191–205.
- Prévost, J. H., Fuller, R. C., Altevogt, A. S., Bruant, R., and Scherer, G. W. (2004). Numerical modeling of carbon dioxide injection and transport in deep saline aquifers. In *Proceedings, 7th International Conference on Greenhouse Gas Control Technologies, Vancouver, BC*.
- Pruess, K. (1987). TOUGH user’s guide. Technical report, Lawrence Berkeley Lab., CA (USA); Nuclear Regulatory Commission, Washington, DC (USA). Division of Waste Management.
- Pruess, K. (2005). *ECO2N: A TOUGH2 fluid property module for mixtures of water, NaCl, and CO₂*. Lawrence Berkeley National Laboratory, Berkeley, USA.
- Pruess, K. (2009). Formation dry-out from CO₂ injection into saline aquifers: 2. Analytical model for salt precipitation. *Water Resources Research*, 45(3):W03403.
- Pruess, K. and Müller, N. (2009). Formation dry-out from CO₂ injection into saline aquifers: 1. Effects of solids precipitation and their mitigation. *Water Resources Research*, 45(3):W03402.
- Pruess, K. and Spycher, N. (2007). ECO2N – A fluid property module for the TOUGH2 code for studies of CO₂ storage in saline aquifers. *Energy Conversion and Management*, 48(6):1761–1767.
- Qian, J., Zhan, H., Luo, S., and Zhao, W. (2007). Experimental evidence of scale-dependent hydraulic conductivity for fully developed turbulent flow in a single fracture. *Journal of Hydrology*, 339(3-4):206–215.
- Qian, J., Zhan, H., Zhao, W., and Sun, F. (2005). Experimental study of turbulent unconfined groundwater flow in a single fracture. *Journal of Hydrology*, 311(1):134–142.

- Reddy, N. B. P. and Rao, P. R. M. (2006). Effect of convergence on nonlinear flow in porous media. *Journal of Hydraulic Engineering*, 132(4):420–427.
- Redlich, O. and Kwong, J. N. S. (1949). On the thermodynamics of solutions. V. An equation of state. Fugacities of gaseous solutions. *Chemical Reviews*, 44(1):233–244.
- Reilly, T., Franke, O. L., and Bennet, G. D. (1984). *The principle of superposition and its application in ground-water hydraulics*. U.S. Geological Survey, Reston, USA.
- Rossen, W. R., Venkatraman, A., Johns, R. T., Kibodeaux, K. R., Lai, H., and Tehrani, N. M. (2011). Fractional flow theory applicable to non-Newtonian behaviour in EOR processes. *Transport in Porous Media*, 89(2):213–236.
- Rumpf, B., Nicolaisen, H., Öcal, C., and Maurer, G. (1994). Solubility of carbon dioxide in aqueous solutions of sodium chloride: Experimental results and correlation. *Journal of Solution Chemistry*, 23(3):431–448.
- Ruth, D. and Ma, H. (1992). On the derivation of the Forchheimer equation by means of the averaging theorem. *Transport in Porous Media*, 7(3):255–264.
- Rutqvist, J., Birkholzer, J., Cappa, F., and Tsang, C. F. (2007). Estimating maximum sustainable injection pressure during geological sequestration of CO₂ using coupled fluid flow and geomechanical fault-slip analysis. *Energy Conversion and Management*, 48(6):1798–1807.
- Rutqvist, J., Birkholzer, J. T., and Tsang, C. F. (2008). Coupled reservoir–geomechanical analysis of the potential for tensile and shear failure associated with CO₂ injection in multilayered reservoir–caprock systems. *International Journal of Rock Mechanics and Mining Sciences*, 45(2):132–143.
- Saripalli, P. and McGrail, P. (2002). Semi-analytical approaches to modeling deep well injection of CO₂ for geological sequestration. *Energy Conversion and Management*, 43(2):185–198.
- Schlumberger (2002). ECLIPSE 300 Technical Description 2002A. Technical report, Schlumberger Information Solutions.
- Schwartz, F. W. and Zhang, H. (2002). *Fundamentals of ground water*. John Wiley & Sons, New York, USA.

- Şen, Z. (1988). Analytical solution incorporating nonlinear radial flow in confined aquifers. *Water Resources Research*, 24(4):601–606.
- Sidiropoulou, M. G., Moutsopoulos, K. N., and Tsihrintzis, V. A. (2007). Determination of Forchheimer equation coefficients a and b . *Hydrological Processes*, 21(4):534–554.
- Singurindy, O. and Berkowitz, B. (2005). The role of fractures on coupled dissolution and precipitation patterns in carbonate rocks. *Advances in water resources*, 28(5):507–521.
- Spycher, N. and Pruess, K. (2005). CO₂-H₂O mixtures in the geological sequestration of CO₂. II. Partitioning in chloride brines at 12–100 C and up to 600 bar. *Geochimica et Cosmochimica Acta*, 69(13):3309–3320.
- Spycher, N., Pruess, K., and Ennis-King, J. (2003). CO₂-H₂O mixtures in the geological sequestration of CO₂. I. Assessment and calculation of mutual solubilities from 12 to 100 C and up to 600 bar. *Geochimica et Cosmochimica Acta*, 67(16):3015–3031.
- Stephenson, G. and Radmore, P. M. (1990). *Advanced mathematical methods for engineers and science students*. Cambridge University Press, Cambridge, UK.
- Theis, C. V. (1935). The relation between the lowering of the piezometric surface and the rate and duration of discharge of a well using ground water storage. *Transaction American Geophysical Union*, 16(1):519–524.
- Thiem, G. (1906). *Hydrologische methode*. PhD thesis, Gebhardt, Leipzig.
- Thiruvengadam, M. and Kumar, G. N. (1997). Validity of Forchheimer equation in radial flow through coarse granular media. *Journal of Engineering Mechanics*, 123(7):696–705.
- van Genuchten, M. T. (1980). A closed-form equation for predicting the hydraulic conductivity of unsaturated soils. *Soil Science Society of America Journal*, 44(5):892–898.
- Vargaftik, N. B. (1975). *Tables on the thermophysical properties of liquids and gases: in normal and dissociated states*. Wiley, New York.
- Venkataraman, P. and Rama Mohan Rao, P. (1998). Darcian, transitional, and turbulent flow through porous media. *Journal of Hydraulic Engineering*, 124(8):840–846.
- Venkataraman, P. and Rama Mohan Rao, P. (2000). Validation of Forchheimer’s law for flow through porous media with converging boundaries. *Journal of Hydraulic Engineering*, 126(1):63–71.

- Vilarrasa, V., Bolster, D., Dentz, M., Olivella, S., and Carrera, J. (2010). Effects of CO₂ compressibility on CO₂ storage in deep saline aquifers. *Transport in Porous Media*, 85(2):619–639.
- Wang, H. F. and Anderson, M. P. (1995). *Introduction to groundwater modeling: Finite difference and finite element methods*. W. H. Freeman and Company, San Francisco, USA.
- Welge, H. J. (1952). A simplified method for computing oil recovery by gas or water drive. *Petroleum Transactions AIME*, 195:91–98.
- Wheater, H. S., Mathias, S. A., and Li, X. (2010). *Groundwater Modelling in Arid and Semi-Arid Areas*. Cambridge University Press, Cambridge, UK.
- Whitaker, S. (1996). The Forchheimer equation: A theoretical development. *Transport in Porous Media*, 25(1):27–61.
- Whitham, G. B. (2011). *Linear and nonlinear waves*, volume 42. Wiley-Interscience, New York, USA.
- Wong, S. (1970). Effect of liquid saturation on turbulence factors for gas-liquid systems. *Journal of Canadian Petroleum Technology*, 9(4):274–278.
- Wu, Y. S. (2001). Non-Darcy displacement of immiscible fluids in porous media. *Water Resources Research*, 37(12):2943–2950.
- Wu, Y. S. (2002a). An approximate analytical solution for non-Darcy flow toward a well in fractured media. *Water Resources Research*, 38(3):1–7.
- Wu, Y. S. (2002b). Numerical simulation of single-phase and multiphase non-Darcy flow in porous and fractured reservoirs. *Transport in Porous Media*, 49(2):209–240.
- Wu, Y. S., Lai, B., Miskimins, J. L., Fakcharoenphol, P., and Di, Y. (2011). Analysis of multiphase non-Darcy flow in porous media. *Transport in Porous Media*, 88(2):205–223.
- Wu, Y. S., Perapon Fakcharoenphol, P., and Zhang, R. (2010). Non-Darcy displacement in linear composite and radial flow porous media. In *SPE EUROPEC/EAGE Annual Conference and Exhibition, 14-17 June 2010, Barcelona, Spain*, SPE 130343.
- Yeh, H. D. and Chang, Y. C. (2012). Recent advances in modeling of well hydraulics. *Advances in Water Resources*, doi:10.1016/j.advwaters.2012.03.006.

- Yildiz, T. (2006). Assessment of total skin factor in perforated wells. *SPE Reservoir Evaluation & Engineering*, 9(1):61–76.
- Zakrisson, J., Edman, I., and Cinar, Y. (2008). Multiwell injectivity for CO₂ storage. In *SPE Asia Pacific Oil and Gas Conference and Exhibition, 20-22 October 2008, Perth, Australia*, SPE 116355.
- Zeidouni, M., Pooladi-Darvish, M., and Keith, D. (2009). Analytical solution to evaluate salt precipitation during CO₂ injection in saline aquifers. *International Journal of Greenhouse Gas Control*, 3(5):600–611.
- Zeng, Z. and Grigg, R. (2006). A criterion for non-Darcy flow in porous media. *Transport in Porous Media*, 63(1):57–69.
- Zhou, Q., Birkholzer, J. T., Tsang, C. F., and Rutqvist, J. (2008). A method for quick assessment of CO₂ storage capacity in closed and semi-closed saline formations. *International Journal of Greenhouse Gas Control*, 2(4):626–639.
- Zimmerman, R. W., Al-Yaarubi, A., Pain, C. C., and Grattoni, C. A. (2004). Non-linear regimes of fluid flow in rock fractures. *International Journal of Rock Mechanics and Mining Sciences*, 41(3):163–169.

Appendix A

Derivation of two-dimensional finite difference approximation for single-phase liquid non-Darcy flow

The continuity equation for two-dimensional (2D) flow can be written as:

$$\frac{\partial q_x}{\partial x} + \frac{\partial q_y}{\partial y} = \delta_{i,j} \frac{Q}{\Delta x \Delta y H} - D \frac{\partial P}{\partial t} \quad (\text{A.1})$$

where

$$q_x = -\frac{1}{\frac{\mu}{k} + \rho b |\vec{q}|} \frac{\partial P}{\partial x} \quad q_y = -\frac{1}{\frac{\mu}{k} + \rho b |\vec{q}|} \frac{\partial P}{\partial y} \quad (\text{A.2})$$

and

$$|\vec{q}| = \sqrt{q_x^2 + q_y^2} \quad (\text{A.3})$$

If the factor F is defined as:

$$F = \frac{\mu}{k} + \rho b |\vec{q}| \quad (\text{A.4})$$

then introducing equations (A.2) and (A.4) into equation (A.1) gives the second-order linear partial differential equation:

$$-\frac{1}{F_i} \frac{\partial^2 P}{\partial x^2} - \frac{1}{F_j} \frac{\partial^2 P}{\partial y^2} = \delta_{i,j} \frac{Q}{\Delta x \Delta y H} - D \frac{\partial P}{\partial t} \quad (\text{A.5})$$

Equation (A.5) can be written as a forward finite difference approximation, which gives:

$$a_{i,j}P_{i,j-1}^{n+1} + b_{i,j}P_{i-1,j}^{n+1} + c_{i,j}P_{i,j}^{n+1} + d_{i,j}P_{i+1,j}^{n+1} + e_{i,j}P_{i,j+1}^{n+1} = \delta_{i,j} \frac{Q}{4x_{i,B}y_{j,B}H} + D \frac{P_{i,j}^n}{t^{n+1} - t^n} \quad (\text{A.6})$$

where

$$a_{i,j} = -\frac{1}{F_{j-1}^n(y_j - y_{j-1})(y_{B,j+1} - y_{B,j})} \quad (\text{A.7})$$

$$b_{i,j} = -\frac{1}{F_{i-1}^n(x_i - x_{i-1})(x_{B,i+1} - x_{B,i})} \quad (\text{A.8})$$

$$d_{i,j} = -\frac{1}{F_{i+1}^n(x_{i+1} - x_i)(x_{B,i+1} - x_{B,i})} \quad (\text{A.9})$$

$$e_{i,j} = -\frac{1}{F_{j+1}^n(y_{j+1} - y_j)(y_{B,j+1} - y_{B,j})} \quad (\text{A.10})$$

$$c_{i,j} = -a_{i,j} - b_{i,j} - d_{i,j} - e_{i,j} + \rho c \frac{1}{t^{n+1} - t^n} \quad (\text{A.11})$$

Set of equations (A.6)-(A.11) can be written in a matrix form:

$$[M^n][P^{n+1}] = [f^n] \quad (\text{A.12})$$

where $[M^n]$ is a five-diagonal matrix of coefficients defined by equations (A.7)-(A.11) at the current time step, $[P^{n+1}]$ is the pressure vector in the next time step and $[f^n]$ is a sink term vector defined as:

$$f^n = \begin{cases} \delta_{i,j} \frac{Q}{4x_{i,B}y_{j,B}H} + D \frac{P_{i,j}^n}{t^{n+1} - t^n}, & i = j = 1 \\ D \frac{P_{i,j}^n}{t^{n+1} - t^n}, & i = 2 : N, j = 2 : N \end{cases} \quad (\text{A.13})$$

Appendix B

Derivation of the radial differential equation for single-phase flow

Under the assumptions of homogenous and isotropic formation, in which the injection well is completed across the entire saturated thickness, the application of the principle of mass conservation gives:

$$\underbrace{[(r + \Delta r)^2 - r^2] \pi H \Delta(\phi \rho)}_{\text{Change in storage}} = \underbrace{2r \pi H \Delta t \rho q}_{\text{Mass in}} - \underbrace{2(r + \Delta r) \pi H \Delta t [\rho q + \Delta(\rho q)]}_{\text{Mass out}} \quad (\text{B.1})$$

which, after rearranging and assuming infinitesimal Δr and Δt gives:

$$\frac{\partial(\phi \rho)}{\partial t} = -\frac{\rho q}{r} - \frac{\partial(\rho q)}{\partial r} \quad (\text{B.2})$$

Equation (B.2) can be further simplified by applying the product rule to the terms on the right-hand side:

$$\frac{\partial(\phi \rho)}{\partial t} + \frac{1}{r} \frac{\partial}{\partial r}(r \rho q) = 0 \quad (\text{B.3})$$

Compressibility of rock, c_r and fluid, c can be defined as (Wheater et al., 2010):

$$c_r = \frac{1}{\phi} \frac{d\phi}{dP} \quad (\text{B.4})$$

$$c = \frac{1}{\rho} \frac{d\rho}{dP} \quad (\text{B.5})$$

Above expressions can be extended in terms of a time derivative:

$$\frac{\partial \rho}{\partial t} = \phi c_r \frac{\partial P}{\partial t} \quad (\text{B.6})$$

$$\frac{\partial \phi}{\partial t} = \rho c \frac{\partial P}{\partial t} \quad (\text{B.7})$$

and substituted in equation (B.3) to obtain:

$$\rho \phi (c_r + c) \frac{\partial P}{\partial t} + \frac{1}{r} \frac{\partial}{\partial r} (r \rho q) = 0 \quad (\text{B.8})$$

If the fluid is assumed to be incompressible, that is $\rho = \text{const.}$, the governing equation for the radial single-phase flow in a porous medium reduces to:

$$\phi (c_r + c) \frac{\partial P}{\partial t} + \frac{1}{r} \frac{\partial}{\partial r} (r q) = 0 \quad (\text{B.9})$$

Appendix C

Equal area rule in radial non-Darcy displacement

The derivation of expressions for shock locations by implementing the equal area rule (EAR) is based upon the assumption that the integral of the discontinuous weak solution (i.e. composition profile) has to be the same as the area under the multivalued profile (LeVeque, 1992). The metrology is shown for the more complicated case, that is the miscible displacement. The expression for leading shock is then simplified to enable its application for immiscible flow analysis.

The composition profile along with the implementation of the equal area rule in miscible displacement problems is shown in Figure 5.3. The expression for the leading front location can be found by equating areas A_1 and A_2 (Figure C.1):

$$A_1 = r_{LD}C_{1h} - r_{bD}s_{1b} - \int_{C_{1c}}^{C_{1h}} r_D dC_1 \quad (C.1)$$

$$A_2 = \int_{C_{1h}}^{C_{1L}} r_D dC_1 - r_{LD}(C_{1L} - C_{1h}) \quad (C.2)$$

where

- s_{1b} is CO₂ concentration at $S_1 = 0$, where S_1 is gas saturation
- C_{1c} is CO₂ concentration at the critical gas saturation, S_{1c}
- C_{1h} is an intermediate CO₂ concentration used in the calculation of the EAR integral
- C_{1L} is CO₂ concentration at leading shock

- r_{LD} is the dimensionless radial extent of leading shock at time t
- r_{bD} is the dimensionless radial extent that brine would have reached at time t in a single-phase displacement

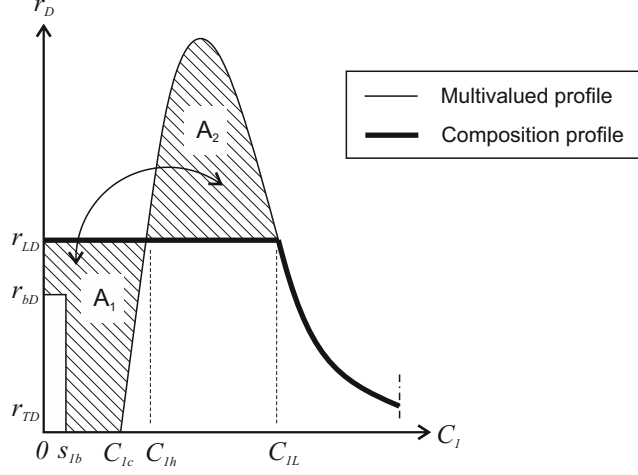


Figure C.1: Equal area rule for leading front calculation

Equating equations (C.1) and (C.2) gives:

$$\int_{C_{1c}}^{C_{1h}} r_D dC_1 + \int_{C_{1h}}^{C_{1L}} r_D dC_1 = r_{LD}(C_{1L} - C_{1h}) + r_{LD}C_{1h} - r_{bD}s_{1b} \quad (C.3)$$

which can be further rearranged to obtain the final expression for leading front position in miscible displacement:

$$r_{LD} = \frac{1}{C_{1L}} \left[r_{bD}s_{1b} + \int_{C_{1c}}^{C_{1L}} r_D dC_1 \right] \quad (C.4)$$

In case of the immiscible displacement, dependent variable is gas saturation, S_1 and the corresponding saturation profile is shown in Figure 4.3. If there is no interphase mass transfer, single-phase regions do not exist, which implies that $r_{bD} = 0$. The expression for r_{LD} in immiscible displacement therefore simplifies to:

$$r_{LD} = \frac{1}{S_{1L}} \int_{S_{1c}}^{S_{1L}} r_D dS_1 \quad (C.5)$$

The position of the trailing shock in miscible displacement can be found by equating

areas A_3 and A_4 (Figure C.2):

$$A_3 = r_{TD}(s_{1c} - C_{1T}) - \int_{C_{1T}}^{1-C_{2r}} r_D dC_1 \quad (C.6)$$

$$A_4 = (r_{cD} - r_{TD})(1 - s_{1c}) \quad (C.7)$$

where

- s_{1c} is CO₂ concentration at $S_1 = 1$
- $1 - C_{2r}$ is CO₂ concentration at the residual brine saturation, $1 - S_{2r}$
- C_{1T} is CO₂ concentration at trailing shock
- r_{TD} is the dimensionless radial extent of trailing shock at time t
- r_{cD} is the dimensionless radial extent that gas would have reached at time t in a single-phase displacement

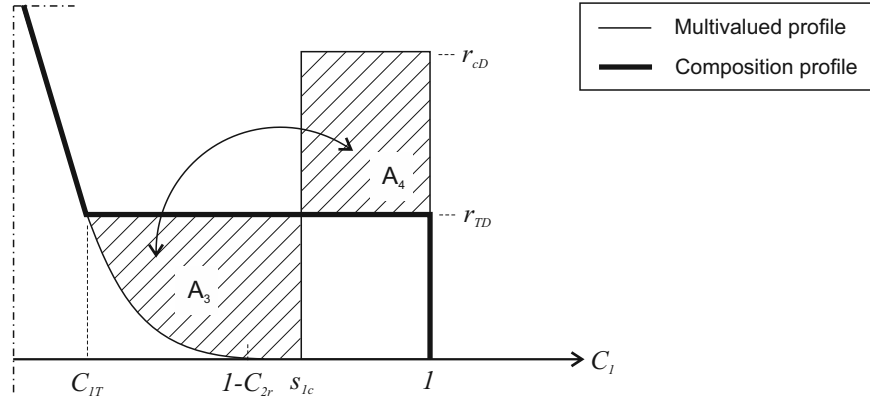


Figure C.2: Equal area rule for trailing front calculation

Equating equations (C.6) and (C.7) results in:

$$\int_{C_{1T}}^{1-C_{2r}} r_D dC_1 = r_{TD}(1 - C_{1T}) - r_{cD}(1 - s_{1c}) \quad (C.8)$$

Finally, the location of the trailing shock can be obtained from:

$$r_{TD} = \frac{1}{1 - C_{1T}} \left[r_{cD}(1 - s_{1c}) + \int_{C_{1T}}^{1-C_{2r}} r_D dC_1 \right] \quad (\text{C.9})$$

Note that equation (C.9) is valid for non-Darcy displacement, in which the gas wave velocity in a single-phase displacement varies with the distance from the well. In case of Darcy displacement, this velocity is constant and thus $r_{cD} = r_{bD}$.

Appendix D

Derivation of the radial differential equation for compressible two-phase displacement

Assuming the gas phase compressibility, the two-phase flow of an immiscible liquid and gas in a porous medium can be described by the system of mass conservation equations:

$$\frac{\partial(S_1\rho_1)}{\partial t} + \frac{1}{\phi} \left[\frac{\rho_1 q_1}{r} + \frac{\partial(\rho_1 q_1)}{\partial r} \right] = 0 \quad (\text{D.1})$$

$$\frac{\partial S_2}{\partial t} + \frac{1}{\phi} \left[\frac{q_2}{r} + \frac{\partial q_2}{\partial r} \right] = 0 \quad (\text{D.2})$$

If the total fluid flux is defined as a sum of phase velocities:

$$q = q_1 + q_2 \quad (\text{D.3})$$

and the concept of fractional flow is applied (Buckley and Leverett, 1942):

$$f_1 = 1 - f_2 = \frac{q_1}{q} \quad (\text{D.4})$$

the governing differential equations can be written as:

$$\frac{\partial(S_1\rho_1)}{\partial t} + \frac{1}{\phi} \left[\frac{\rho_1 f_1 q}{r} + \frac{\partial(\rho_1 f_1 q)}{\partial r} \right] = 0 \quad (\text{D.5})$$

$$\frac{\partial S_2}{\partial t} + \frac{1}{\phi} \left[\frac{(1-f_1)q}{r} + \frac{\partial(1-f_1)q}{\partial r} \right] = 0 \quad (\text{D.6})$$

The above system of partial differential equations admits the self-similar solution (Bedrikovetsky, 1993):

$$S_1 = 1 - S_2 = S_1(\xi) \quad (\text{D.7})$$

$$q = \frac{U(\xi)}{\sqrt{2t}} \quad (\text{D.8})$$

$$\xi = \frac{r}{\sqrt{2t}} \quad (\text{D.9})$$

The self similar function (D.9) can be differentiated with respect to space and time:

$$\frac{d\xi}{dr} = \frac{1}{\sqrt{2t}} \quad (\text{D.10})$$

$$\frac{d\xi}{dt} = -\frac{1}{2t} \frac{r}{\sqrt{2t}} = -\frac{\xi}{2t} \quad (\text{D.11})$$

Substitution of expressions (D.7)-(D.11) into equations (D.5) and (D.6) gives the system of ordinary differential equations:

$$-\xi \frac{d(S_1 \rho_1)}{d\xi} + \frac{1}{\phi} \left[\frac{\rho_1 f_1 U}{\xi} + \frac{d}{d\xi} (\rho_1 f_1 U) \right] = 0 \quad (\text{D.12})$$

$$\xi \frac{dS_1}{d\xi} + \frac{1}{\phi} \left[\frac{(1-f_1)U}{\xi} + \frac{d}{d\xi} [(1-f_1)U] \right] = 0 \quad (\text{D.13})$$

which can be further modified by applying the product rule and rearranged to obtain:

$$\frac{\rho_1 f_1}{\phi} \frac{dU}{d\xi} = \frac{d\rho_1}{d\xi} \left(\xi S_1 - \frac{f_1 U}{\phi} \right) - \frac{\rho_1 f_1 U}{\phi \xi} - \frac{\rho_1 U}{\phi} \frac{df_1}{d\xi} + \rho_1 \xi \frac{dS_1}{d\xi} \quad (\text{D.14})$$

$$\xi \frac{dS_1}{d\xi} = -\frac{(1-f_1)U}{\phi \xi} + \frac{U}{\phi} \frac{df_1}{d\xi} - \frac{(1-f_1)}{\phi} \frac{dU}{d\xi} \quad (\text{D.15})$$

After equation (D.15) has been substituted into (D.14), the solution gives the change of the fluid flux in a compressible displacement:

$$\frac{dU}{d\xi} = \frac{\phi}{\rho_1} \frac{d\rho_1}{d\xi} \left(\xi S_1 - \frac{f_1 U}{\phi} \right) - \frac{U}{\xi} \quad (\text{D.16})$$

Expressions (D.8)-(D.11) can again be used to revert equations (D.15) and (D.16) into the original notation. Finally, the system (D.5)-(D.6) can be written in the form:

$$\frac{\partial S_1}{\partial t} + \frac{q}{\phi} \frac{\partial f_1}{\partial r} - \frac{1}{\phi} \left[(1 - f_1) \frac{q}{r} + (1 - f_1) \frac{\partial q}{r} \right] = 0 \quad (\text{D.17})$$

$$\frac{dq}{dr} = \phi \frac{1}{\rho_1} \frac{d\rho_1}{dP} \frac{dP}{dr} \left(\frac{r S_1}{2t} - \frac{f_1 q}{\phi} \right) - \frac{q}{r} \quad (\text{D.18})$$

where $(d\rho_1/dP)/\rho_1$ defines the gas compressibility (Bear, 1979) and dP/dr is a pressure change under either Darcy or Forchheimer flow conditions.